

2

NAVAL POSTGRADUATE SCHOOL

Monterey, California

AD-A246 993




THESIS

A DIAGNOSTIC STUDY OF
RAPIDLY DEVELOPING CYCLONES USING
SURFACE-BASED Q VECTORS

by

David W. Titley

June, 1991

Thesis Advisor:

Wendell A. Nuss

Approved for public release; distribution is unlimited

92 3 03 200

92-05731



REPORT DOCUMENTATION PAGE				
1a. REPORT SECURITY CLASSIFICATION Unclassified		1b. RESTRICTIVE MARKINGS		
2a. SECURITY CLASSIFICATION AUTHORITY		3. DISTRIBUTION/AVAILABILITY OF REPORT Approved for public release; distribution is unlimited.		
2b. DECLASSIFICATION/DOWNGRADING SCHEDULE				
4. PERFORMING ORGANIZATION REPORT NUMBER(S)		5. MONITORING ORGANIZATION REPORT NUMBER(S)		
6a. NAME OF PERFORMING ORGANIZATION Naval Postgraduate School	6b. OFFICE SYMBOL (If applicable) 35	7a. NAME OF MONITORING ORGANIZATION Naval Postgraduate School		
6c. ADDRESS (City, State, and ZIP Code) Monterey, CA 93943-5000		7b. ADDRESS (City, State, and ZIP Code) Monterey, CA 93943-5000		
8a. NAME OF FUNDING/SPONSORING ORGANIZATION	8b. OFFICE SYMBOL (If applicable)	9. PROCUREMENT INSTRUMENT IDENTIFICATION NUMBER		
8c. ADDRESS (City, State, and ZIP Code)		10. SOURCE OF FUNDING NUMBERS		
		Program Element No.	Project No.	Task No.
				Work Unit Accession Number
11. TITLE (Include Security Classification) A DIAGNOSTIC STUDY OF RAPIDLY DEVELOPING CYCLONES USING SURFACE-BASED Q VECTORS				
12. PERSONAL AUTHOR(S) Titley, David W.				
13a. TYPE OF REPORT Master's Thesis	13b. TIME COVERED From To	14. DATE OF REPORT (year, month, day) 1991, June	15. PAGE COUNT 139	
16. SUPPLEMENTARY NOTATION The views expressed in this thesis are those of the author and do not reflect the official policy or position of the Department of Defense or the U.S. Government.				
17. COSATI CODES		18. SUBJECT TERMS (continue on reverse if necessary and identify by block number)		
FIELD	GROUP	SUBGROUP		
		ERICA, Q vectors, vertical motion, rapid cyclogenesis, marine cyclogenesis		
19. ABSTRACT (continue on reverse if necessary and identify by block number)				
<p>Accurate short-term (0-6 h) forecasts of rapid cyclogenesis are important to both civilian and military maritime interests. Because upper-air observations over the ocean are sparse, the relatively plentiful surface synoptic data must be used for diagnostic analysis. Surface pressure and temperature data for two Intensive Observation Periods (IOPs) that occurred during the Experiment on Rapidly Intensifying Cyclones over the Atlantic (ERICA) are objectively analyzed and Q vectors--a measure of the low-level ageostrophic flow required to restore geostrophic balance--are calculated. Areas of Q vector convergence, which imply upward vertical motion, were compared to satellite imagery and to the future 3-h and 6-h pressure tendencies. When the storms were intensifying most rapidly, satellite imagery showed cold-topped stratiform clouds over areas of Q vector convergence. Areas of strong Q vector convergence (divergence) showed significant (95% confidence level) pressure falls (rises) 3 h and 6 h in the future. Surface Q vectors are shown to have qualitative value in short-range forecasts of the location of the storm, but do not forecast storm intensity. The surface Q vector interpretations are less useful near landmasses, as the surface temperature field becomes less representative of the mean tropospheric temperature.</p>				
20. DISTRIBUTION/AVAILABILITY OF ABSTRACT		21. ABSTRACT SECURITY CLASSIFICATION		
<input checked="" type="checkbox"/> UNCLASSIFIED/UNLIMITED <input type="checkbox"/> SAME AS REPORT <input type="checkbox"/> DTIC USERS		Unclassified		
22a. NAME OF RESPONSIBLE INDIVIDUAL Wendell A. Nuss		22b. TELEPHONE (Include Area code) (408) 646-2308	22c. OFFICE SYMBOL 63Nu	

Approved for public release; distribution is unlimited.

A Diagnostic Study of
Rapidly Developing Cyclones using
Surface-Based Q Vectors

by

David W. Titley
Lieutenant Commander, United States Navy
B.S., The Pennsylvania State University, 1980

Submitted in partial fulfillment
of the requirements for the degree of

MASTER OF SCIENCE IN METEOROLOGY AND PHYSICAL OCEANOGRAPHY

from the

NAVAL POSTGRADUATE SCHOOL
June 1991

Author:

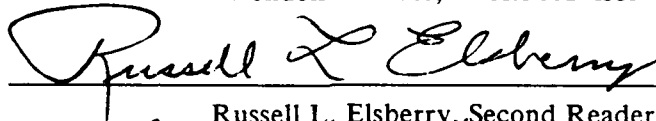


David W. Titley

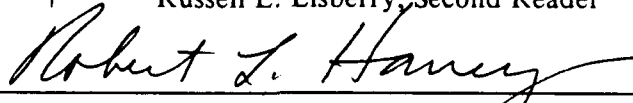
Approved by:



Wendell A. Nuss, Thesis Advisor



Russell L. Elsberry, Second Reader



Robert L. Haney, Chairman
Department of Meteorology

ABSTRACT

Accurate short-term (0-6 h) forecasts of rapid cyclogenesis are important to both civilian and military maritime interests. Because upper-air observations over the ocean are sparse, the relatively plentiful surface synoptic data must be used for diagnostic analysis. Surface pressure and temperature data for two Intensive Observation Periods (IOPs) that occurred during the Experiment on Rapidly Intensifying Cyclones over the Atlantic (ERICA) are objectively analyzed and Q vectors--a measure of the low-level ageostrophic flow required to restore geostrophic balance--are calculated. Areas of Q vector convergence, which imply upward vertical motion, were compared to satellite imagery and to the future 3-h and 6-h pressure tendencies. When the storms were intensifying most rapidly, satellite imagery showed cold-topped stratiform clouds over areas of Q vector convergence. Areas of strong Q vector convergence (divergence) showed significant (95% confidence level) pressure falls (rises) 3 h and 6 h in the future. Surface Q vectors are shown to have qualitative value in short-range forecasts of the location of the storm, but do not forecast storm intensity. The surface Q vector interpretations are less useful near landmasses, as the surface temperature field becomes less representative of the mean tropospheric temperature.



Accession For	
NTIS GRA&I	<input checked="" type="checkbox"/>
DTIC TAB	<input type="checkbox"/>
Unannounced	<input type="checkbox"/>
Justification	
By _____	
Distribution/ _____	
Availability Codes	
Dist	Avail and/or Special
A-1	

TABLE OF CONTENTS

I. INTRODUCTION	1
A. THE SIGNIFICANCE OF RAPID CYCLOGENESIS	1
B. OBJECTIVE	3
II. BACKGROUND	5
A. PREVIOUS RAPID CYCLOGENESIS STUDIES	5
B. CALCULATING VERTICAL MOTION	11
1. Quasi-Geostrophic Vertical Motion	11
a. Q Vectors	13
b. Limits to Quasi-Geostrophic Theory	15
c. Quasi-geostrophic Theory as Applied to Rapidly Developing Cyclones	18
d. Q Vectors Applied to Surface Data	19
2. Verifying Vertical Motion Calculations	19
C. EXPERIMENT ON RAPIDLY INTENSIFYING CYCLONES OVER THE ATLANTIC	20
III. DATA ANALYSIS	25
A. ANALYSIS METHOD	25
1. Comparison of Hand-drawn Surface Analyses	27

2. Obtaining the Gridded Fields	30
3. Calculating Q Vectors and the Associated Divergence Field	33
4. Evaluating the Q Vector Divergence Field	34
IV. CASE STUDIES	39
A. IOP 3	39
1. Synoptic Overview	39
2. Q Vectors and Satellite Imagery	50
3. Objective Verification of Q Vector Divergence	60
B. IOP 5	76
1. Synoptic Overview	76
2. Q Vectors and Satellite Imagery	87
3. Objective Verification of Q Vector Divergence	92
C. DISCUSSION	106
V. CONCLUSIONS AND RECOMMENDATIONS	113
A. CONCLUSIONS	113
B. RECOMMENDATIONS	114
LIST OF REFERENCES	116
INITIAL DISTRIBUTION LIST	121

LIST OF TABLES

Table 1. NUMBER OF DRIFTING BUOY OBSERVATIONS AND NUMBER OF TOTAL SURFACE MARINE OBSERVATIONS FOR THE IOP 3 CYCLONE.	27
Table 2. NUMBER OF DRIFTING BUOY OBSERVATIONS AND NUMBER OF TOTAL SURFACE MARINE OBSERVATIONS FOR THE IOP 5 CYCLONE.	28
Table 3. NUMBER OF BOGUS PRESSURE AND TEMPERATURE OBSERVATIONS INSERTED INTO THE IOP 3 ANALYSES.	32
Table 4. NUMBER OF BOGUS PRESSURE AND TEMPERATURE OBSERVATIONS INSERTED INTO THE IOP 5 ANALYSES.	33
Table 5. CORRELATION BETWEEN VERTICAL VELOCITY (w , cm s^{-1}) MEASURED BY AIRCRAFT AND $-2\mathbf{\nabla} \cdot \mathbf{Q}$ ($\text{m kg}^{-1} \text{s}^{-1}$) DURING IOP 3. . .	62
Table 6. CORRELATION COEFFICIENTS AND LINEAR REGRESSION EQUATIONS FOR THE IOP 3 CYCLONE.	69
Table 7. $-2\mathbf{\nabla} \cdot \mathbf{Q}$ VS. 3 H FUTURE PRESSURE TENDENCY FOR THE IOP 3 CYCLONE.	72
Table 8. $-2\mathbf{\nabla} \cdot \mathbf{Q}$ VS. 6 H FUTURE PRESSURE TENDENCY FOR THE IOP 3 CYCLONE.	73

Table 9. CORRELATION BETWEEN VERTICAL VELOCITY (w , cm s^{-1}) MEASURED BY AIRCRAFT AND $-2\nabla\cdot\mathbf{Q}$ ($\text{m kg}^{-1} \text{ s}^{-1}$) DURING IOP 5. . .	95
Table 10. CORRELATION COEFFICIENTS AND LINEAR REGRESSION EQUATIONS FOR THE IOP 5 CYCLONE.	101
Table 11. $-2\nabla\cdot\mathbf{Q}$ VS. 3 H FUTURE PRESSURE TENDENCY FOR THE IOP 5 CYCLONE.	104
Table 12. $-2\nabla\cdot\mathbf{Q}$ VS. 6 H FUTURE PRESSURE TENDENCY FOR THE IOP 5 CYCLONE.	105

LIST OF FIGURES

Fig. 1. Location (dots) of regularly reporting rawinsonde stations (Ohring 1990). .	3
Fig. 2. Isobars (solid, 4 mb intervals) and 1000-500 mb thickness (dashed, 60 dam intervals). Surface geostrophic wind in conventional notation, and Q vectors in bold arrows (Sanders and Hoskins 1990).	16
Fig. 3. Primary (dark stippling) and secondary (light stippling) areas where "ERICA-type" storms are most likely to occur (Hadlock <i>et al.</i> 1989).	22
Fig. 4. Location of deep-water moored buoys (squares), coastal moored buoys (circles) C-Man stations (triangles) and ERICA drifting buoys (numbers) as of 18 December 1988 (Hadlock <i>et al.</i> 1989).	23
Fig. 5. As in Fig. 4, except for 19 January 1989.	24
Fig. 6. Analyzed central pressure (mb) vs. time for IOP 3.	29
Fig. 7. Surface pressure (mb) and temperature (°C) analysis by Sanders (1989) for 0000 UTC 18 December 1988. Contour interval is 4 mb for pressure and 5°C for temperature.	34
Fig. 8. Surface pressure (mb) analysis by Titley for 0000 UTC 18 December 1988. Contour interval is 4 mb.	35
Fig. 9. Objective analysis of pressure (mb) and temperature (°C) for 0000 UTC 18 December 1988. Contour intervals as in Fig. 7. Bold lines indicate bounds of "cyclone domain".	36

Fig. 10. Tracks (solid) of IOP 3 storms as analyzed by Sanders (1989). Underlined number is pressure (mb). Time is (day/hour) UTC December 1988.	40
Fig. 11. 500 mb height (solid, contour interval 60 dam) and absolute vorticity (dashed, contour interval $3 \times 10^{-5} \text{ s}^{-1}$) analysis at 0000 UTC 17 December 1988.	41
Fig. 12. Surface pressure (solid, contour interval 4 mb) and temperature (dashed, contour interval 5°C) analysis at 1200 UTC 17 December 1988.	42
Fig. 13. Surface pressure (solid, contour interval 4 mb) and 1000-500 mb thickness (dashed, contour interval 60 dam) analysis at 1200 UTC 17 December 1988. "L" marks position of surface lows as shown in Fig. 12.	43
Fig. 14. 500 mb height and absolute vorticity analysis as in Fig. 11, except for 1200 UTC 17 December 1988.	44
Fig. 15. 300 mb isotach (solid, contour interval 10 m s^{-1}) and surface pressure (dashed, contour interval 4 mb) analysis at 1200 UTC 17 December 1988. . .	45
Fig. 16. Surface pressure and temperature analysis as in Fig. 7, except for 1800 UTC 17 December 1988.	46
Fig. 17. Sea-surface temperatures ($^{\circ}\text{C}$) during IOP 3 (Hadlock and Kreitzberg 1988).	47
Fig. 18. 300 mb isotach and surface pressure analysis as in Fig. 15, except for 0000 UTC 18 December 1988.	49
Fig. 19. Surface pressure and temperature analysis as in Fig. 7, except for 1200 UTC 18 December 1988.	50

Fig. 20. 500 mb height and absolute vorticity analysis as in Fig. 11, except for 1200 UTC 18 December 1988.	51
Fig. 21. $-2\nabla\cdot\mathbf{Q}$ (solid, contour interval $10\times 10^{-16} \text{ m kg}^{-1} \text{ s}^{-1}$), surface isobars (dashed, contour interval 4 mb) and \mathbf{Q} vectors (arrows) at 0600 UTC 17 December 1988.	52
Fig. 22. GOES IR imagery, and $-2\nabla\cdot\mathbf{Q}$ (contour interval $10\times 10^{-16} \text{ m kg}^{-1} \text{ s}^{-1}$, solid lines where $-2\nabla\cdot\mathbf{Q} > 0$) at 0601 UTC 17 December 1988.	53
Fig. 23. $-2\nabla\cdot\mathbf{Q}$, surface isobars and \mathbf{Q} vectors as in Fig. 21, except for 1200 UTC 17 December 1988.	55
Fig. 24. $-2\nabla\cdot\mathbf{Q}$, surface isobars and \mathbf{Q} vectors as in Fig. 21, except for 1800 UTC 17 December 1988.	56
Fig. 25. GOES Visible imagery and $-2\nabla\cdot\mathbf{Q}$ (contour interval $10\times 10^{-16} \text{ m kg}^{-1} \text{ s}^{-1}$, solid lines where $-2\nabla\cdot\mathbf{Q} > 0$) at 1901 UTC 17 December 1988.	57
Fig. 26. $-2\nabla\cdot\mathbf{Q}$, surface isobars and \mathbf{Q} vectors as in Fig. 21, except for 0300 UTC 18 December 1988.	58
Fig. 27. GOES IR imagery and $-2\nabla\cdot\mathbf{Q}$ as in Fig. 22, except for 0301 UTC 18 December 1988.	59
Fig. 28. GOES IR imagery and $-2\nabla\cdot\mathbf{Q}$ as in Fig. 22, except for 0601 UTC 18 December 1988.	60
Fig. 29. $-2\nabla\cdot\mathbf{Q}$, surface isobars and \mathbf{Q} vectors as in Fig. 21, except for 1800 UTC 18 December 1988.	61

Fig. 30. Vertical velocity (cm s^{-1} , 20 minute average), $-2\nabla\cdot\mathbf{Q}$ ($\times 10^{-16} \text{ m kg}^{-1} \text{ s}^{-1}$) and aircraft elevation (m) centered around 0900 UTC 18 December 1988.	63
Fig. 31. Vertical velocity, $-2\nabla\cdot\mathbf{Q}$ and aircraft elevation as in Fig. 30, but centered around 1200 UTC 18 December 1988.	64
Fig. 32. \mathbf{Q} vectors (arrows) at 1200 UTC 17 December 1988 and isallobars ($\text{mb}\cdot 10$ per 3 h, solid) for 1500-1200 UTC 17 December 1988.	65
Fig. 33. \mathbf{Q} vectors (arrows) at 1200 UTC 17 December and isallobars ($\text{mb}\cdot 10$ per 6 h, solid) for 1800-1200 UTC 17 December 1988.	66
Fig. 34. \mathbf{Q} vectors (arrows) at 0000 UTC 18 December 1988 and isallobars ($\text{mb}\cdot 10$ per 3 h, solid) for 0300-0000 UTC 18 December 1988.	67
Fig. 35. \mathbf{Q} vectors (arrows) at 0000 UTC 18 December 1988 and isallobars ($\text{mb}\cdot 10$ per 6 h, solid) for 0600-0000 UTC 18 December 1988.	68
Fig. 36. Scatter plot of $-2\nabla\cdot\mathbf{Q}$ ($\times 10^{-16} \text{ m kg}^{-1} \text{ s}^{-1}$) vs. the future 3 h pressure tendency ($\text{mb}\cdot 10$), linear regression line (dashed) and 95% confidence interval (dotted) for IOP 3.	70
Fig. 37. Scatter plot of $-2\nabla\cdot\mathbf{Q}$ ($\times 10^{-16} \text{ m kg}^{-1} \text{ s}^{-1}$) vs. the future 6 h pressure tendency ($\text{mb}\cdot 10$), linear regression line (dashed) and 95% confidence interval (dotted) for IOP 3.	71
Fig. 38. Mean 3 h pressure tendency for significant (see text) $ -2\nabla\cdot\mathbf{Q} $ (solid and dotted lines), 95% confidence intervals (hatched) and analyzed central pressure of the IOP 3 storm (dash-dot).	74
Fig. 39. As in Fig. 38, except for 6 h pressure tendency.	75

Fig. 40. Analyzed central pressure (mb) vs. time for IOP 5.	77
Fig. 41. Storm track as in Fig. 10, except for IOP 5 storm. Time is UTC, January 1989.	78
Fig. 42. Surface pressure and temperature analysis as in Fig. 7, except for 0000 UTC 19 January 1989.	79
Fig. 43. 500 mb height and absolute vorticity analysis as in Fig. 11, except for 0000 UTC 19 January 1989.	80
Fig. 44. Surface pressure and temperature analysis as in Fig. 7, except for 1200 UTC 19 January 1989.	81
Fig. 45. Sea-surface temperatures as in Fig. 17, except for 18-20 January 1989. . .	82
Fig. 46. 300 mb isotach and surface pressure analysis as in Fig. 15, except for 1200 UTC 19 January 1989.	83
Fig. 47. 500 mb height and absolute vorticity analysis as in Fig. 11, except for 1200 UTC 19 January 1989.	84
Fig. 48. Surface pressure and temperature analysis as in Fig. 7, except for 0000 UTC 20 January 1989.	85
Fig. 49. 500 mb height and absolute vorticity analysis as in Fig. 11, except for 0000 UTC 20 January 1989.	86
Fig. 50. 300 mb isotach and surface pressure analysis as in Fig. 15, except for 0000 UTC 20 January 1989.	87
Fig. 51. $-2\nabla \cdot \mathbf{Q}$, surface isobars and \mathbf{Q} vectors as in Fig. 21, except for 0000 UTC 19 January 1989.	88

Fig. 52. GOES IR imagery and $-2\nabla\cdot\mathbf{Q}$ as in Fig. 22, except for 0001 UTC 19 January 1989.	89
Fig. 53. $-2\nabla\cdot\mathbf{Q}$, surface isobars and \mathbf{Q} vectors as in Fig. 21, except for 0300 UTC 19 January 1989.	90
Fig. 54. GOES IR imagery and $-2\nabla\cdot\mathbf{Q}$ as in Fig. 22, except for 0601 UTC 19 January 1989.	91
Fig. 55. $-2\nabla\cdot\mathbf{Q}$, surface isobars and \mathbf{Q} vectors as in Fig. 21, except for 1200 UTC 19 January 1989.	92
Fig. 56. GOES IR imagery and $-2\nabla\cdot\mathbf{Q}$ as in Fig. 22, except for 1201 UTC 19 January 1989.	93
Fig. 57. $-2\nabla\cdot\mathbf{Q}$, surface isobars and \mathbf{Q} vectors as in Fig. 21, except for 0000 UTC 20 January 1989.	94
Fig. 58. Vertical velocity, $-2\nabla\cdot\mathbf{Q}$ and aircraft elevation as in Fig. 30 centered 90 minutes either side of 0600 UTC 20 January 1989.	96
Fig. 59. \mathbf{Q} vectors (arrows) at 0000 UTC 20 January 1989 and isallobars (mb*10 per 3 h, solid) for 0300-0000 UTC 20 January 1989.	97
Fig. 60. \mathbf{Q} vectors (arrows) at 0000 UTC 20 January 1989 and isallobars (mb*10 per 6 h, solid) for 0600-0000 UTC 20 January 1989.	98
Fig. 61. Scatter plot of $-2\nabla\cdot\mathbf{Q}$ ($\times 10^{-16}$ m kg ⁻¹ s ⁻¹) vs. the future 3 h pressure tendency (mb*10), with linear regression line (dashed) and 95% confidence interval (dotted) for IOP 5.	99

Fig. 62. Scatter plot of $-2\nabla\cdot\mathbf{Q}$ ($\times 10^{-16}$ m kg ⁻¹ s ⁻¹) vs. the future 6 h pressure tendency (mb*10), with linear regression line (dashed) and 95% confidence interval (dotted) for IOP 5.	100
Fig. 63. Mean 3 h pressure tendency for significant (see text) $ -2\nabla\cdot\mathbf{Q} $ (solid and dotted lines), 95% confidence intervals (hatched) and analyzed central pressure of the IOP 5 storm (dash-dot).	102
Fig. 64. As in Fig. 63, except for 6 h pressure tendency.	103
Fig. 65 Quasi-geostrophic vertical motion (ω , mb s ⁻¹) at 700 mb, based upon a full-physics model run of Kuo <i>et al.</i> (1991, Fig. 15 b).	109
Fig. 66. Quasi-geostrophic vertical motion (ω , mb s ⁻¹) at 700 mb calculated for an adiabatic experiment (Kuo <i>et al.</i> 1991, Fig. 15 a).	109
Fig. 67. 0600 UTC 19 January 1989 surface analysis by Sanders (1989) of temperature (°C, dashed) and pressure (mb, solid). Observations plotted using conventional notation.	111

ACKNOWLEDGEMENTS

I would like to thank Professor Wendell Nuss for his academic guidance, constructive criticism, and not least of all, his knowledge of the IDEA Lab. His ability to link current research to operational problems is valuable and much appreciated. This thesis would not have been written without his encouragement and patience. Thanks also to Professor Russell Elsberry, whose critical thinking and suggestions significantly improved this thesis. Professor Patrick Harr's comments kept this thesis statistically honest (otherwise liars can figure...) and Professor Patricia Pauley assisted with the objective analysis and provided comments about quasi-geostrophic vertical motion that helped clarify my ideas.

This thesis is dedicated to my wife, Kathy. Her talents as a graphic artist produced professional camera-ready figures, while her love and support have made this project (and the intervening deployment) worthwhile.

I. INTRODUCTION

A. THE SIGNIFICANCE OF RAPID CYCLOGENESIS

Rapidly deepening cyclones over the midlatitude oceans are of interest to both the professional mariner and meteorologist. From a meteorologist's perspective, rapid cyclogenesis is interesting because of possible physical differences between rapidly developing cyclones and "normal" extratropical cyclones. These differences have been extensively studied (e.g., Roebber 1984; Reed and Albright 1986; Uccellini 1990; Kocin and Uccellini 1990) with the goal of enhancing our knowledge of the physical processes that govern the formation and growth of all extratropical cyclones.

For the mariner, these storms result in significant additional costs in fuel and delayed arrivals. More importantly, rapid cyclogenesis can pose a real danger to the physical safety of ships and their crews when weather conditions deteriorate from marginal to extreme in a matter of hours.

Naval ships, particularly aircraft carriers (CV/CVN), have unique environmental requirements. Any sudden, especially unexpected, change of weather conditions will have a great impact on the conduct of flight operations. If the CV is operating in an area without shore-based divert fields available, a rapidly developing storm hazards the safety of airborne aircraft. Due to the nature of carrier flight operations, a minimum of three to six hours of warning is required before weather conditions deteriorate and make safe conduct of flight operations infeasible. Unfortunately, the current operational numerical

models have difficulty with these short-range forecasts because of their adjustment to initial conditions (e.g., Haltiner and Williams 1980; Doswell 1986) during the first 6-9 h. An enhanced ability to accurately diagnose the current state of the atmosphere (including vertical motions) will assist the forecaster in preparing these crucial short-range forecasts.

A significant factor that hinders the analysis and prediction of rapid cyclogenesis, or any other oceanic meteorological phenomena, is the paucity of maritime observations compared to the continents. Three major sources of data for oceanic regions are satellite imagery, commercial aircraft Pilot Reports (PIREPs), surface ship and buoy reports.

Since weather satellites became available, less emphasis has been placed on reports from weather ships. As budgets and spending resources tightened, these permanent oceanic observing platforms were phased out of service. As shown in Fig. 1, regular rawinsonde reports over the oceans are limited to isolated island stations. Satellite imagery is of vital importance, and useful upper- and low-level winds may be obtained through cloud-drift techniques. As described by Ohring (1990), satellite sounding methods are being refined. However, the sounding errors can potentially degrade the numerical models. Comparison with rawinsondes show that satellite soundings are least accurate near the surface and close to the tropopause. These techniques also degrade in cloudy regions. For these reasons, it is difficult to measure synoptic forcing objectively by satellite alone. If geostationary satellite data cannot be received (a common situation for ships at sea), satellite coverage may be limited to three or four polar orbiter passes per day at asynoptic times. Although PIREPs are also very useful, especially in tropical



Fig. 1. Location (dots) of regularly reporting rawinsonde stations (Ohring 1990).

regions, most commercial airlines routinely fly above the midlatitude winter tropopause. PIREPs are also asynoptic, and tend to be concentrated along a relatively few commercial routes. This leaves the surface data as the only routinely available, synoptic data source over the oceans. Consequently, techniques that make maximum use of surface data are most useful and potentially most informative.

B. OBJECTIVE

The goal of this study is to assess the ability of surface observations and subsequent derived analyses to generate an accurate diagnosis of the vertical velocity field in a

rapidly developing cyclone, subject to the constraints of quasi-geostrophic theory. Surface pressure and temperature fields will be used to construct Q vectors. As described by Hoskins and Pedder (1980), Q vectors point in the direction of the low-level ageostrophic flow, and are directed towards rising motion. Hoskins *et al.* (1978) show that $-2\nabla \cdot Q$ equals the forcing terms of the Omega equation as derived by Sutcliffe (1947). The divergence of the Q Vectors will be compared with available satellite imagery to see if significant convective or stratiform clouds are in areas of implied upward vertical motion. In addition, regions of Q vector convergence will be evaluated by correlating the observed Q Vector divergence to future 3-h to 6-h pressure changes of the storm. If a statistically significant correlation can be shown, this method would be useful for applications requiring short-range forecasts of rapidly deepening cyclones.

Section II of this thesis provides background on rapid cyclogenesis and the theoretical justification for use of Q vectors with surface data. Section III discusses data analysis. Section IV presents case studies of two Intensive Observation Period (IOP) cyclones from the Experiment on Rapidly Intensifying Cyclones over the Atlantic (ERICA), while the final section contains conclusions and recommendations.

II. BACKGROUND

A. PREVIOUS RAPID CYCLOGENESIS STUDIES

Rapid, or explosive, extratropical cyclogenesis has been studied by meteorologists for decades (e.g., Winston 1955; Pyke 1965). Sanders and Gyakum (1980) revived interest in the subject. In addition, the well-publicized 1979 Fastnet yacht race storm, the storm of 10 September 1978 in which the luxury liner *Queen Elizabeth 2* was damaged (NOAA 1979) and the "Presidents' Day Storm" that occurred 18-20 February 1979 along the middle Atlantic coast of the United States increased public awareness. Sanders and Gyakum defined a rapidly deepening extratropical low as a system that deepens at least one bergeron, which is defined as a deepening rate of $(1 \text{ mb h}^{-1} \text{ for } 24 \text{ h}) * (\sin \phi / \sin 60)$, where ϕ is the cyclone center latitude. Sanders and Gyakum found that these rapidly developing storms primarily occurred over and just to the north of the Kuroshio and Gulf Stream in the Pacific and Atlantic, respectively. Secondary maxima existed in the central Pacific and eastern Atlantic. They noted that most rapid cyclogenesis events occurred in the cold season (September through April in the Northern Hemisphere (NH)).

The exact physical processes responsible for rapid cyclogenesis are still a matter of debate (Uccellini 1990). Roebber (1984) concluded that the physical processes producing rapidly deepening cyclones were fundamentally different from baroclinically developed storms. He based his conclusion on a statistical analysis of the 24-h deepening rates for a one year sample of NH storms. Roebber found that one normal distribution curve could

fit normal cyclogenesis, while a separate normal distribution curve fit the "explosive" cyclogenesis cases. In addition, both Roebber (1984) and Farrell (1984) noted that cyclone development rates from baroclinic instability theory are less than those observed.

However, several studies (e.g., Roebber 1984; Reed and Albright 1986; Kocin and Uccellini 1990) have shown that most of the rapid deepening of a cyclone occurs during a relatively small portion of the storm's total life. This leads Uccellini (1990) to an alternate and more widely-held interpretation that rapid cyclogenesis is a result of "traditional" upper- and lower-level processes, including the release of latent heat, that interact in a more efficient manner over a relatively small period of time. If this is true, then "traditional" diagnostic tools such as quasi-geostrophic theory (e.g., Holton 1979) may be capable of producing accurate diagnostic and predictive fields.

Given that rapid cyclogenesis is an interaction of these processes, it is still not clear as to the relative importance of each of these processes. Winston (1955) believed that barotropic vorticity advection could explain most of the deepening observed during rapid cyclogenesis, while Petterssen (1956) noted that cyclogenesis occurred when an area of cyclonic vorticity advection in the upper troposphere moved over a low level quasi-stationary front. Uccellini (1984) and Wash *et al.* (1988) show that jet streaks can produce very significant divergence aloft, even in jets that have little curvature. Several recent studies (e.g., Sinclair and Elsberry 1986; Kocin and Uccellini 1990) show the presence of jet streaks, and their associated ageostrophic circulations, significantly influence rapid cyclogenesis. These results suggest that deep baroclinic forcing occurs

in these cyclones on a scale that potentially allows diagnosis of the effects of dynamic forcing through quasi-geostrophic ideas.

In addition to these upper-level processes, Uccellini (1990) lists four low-level processes that contribute to rapid cyclogenesis:

- (i) The thermal advection pattern in the lower troposphere in conjunction with the presence of low-level baroclinic zones and strong low-level winds;
- (ii) Sensible and latent heat fluxes in the boundary layer that act to fuel these systems;
- (iii) Decrease of static stability in the lower troposphere; and
- (iv) Mountain ranges.

The thermal patterns in the lower troposphere have long been recognized as being important in the formation and intensification of storms. Eliassen (Chap. 15, Petterssen 1956) notes that the baroclinic instability concepts of Charney (1947) and Eady (1949) lead to a low-level thermal and thermal advection structure that is important in the development of cyclones. The evolution of the thermal field into an "S-shaped" field during cyclogenesis has been noted for decades (e.g., Bjerknes and Solberg 1922), and more recently confirmed in cases of rapid cyclogenesis (Kocin and Uccellini 1990). This "S" pattern is associated with warm advection to the east of the storm and cold advection to the west of the storm. This thermal advection pattern is favorable for further deepening of the storm.

This low-level baroclinic forcing has a spatial scale on the order of the storm, so that quasi-geostrophic concepts should adequately describe these dynamics. If significant

low-level forcing exists, and the stability of the atmosphere is low, then this low-level baroclinic zone may be coupled to mid- and upper-tropospheric dynamics. The hypothesis here is that the use of Q vectors based upon surface data will provide an adequate diagnosis of the storm dynamics.

Sensible and latent heat fluxes due to cold air flowing over a relatively warm ocean north of the warm front appear to have an important role in rapid cyclogenesis. Most cases of rapid deepening occur over the ocean, and numerous diagnostic and model sensitivity studies have shown heat fluxes to be important in the development of rapid cyclogenesis (e.g., Petterssen *et al.* 1962; Uccellini *et al.* 1987; Mullen and Baumhefner 1988; Mailhot and Chouinard 1989; Nuss and Kamikawa 1990). Bosart (1981) notes that the preconditioning of the cold easterly flow ahead of the Presidents' Day storm by sensible heat from the ocean was crucial for the rapid intensification. However, Uccellini (1990) states that these studies do not explain rapid cyclogenesis events over land, and other model sensitivity studies (e.g., Danard and Ellenton 1980; Kuo and Reed 1988; Kuo and Low-Nam 1990) show that sensible and latent heat fluxes have little impact on the subsequent cyclogenesis. Uccellini states that these apparently conflicting results may either show a large dependence on the specific case being modeled or may be due to differing model boundary layer parameterizations. Although this study does not attempt to resolve the role of sensible and latent heat fluxes, Q vectors and their associated divergence field will be evaluated where these fluxes are significant. If these fluxes result from organized baroclinic forcing, Q vectors should implicitly account for the vertical forcing due to latent and sensible heat fluxes.

Surface heat and moisture fluxes into the atmospheric boundary layer and lower troposphere also reduces the low-level static stability in the vicinity of the storm. Studies (e.g., Eliassen 1962; Bosart 1981; Keyser and Carlson 1984) have shown that static stability plays an important role in controlling the strength of secondary circulations arising from jets and fronts. Wash *et al.* (1988) noted that a reduction in the static stability of the lower troposphere enhanced the vertical motion during rapid cyclogenesis over the Pacific Ocean. This increased vertical motion increased the magnitude of upper-level divergence and low-level convergence, which aided the development of the storm. Emanuel (1983) showed that the sensible and latent heat fluxes may decrease the symmetric stability and lead to regions that are conditionally unstable to slantwise convection.

This reduction in stability is probably crucial for low-level or surface-based diagnostics of vertical velocity to be representative of the deeper troposphere. That is, forcing near the surface in areas where the stability is low will be assumed to extend through the low- and mid-troposphere. By contrast, vertical circulations will remain relatively shallow and weak in areas of high static stability.

Uccellini (1990) notes that determining the relative importance of latent heat release in rapid cyclogenesis has remained elusive. Case studies by Johnson and Downey (1976), numerical experiments by Gall (1976) and model sensitivity studies by Chang *et al.* (1982) have shown latent heat release to be important to the rapidly developing cyclone. Emanuel (1985) showed that latent heat release focuses the vertical motion on a smaller scale, which then enhances the baroclinic processes that cause the storm to deepen.

Uccellini states that it is difficult to tell if the latent heat is directly lowering the surface pressure of the storm through hydrostatic considerations or indirectly deepening the cyclone by increasing the Laplacian of the diabatic terms in the Petterssen development equation. Uccellini also notes that the effects of latent heat release are difficult to separate from those of the boundary layer fluxes.

Latent heat release implies lowered static stability and greater coupling between the lower and upper troposphere. If latent heat is significant, quasi-geostrophic diagnostics may still be informative if the latent heating is organized by the baroclinic processes. However, substantial release of latent heat may distort a quantitative prediction of cyclogenesis from quasi-geostrophic terms only. Hoskins and Pedder (1980) noted that although Q vectors do not explicitly account for diabatic effects, Q vectors implicitly measure previous diabatic forcing through the diabatic effects on the secondary circulations. If the release of latent heat is a relatively unimportant forcing term when compared to vorticity advection and baroclinic forcing, then ignoring the diabatic terms in the quasi-geostrophic dynamics should still yield adequate results, but increased static stability may render a surface-based calculation less meaningful.

Uccellini (1990) suggests that rapid cyclogenesis is not the product of one or two discrete physical processes, but rather occurs by upper- and lower-tropospheric processes acting in concert with diabatic processes. In his view, rapid deepening occurs when these processes act together, perhaps in a "nonlinear synergistic" manner. The objective here is to demonstrate that vertical velocities resulting from rapid cyclogenesis can be diagnosed--at least in a qualitative manner--with surface-based Q vectors.

B. CALCULATING VERTICAL MOTION

Although synoptic-scale vertical motions are small, they are vital to understanding processes associated with cyclogenesis. Dunn (1991) notes that knowledge of the vertical motion field provides insight into the distribution of sensible weather elements such as clouds and precipitation. Vertical motions are essential to maintain the atmosphere in geostrophic and thermal balance. Consequently, vertical motion is a useful diagnostic quantity during cyclogenesis. A qualitative real-time diagnosis of vertical motion in the atmosphere can also provide a quality-control check on the various numerical products. However, calculating synoptic-scale vertical motion in the atmosphere has always been a difficult task. A scaling of the momentum equations (e.g., Holton 1979) shows that synoptic-scale vertical motions are on the order of a few cm s^{-1} , or about two orders of magnitude less than the horizontal winds. Such small values preclude direct measurement. This dilemma has led meteorologists to indirect methods to estimate vertical velocities.

1. Quasi-Geostrophic Vertical Motion

The Sutcliffe (1947) quasi-geostrophic theory of development is based upon the ageostrophic components of the wind continually restoring the geostrophic balance (Hoskins *et al.* 1978). Quasi-geostrophic theory provides a conceptual framework for the synoptic-scale dynamic and thermal forcing that explains the secondary circulations. The quasi-geostrophic omega equation is a diagnostic equation for the vertical velocity, and may be expressed as

$$\left(\sigma \nabla^2 + f_0^2 \frac{\partial^2}{\partial p^2} \right) \omega = f_0 \frac{\partial}{\partial p} \left[\mathbf{v}_g \cdot \nabla \left(\frac{1}{f_0} \nabla^2 \Phi + f \right) \right] + \nabla^2 \left[\mathbf{v}_g \cdot \nabla \left(\frac{-\partial \Phi}{\partial p} \right) \right] \quad (1)$$

using the notation of Holton (1979) and ignoring diabatic and frictional terms. The left side of the equation is the "three-dimensional Laplacian" of the vertical motion, the first term on the right side is the differential advection of geostrophic vorticity, and the last term is the horizontal Laplacian of thermal advection by the geostrophic wind.

Although this equation provides vertical velocities in terms of observed winds and temperatures, solving directly for ω is not commonly done in an operational environment, even with the proliferation of micro-computers. The solution to (1) requires observations at multiple levels in the atmosphere, and these observations over the ocean frequently do not exist. A direct solution for ω requires knowledge of the lateral boundary conditions that are normally unknown for a regional analysis. Additionally, inverting the three-dimensional differential operator on the left side becomes complex when static stability (σ) is allowed to vary over the domain. Therefore, in operational settings, it is normally assumed that the left side of (1) is proportional to $-\omega$. Durran and Snellman (1987) note the errors introduced by this assumption by showing that the right side of (1) is a noisier field than ω and that the approximation is best in the middle-troposphere. The terms on the right side are commonly estimated by using the vorticity advection at 500 mb and assuming that the Laplacian of the thermal advection is proportional to the negative of thickness advection. Durran and Snellman again point out potentially serious errors that may result from these simplifications.

Assuming that one could accurately calculate the vorticity and thermal forcing terms, it may be misleading to consider the individual terms separately. Trenberth (1978) shows that the advection of thermal vorticity by the geostrophic wind is a component of both terms on the right side of (1). This component has a relatively large magnitude but opposite sign in each of the terms on the right side of (1). This common component means that the terms on the right side of (1) are not independent. As discussed by Hoskins *et al.* (1978) and Durran and Snellman (1987), this common term changes as the mean wind speed varies. This will change the relative magnitudes between the right side terms, and may even alter the sign of one term. The final result will still be correct, but there is little physical meaning in the individual terms. Quasi-geostrophic vertical motion is not caused by either term on the right side of (1), but rather is an attempt (along with differential ageostrophic horizontal velocity) to restore geostrophic and thermal wind balance that is being simultaneously destroyed by the thermal advection of the geostrophic wind. Another problem with a large canceling common component is the potential for catastrophic cancellation (e.g., Gerald and Wheatley 1990) when solving the right side of (1) numerically. Catastrophic cancellation results in the loss of all significant digits, and the answer produced would be meaningless.

a. Q Vectors

Hoskins *et al.* (1978) derive an alternate method of calculating the left side of (1) through the use of *Q* vectors. Neglecting variations in the Coriolis parameter, Hoskins *et al.* show that

$$\left(\sigma \nabla^2 + f_0^2 \frac{\partial^2}{\partial p^2} \right) \omega = -2 \nabla \cdot \mathbf{Q} \quad (2)$$

where \mathbf{Q} is defined as

$$\mathbf{Q} = \left[-\frac{\partial u_g}{\partial x} \frac{\partial \theta}{\partial x} - \frac{\partial v_g}{\partial x} \frac{\partial \theta}{\partial y}, -\frac{\partial u_g}{\partial y} \frac{\partial \theta}{\partial x} - \frac{\partial v_g}{\partial y} \frac{\partial \theta}{\partial y} \right]. \quad (3)$$

The components of this vector are orthogonal and can be directly related to quasi-geostrophic frontogenesis in the zonal (x) and meridional (y) directions. \mathbf{Q} vectors have several useful properties. First, the distribution of \mathbf{Q} vectors allows deduction of the vertical and horizontal ageostrophic secondary circulations. Hoskins *et al.* describe \mathbf{Q} vectors as "a constant times the vector rate of change of horizontal potential temperature gradient on a fluid particle implied by the geostrophic motion alone" (frontogenesis). They show that the right side of (1) is equal to -2 times the divergence of \mathbf{Q} as given in (2). Hoskins and Pedder (1980) explain that \mathbf{Q} vectors point in the direction of the low-level ageostrophic motion, and toward the rising motion. Durran and Snellman (1987) state that the magnitude of the \mathbf{Q} vector is approximately proportional to the strength of the ageostrophic horizontal wind.

Because Sanders and Hoskins (1990) realized that the above explanations of \mathbf{Q} vectors may be difficult to quickly visualize in an operational setting, they described another way to obtain \mathbf{Q} vectors. Their method is to follow an isotherm with cold air to the left, and calculate the vector change of the geostrophic wind. The magnitude of the

Q vector is proportional to the magnitude of the temperature gradient multiplied by the vector rate of change of the geostrophic wind, and the direction of the Q vector is obtained by rotating the vector 90° clockwise. Examples of Q vectors using the surface pressure and the 1000-500 mb thickness field in place of the surface isotherms are shown in Fig. 2. This method of calculation can be applied qualitatively with relative ease to synoptic charts without making a complete set of calculations on a grid. Finally, Q vectors can be calculated from a single pressure level, and do not suffer from having a large magnitude terms with opposite signs. This makes Q vectors numerically more stable than the conventional approach in (1). Because the left side of (1) is still a three-dimensional "Laplacian", the same approximations relating this operator to the actual vertical velocity apply when using Q vectors as they do when using the traditional terms.

b. Limits to Quasi-Geostrophic Theory

Quasi-geostrophic theory is a powerful method of interpreting synoptic-scale motions in the atmosphere, and is the theoretical basis by which vertical motion is evaluated from operational numerical models output (Dunn 1991). However, it is necessary to understand the limitations of quasi-geostrophic dynamics when using this tool to model the atmosphere. Quasi-geostrophic theory assumes large-scale flow in which the geostrophic and hydrostatic approximations are valid. Thus, the Rossby number (Ro), which is the ratio between scales of the fluid's acceleration and the Coriolis force, must be $\ll 1$. Holton (1979) derives (1) by making several simplifications to the vorticity equation, invoking the beta-plane approximation, and assuming that diabatic effects are negligible compared to horizontal temperature advection and adiabatic heating

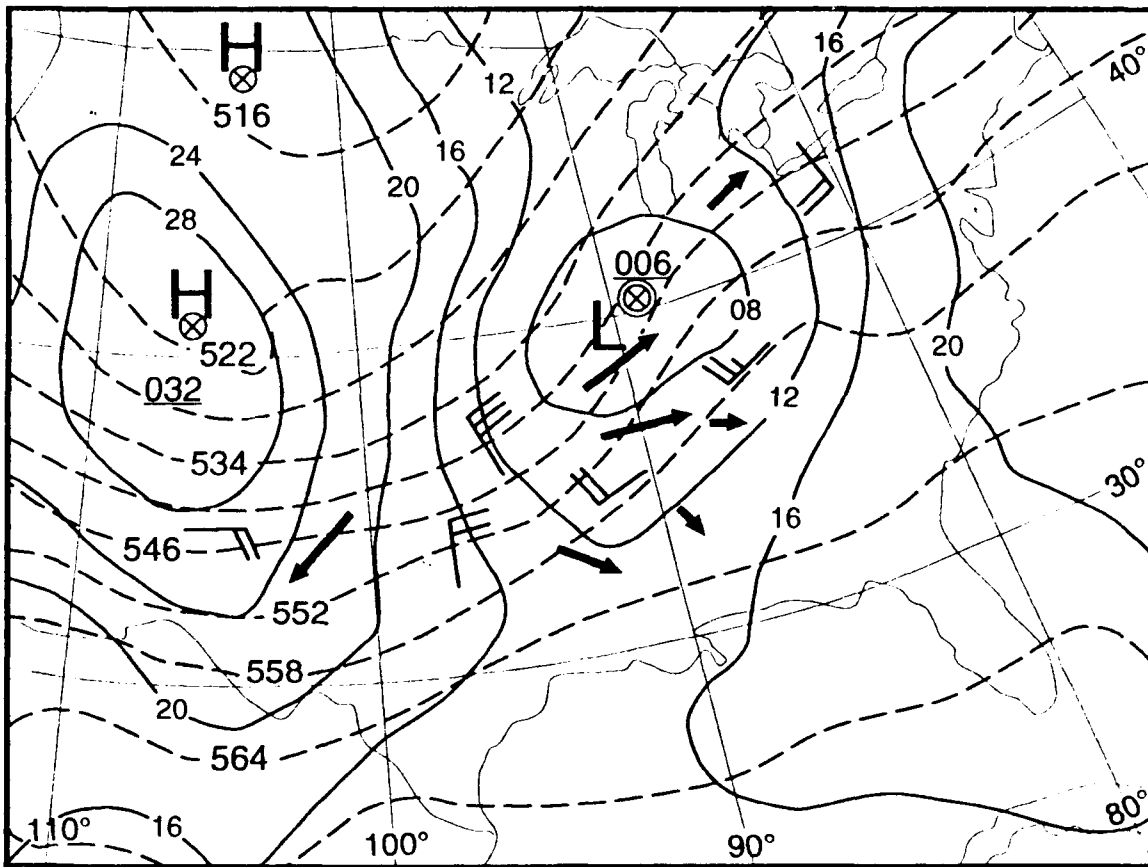


Fig. 2. Isobars (solid, 4 mb intervals) and 1000-500 mb thickness (dashed, 60 dam intervals). Surface geostrophic wind in conventional notation, and Q vectors in bold arrows (Sanders and Hoskins 1990).

and cooling terms. Holton notes that these approximations are most accurate for midlatitude synoptic-scale motions.

In a midlatitude cyclone environment, these approximations are tested most severely in the vicinity of jet streaks. Uccellini *et al.* (1984) show that Ro approaches unity near the entrance region of intense jet streaks, and Bluestein and Thomas (1984) state that quasi-geostrophic vertical motions may not even be qualitatively correct in regions where the trajectories curve sharply near jet streaks. As stated above,

jet streaks appear to be a common feature associated with rapid cyclogenesis, and may limit the usefulness of quasi-geostrophic theory in rapid cyclogenesis.

Several (e.g., Gyakum 1983; Pauley and Nieman 1991) studies have discussed the inability of adiabatic quasi-geostrophic theory to produce deepening rates similar to those observed in rapidly deepening cyclones. Pauley and Nieman numerically simulated the *Queen Elizabeth 2* storm, and showed that upward vertical velocities obtained from quasi-geostrophic dynamics were too low in regions of significant latent heat release. Quasi-geostrophic theory also over-estimated the magnitude of the sinking air in the wake of the storm, primarily due to ageostrophic advections being ignored.

Applying quasi-geostrophic theory near the surface also stretches the approximations in the theory. Surface friction can create large deviations between the geostrophic and observed winds. The largest curvature in the isobars occurs in the lower troposphere, which results in winds that are super- and sub-geostrophic around regions of high and low pressure, respectively. Although diabatic terms can be included in the quasi-geostrophic theory, regions of large sensible and latent heat fluxes may not be evaluated correctly without including the diabatic forcing. The surface is the lower boundary at which the vertical motion is assumed to be zero (over level terrain). To calculate vertical motions based upon surface temperatures and geostrophic winds, the temperature field must be considered to be representative of the temperature gradients existing in the lower troposphere, while the geostrophic winds are assumed to be comparable to the winds immediately above the boundary layer. Although quasi-geostrophic theory is deficient in modeling the time evolution of fronts and their

subsequent vertical motion (Williams 1972), quasi-geostrophic theory provides a qualitatively correct diagnosis of the secondary circulation induced by a front.

Clearly, these are not trivial limitations on quasi-geostrophic theory. This study will demonstrate that, despite these approximations, useful information is obtained when quasi-geostrophic vertical motions are calculated from surface data.

c. *Quasi-geostrophic Theory as Applied to Rapidly Developing Cyclones*

Despite these potential limitations, previous studies have shown that quasi-geostrophic theory has considerable validity in regions of rapid cyclogenesis. Kuo *et al.* (1991) conducted a numerical experiment in which they simulated a rapid cyclogenesis event (the *Queen Elizabeth 2* storm) with pressure falls of $37 \text{ mb (24 h)}^{-1}$. They found quasi-geostrophic vertical motion to be comparable in both magnitude and areal distribution to the primitive-equation model vertical motion providing diabatic terms were accounted for. Nuss and Kamikawa (1990) studied one storm east of Japan that deepened $33 \text{ mb (36 h)}^{-1}$, and another low that deepened $29 \text{ mb (24 h)}^{-1}$. Nuss and Kamikawa found that kinematic vertical velocities were similar to quasi-geostrophic omega fields.

These studies provide confidence that quasi-geostrophic theory produces at least a qualitatively correct diagnosis of the storm vertical velocity. Although conditions in a rapidly developing cyclone may be extending quasi-geostrophic theory beyond conditions in ordinary cyclones, the goal is to demonstrate that quasi-geostrophic reasoning may be an appropriate tool to analyze rapidly deepening cyclones.

d. Q Vectors Applied to Surface Data

As discussed above, rapidly developing cyclones typically have low stability and a strong low-level thermal signature. If the low-level temperature gradient is representative of the mean tropospheric thermal structure, and the stability is sufficiently low to couple low-level forcing to mid-tropospheric vertical motions, then surface-based Q vectors should give an accurate qualitative diagnosis of the storm's current vertical velocity. The divergence of the Q vectors is calculated, and the implied vertical motion is evaluated to verify this method. In addition to the approximations made in quasi-geostrophic theory, the use of Q vectors with surface data introduces sources of error. Potential errors arise due to the neglect of any boundary layer effects, the use of the surface temperature field as a proxy for the tropospheric thermal structure and the neglect of possible phase differences between the surface and mid-level vertical velocity forcing. Errors may also result from inaccurate objective analyses of the surface pressure and temperature fields, and from the finite difference calculations.

2. Verifying Vertical Motion Calculations

Several methods are used in this study to verify the Q vector computed vertical motion. First, direct vertical velocity measurements, when available from aircraft, can be compared to the calculated vertical motion. However, aircraft vertical velocity measurements, even when averaged in time, may not be representative of the vertical motion on an 80 km grid, especially in the vicinity of fronts. Second, a comparison can be made with the clouds as depicted by satellite imagery. Limitations to this method include the inability to detect rising but unsaturated air, and the difficulties in determining

the structure of lower layers of clouds, especially in infrared (IR) imagery of convective clouds below a layer of cirrus.

Another evaluation of the surface vertical velocity calculations is a comparison with future 3-h and 6-h pressure tendencies. Cyclones in the midlatitudes with sustained significant upward vertical motions likely have considerable divergence aloft. For developing systems in which the upper-level divergence is greater than the low-level convergence, regions of upward motion should be characterized by falling surface pressures. According to the quasi-geostrophic theory upon which the vertical velocities are based, an imbalance in the pressure gradient and Coriolis force will tend to be restored on the time scale of the inertial period, as opposed to minutes or days. Thus, sustained upward (downward) vertical velocities should be manifest as a pressure fall (rise) for several hours into the future. Although not tested on an actual case study, Zwack and Kabil (1988) analytically demonstrated and modeled a strong correlation between current lower- and mid-tropospheric vertical velocities and the previous 3 h surface pressure tendencies, which supports the use of pressure changes as a verification of vertical motion.

C. EXPERIMENT ON RAPIDLY INTENSIFYING CYCLONES OVER THE ATLANTIC

The Experiment on Rapidly Intensifying Cyclones over the Atlantic (ERICA) was conducted between December 1988 and February 1989 (Hadlock and Kreitzberg 1988). As stated by Hadlock and Kreitzberg, the objectives of ERICA were to:

- (i) Understand the fundamental physical processes occurring in the atmosphere during rapid intensification of cyclones at sea;
- (ii) Determine those physical processes that need to be incorporated into dynamical prediction models through efficient parameterizations if necessary; and
- (iii) Identify measurable precursors that must be incorporated into the initial analysis for accurate and detailed operational model predictions.

To accomplish these objectives, measurements were obtained during eight Intensive Observation Periods (IOP) when storms within the ERICA area (Fig. 3) were forecast to meet the criterion of deepening at least 10 mb (6 h)^{-1} for at least 6 h. Each IOP lasted about 36 h. The cyclones that developed during IOP 3 and IOP 5 were chosen for this study because of their relatively good surface data coverage, availability of aircraft observations, and their typical rates of development. Whereas these storms deepened between 27 and 32 mb in 24 h, an extreme rapidly developing cyclone in IOP 4 deepened 60 mb $(24 \text{ h})^{-1}$. By contrast, the storm in IOP 8, only deepened 15 mb $(24 \text{ h})^{-1}$.

Data collection efforts were concentrated over the data-sparse oceanic regions. ERICA involved a complex multi-platform, multi-agency observing system to maximize the data set. Special data sources included research aircraft, surface buoys, coastal marine (C-Man) stations, commercial and naval ships of opportunity, and more frequent land-based soundings.

Observations from the WP-3D ERICA aircraft were important to this study. Aircraft observations of surface pressure and flight-level winds provided precise locations of the surface low pressure centers. ERICA aircraft also directly measured vertical

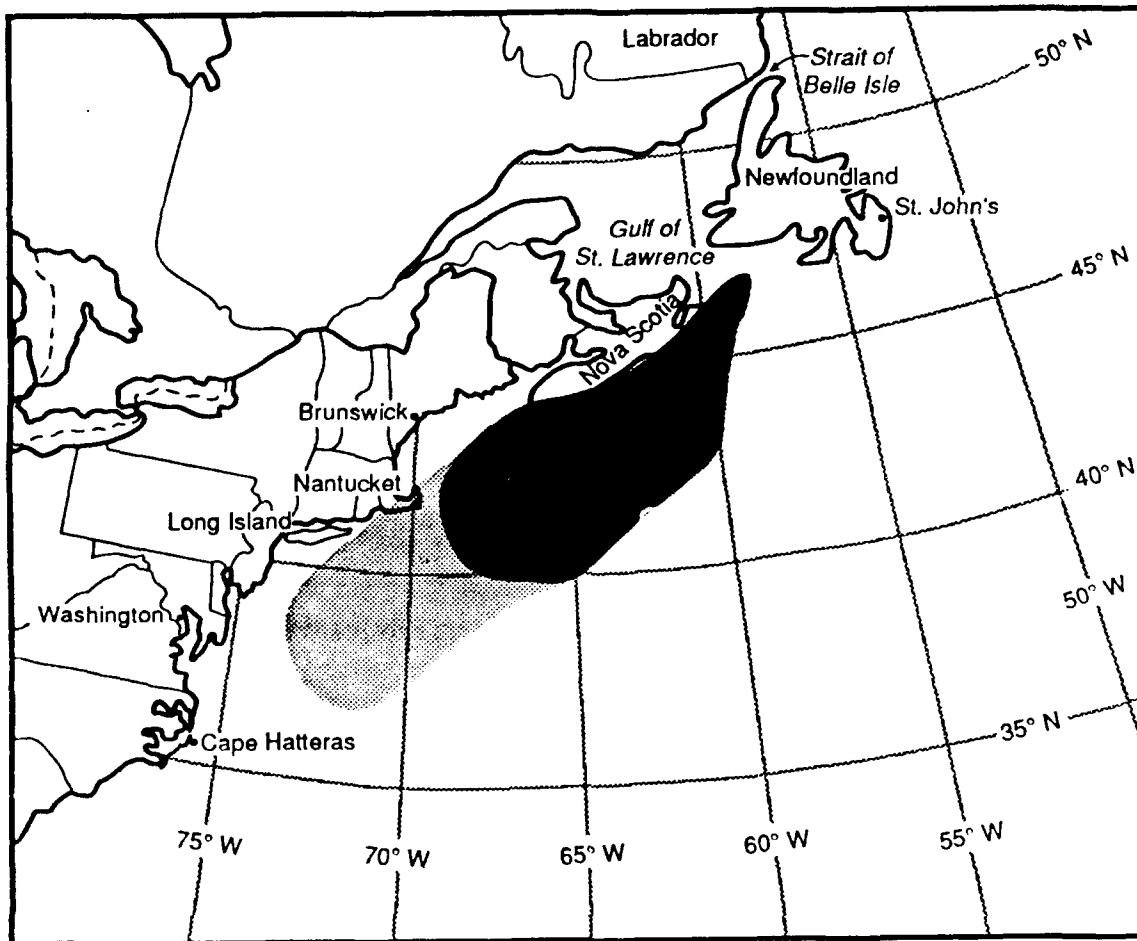


Fig. 3. Primary (dark stippling) and secondary (light stippling) areas where "ERICA-type" storms are most likely to occur (Hadlock *et al.* 1989).

velocity for comparison with the vertical velocity calculated from the Q vector divergence field. Four WP-3D missions were flown in each of the IOP 3 and IOP 5 cyclones.

Surface data consisted of the ship reports, operational coastal moored buoys, four deep water moored buoys, and about 100 drifting buoys that were deployed from Navy P-3 aircraft. The buoys were deployed in such a manner as to initially achieve 200 km resolution. The actual buoy patterns during the IOP 3 and IOP 5 cyclones are shown in Fig. 4 and Fig. 5, respectively. The drifting buoy reports include location (accurate to

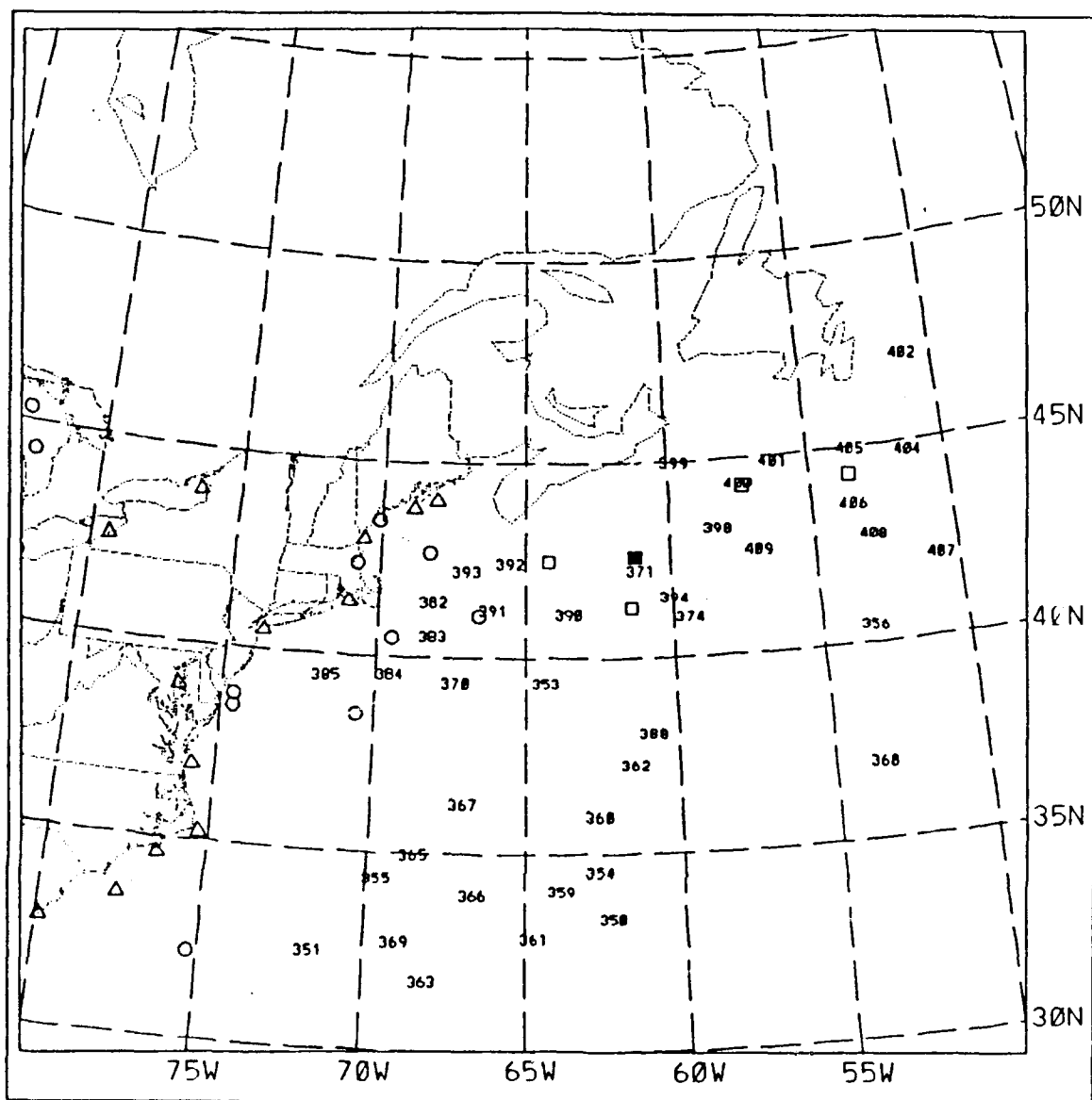


Fig. 4. Location of deep-water moored buoys (squares), coastal moored buoys (circles) C-Man stations (triangles) and ERICA drifting buoys (numbers) as of 18 December 1988 (Hadlock *et al.* 1989).

within 500 m), pressure, air temperature and sea-surface temperature. Buoy observations that were stored every ten minutes were transmitted via satellite several times a day. Drifting buoys generally survived between one to three months. All commercial ship

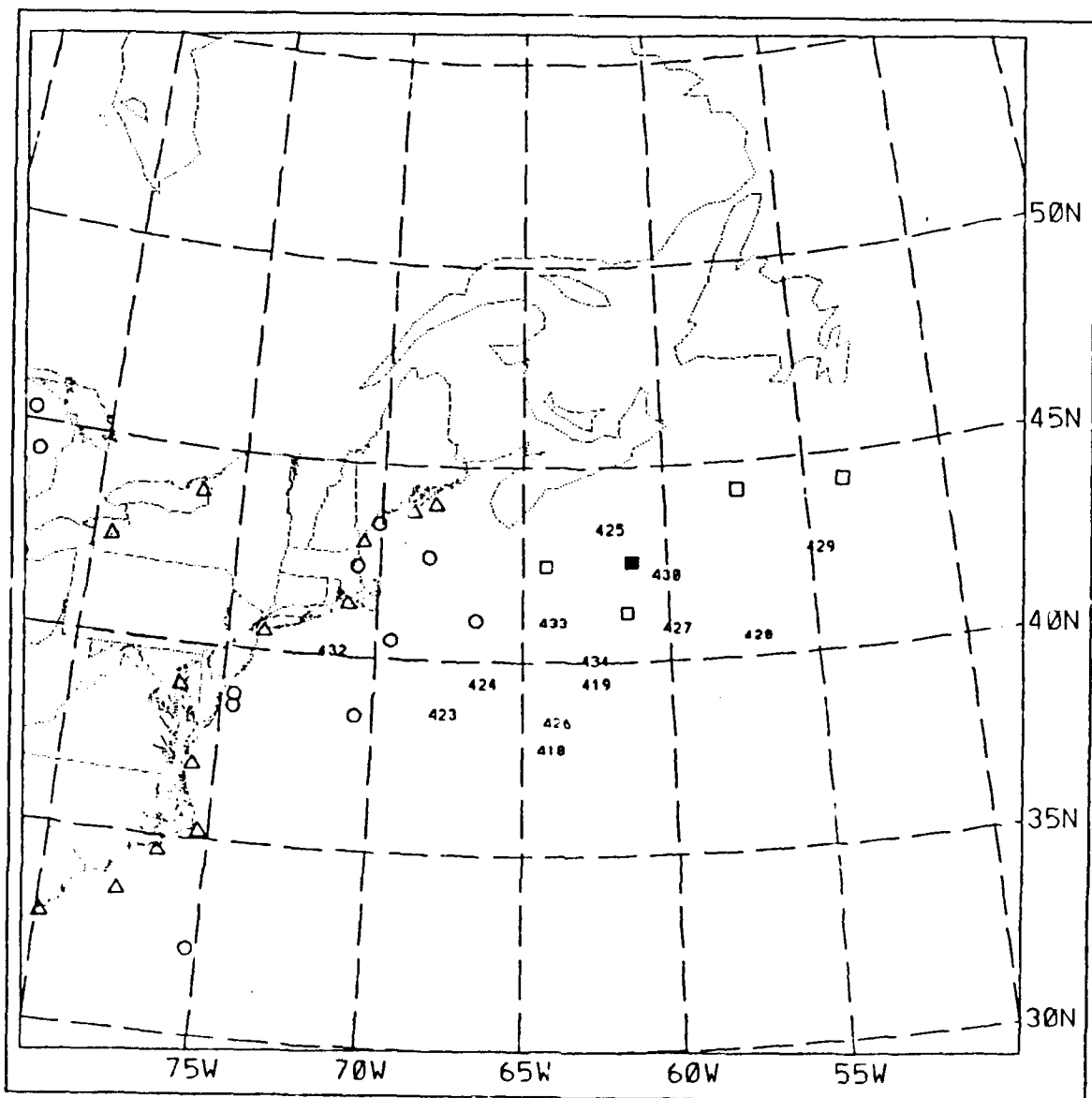


Fig. 5. As in Fig. 4, except for 19 January 1989.

observations, including those received by the National Climatic Data Center by mail, were added to the data set, after being quality checked. Ships in the ERICA study area were requested to transmit at least 3-h observations.

III. DATA ANALYSIS

A. ANALYSIS METHOD

Hand and objective surface analyses were produced by the author every 3 h for the duration of IOP 3. Although hourly airways observations provide good temporal and spatial resolution over the eastern U.S. and southeastern Canada, the density of these observations greatly diminishes north of 50°N. Producing accurate surface temperature and pressure analyses over the western North Atlantic, or any oceanic region, is a much more challenging task. In addition to a general sparsity of data (when compared to most land masses) different types of data must be integrated into the analysis. As Sanders (1990) states, these data vary in both their reliability and timeliness.

The hand-drawn oceanic pressure and temperature analyses for IOP 3 were accomplished using ship, C-MAN platform and moored buoy observations, along with the ERICA drifting buoys. Geostationary Operational Environmental Satellite (GOES) imagery was used to assist in locating the position of surface fronts and low pressure centers. When available, ERICA aircraft observations of low-level pressures and winds also assisted in providing an accurate location of the storm. Since most ship reports are at synoptic (every 6 h) times (Sanders 1990), the intermediate 3-h surface analyses were based upon buoy, satellite and aircraft observations along with forward and backward continuity in time.

Although aircraft and satellite data were used to derive the surface analyses and verify vertical velocity implied by the Q vectors, the surface analyses were based mainly on ship and buoy observations. The primary use for both satellite imagery and aircraft data was to locate the center of the surface low pressure and any associated fronts. Gradients of pressure and temperature, which are crucial to calculating Q vectors, were not directly affected by the satellite and aircraft data; therefore the Q vectors are not completely dependent upon the tools that will partially verify the vertical motion.

Table 1 and Table 2 list the number of drifting buoy observations and the total number of surface observations for the IOP 3 and IOP 5 cyclones, respectively. The drifting buoys significantly aided the analysis of both IOPs, although the location of the buoys with respect to critical surface features (e.g., centers of low pressure, frontal locations) was more important than the numbers of drifting buoys. Although the goal is to produce an operational method (using data available operationally) to diagnose rapidly developing cyclones, proof of the soundness of the technique was done using the best surface data-set available. Further studies are required to show if the drifting buoy data are essential to the success of this diagnosis.

The National Meteorological Center (NMC) final analyses are used for all upper-air and thickness analyses referenced in later sections of this study. These upper-air analyses are 12 hourly and do not contain detailed observations made in ERICA, but are internally consistent.

Table 1. NUMBER OF DRIFTING BUOY OBSERVATIONS AND NUMBER OF TOTAL SURFACE MARINE OBSERVATIONS FOR THE IOP 3 CYCLONE.

Time (DDHH UTC December 1988)	Number of Drifting Buoy Observations	Number of Marine Observations	Percent Drifting Buoy Observations
1700	38	130	29
1703	38	92	41
1706	38	134	28
1709	38	84	45
1712	38	144	26
1715	38	99	38
1718	38	135	28
1721	38	82	41
1800	37	135	27
1803	37	94	39
1806	37	141	26
1809	37	77	48
1812	37	137	27
1815	37	102	36
1818	37	135	27
1821	37	90	41
1900	35	125	28

1. Comparison of Hand-drawn Surface Analyses

After the hand analyses produced by the author for IOP 3 were completed, they were compared to the surface analyses drawn by Sanders (Sanders 1989), and to the track and central pressure analysis produced by Forbes (Hadlock *et al.* 1989). Forbes'

Table 2. NUMBER OF DRIFTING BUOY OBSERVATIONS AND NUMBER OF TOTAL SURFACE MARINE OBSERVATIONS FOR THE IOP 5 CYCLONE.

Time (DDHH UTC January 1989)	Number of Drifting Buoy Observations	Number of Marine Observations	Percent Drifting Buoy Observations
1818	13	108	12
1821	14	56	25
1900	14	84	17
1903	14	57	25
1906	14	87	16
1909	14	53	26
1912	14	108	13
1915	14	61	23
1918	13	96	14
1921	13	60	22
2000	13	96	14
2003	13	50	26
2006	13	82	16
2009	13	52	25
2012	13	110	12

analyses of the storm tracks and central pressures were constructed about six weeks after the completion of the field experiment, before the complete set of aircraft and ship observations were available. Sanders' analyses were drawn at a later time and with a more complete data set.

As shown in Fig. 6, the minimum central pressures for the three hand analyses for IOP 3 are in good agreement, and are 6-10 mb deeper than the NMC analyses used

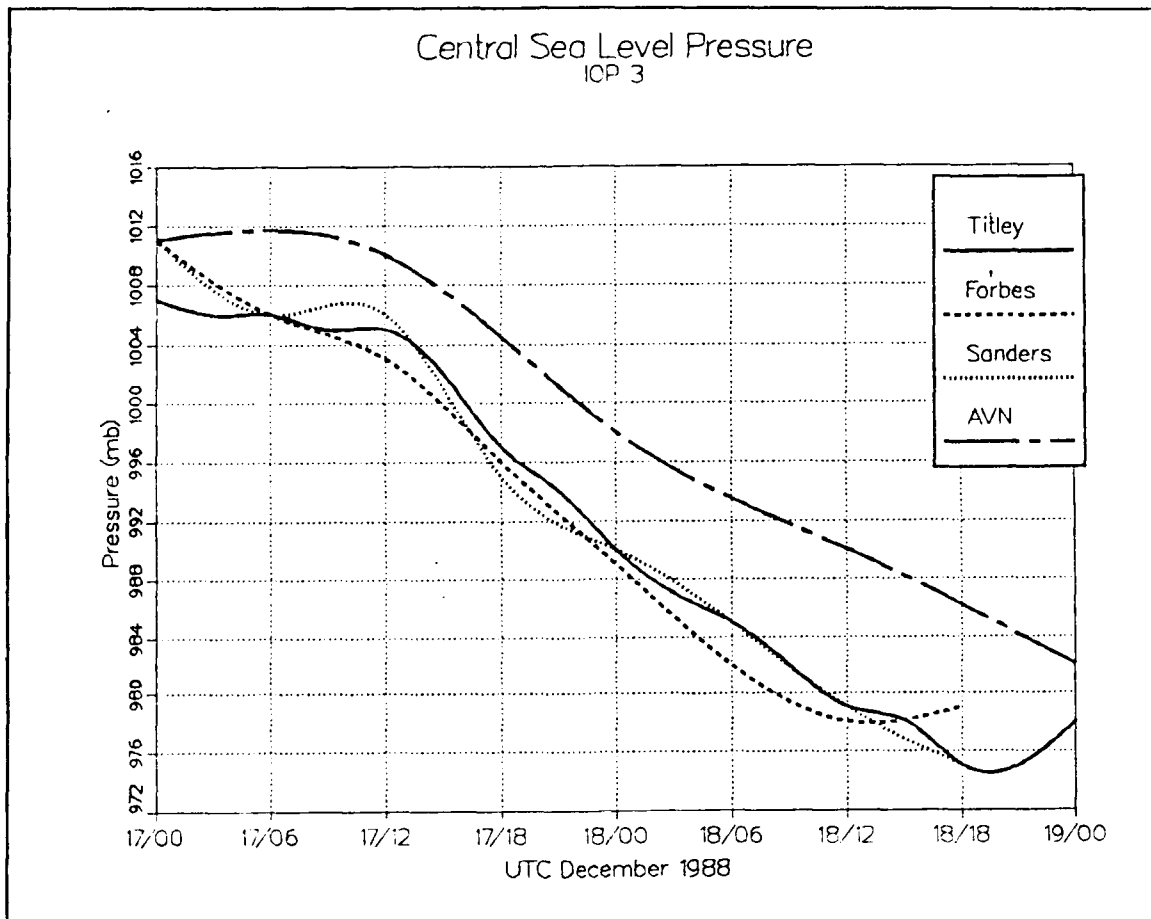


Fig. 6. Analyzed central pressure (mb) vs. time for IOP 3.

in the spectral model aviation (AVN) run (Petersen and Stackpole 1989). Sanders (1990) found similar discrepancies with the NMC analyses for all the ERICA IOPs. The locations of the storm center agreed well among the non-real-time, hand analyses, and the surface pressure and thermal structure in the author's and in Sanders' analyses closely matched each other. Based upon the close agreement of hand analyses throughout the IOP 3 cyclone, Sanders' analyses were used as the baseline charts for the IOP 5 storm.

2. Obtaining the Gridded Fields

The next step was to transform these surface pressure and thermal analyses into fields on a 40 x 36 grid with 80 km spacing. The central locations on the Lambert Conformal map grid for the IOP 3 and IOP 5 case studies were 42°N 70°W and 42°N 65°W respectively. This was accomplished by analyzing the data using an objective analysis scheme, then iteratively "bogussing", or adding artificial observations to the real data, to force the objective analysis to conform to the previously derived hand analysis. Although this process takes several iterations with an objective analysis scheme, it is more efficient than manually gridding the approximately 100,000 data points that were generated in this study.

Ship and buoy data, along with aircraft data below 1000 m and within 90 minutes of synoptic time were objectively analyzed to the grid using a Barnes (1964, 1973) analysis scheme. The first guess for the initial time was the NMC final analysis. Subsequent first guesses were the pressure and temperature fields from the previous 3-h objective analysis.

The objective gridded analysis was compared with the author's analysis for IOP 3 or Sanders' analysis for IOP 5. Over the land in general, and particularly over the United States, the density of observations produced an objective analysis very close to that obtained by hand. The only exceptions occurred when bad data contaminated the analyses. Poor data points were normally caused by transposed digits or other communication errors. Once the erroneous data were removed, the objective analysis over land was very good.

Over the ocean, sparse and unevenly distributed data along with occasionally conflicting observations from buoys and ships created the need for a careful evaluation of each observation as has been described by Sanders (1990). Even after bad buoy and ship observations had been removed, considerable problems remained with the objective analysis. A relatively large scan radius for including observations into a grid value ensured that the entire area was affected by the current data as opposed to maintaining the first guess in places where there were no observations. However, the large radius of influence simultaneously weakened regions of strong gradients. This was especially true if the data were distributed unevenly with respect to the gradient. These problems were solved by bogussing. These bogus observations were placed at selected locations to force the objective analysis to agree with the hand analysis. The objective analysis was then rerun with the bogus observations included. If necessary, this cycle was repeated until the objective analysis agreed as closely as possible with the hand analysis. Using this iterative process, gridded analyses of surface pressure and temperature were produced for every three hours during the IOP. Table 3 and Table 4 list the number of bogus pressure and temperature observations inserted at each analysis time for the IOP 3 and IOP 5 cyclones, respectively.

Typical examples of Sanders' hand analyses, the author's hand analyses and the subsequent objective analyses (after the addition of the bogus observations) are shown in Fig. 7, Fig. 8 and Fig. 9 respectively. While the objective analysis (Fig. 9) failed to depict the two separate closed low pressure systems, the central pressure of the storm was

Table 3. NUMBER OF BOGUS PRESSURE AND TEMPERATURE OBSERVATIONS INSERTED INTO THE IOP 3 ANALYSES.

Time (DDHH UTC December 1988)	Number of Bogus Pressure Observations	Number of Bogus Temperature Observations
1700	36	3
1703	69	4
1706	42	3
1709	8	0
1712	19	0
1715	19	1
1718	4	0
1721	10	1
1800	60	4
1803	5	0
1806	6	0
1809	46	0
1812	32	6
1815	28	0
1818	3	0
1821	57	0
1900	45	0

within 1 mb of the hand analyses, and the pattern of both isobars and isotherms closely agreed with the hand analyses.

Table 4. NUMBER OF BOGUS PRESSURE AND TEMPERATURE OBSERVATIONS INSERTED INTO THE IOP 5 ANALYSES.

Time (DDHH UTC January 1989)	Number of Bogus Pressure Observations	Number of Bogus Temperature Observations
1818	13	0
1821	7	4
1900	23	3
1903	2	4
1906	6	7
1909	4	7
1912	11	5
1915	17	7
1918	20	2
1921	37	17
2000	9	44
2003	43	13
2006	18	30
2009	27	16
2012	37	20

3. Calculating Q Vectors and the Associated Divergence Field

Once the gridded surface pressure and temperature analyses were in good agreement with the hand analyses, Q vectors were calculated using a first-order centered difference approximation of (3). $\nabla \cdot \mathbf{Q}$ is subsequently obtained by first-order finite differencing. Boundary values are extrapolated from the closest interior grid point. A

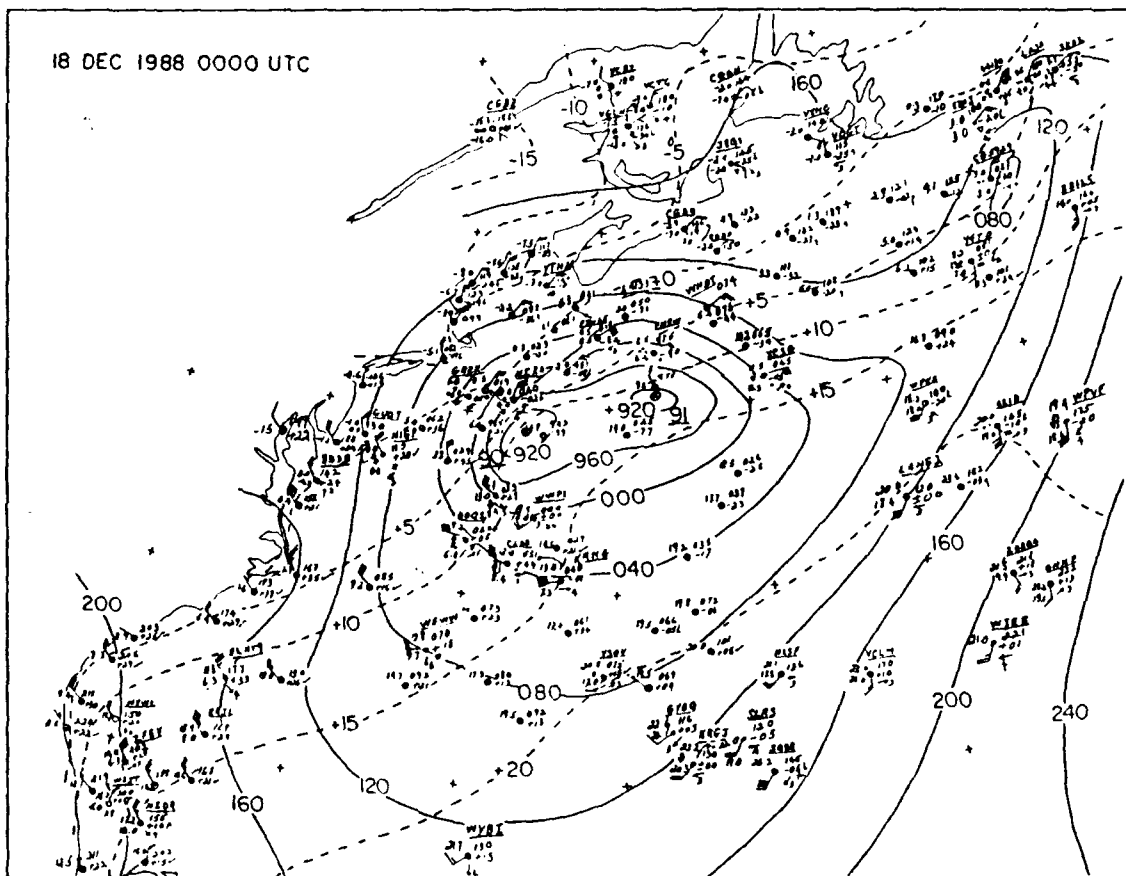


Fig. 7. Surface pressure (mb) and temperature ($^{\circ}\text{C}$) analysis by Sanders (1989) for 0000 UTC 18 December 1988. Contour interval is 4 mb for pressure and 5°C for temperature.

nine point low-pass smoothing algorithm (Haltiner and Williams 1980) is then applied to the divergence field.

4. Evaluating the Q Vector Divergence Field

As a first test of the validity of the Q vector divergence fields, subjective comparisons to a conceptual model of an extratropical cyclone were made. The divergence fields of the Q vectors were also subjectively evaluated against visible and IR satellite imagery to see if areas of extensive stratiform or convective clouds correlated

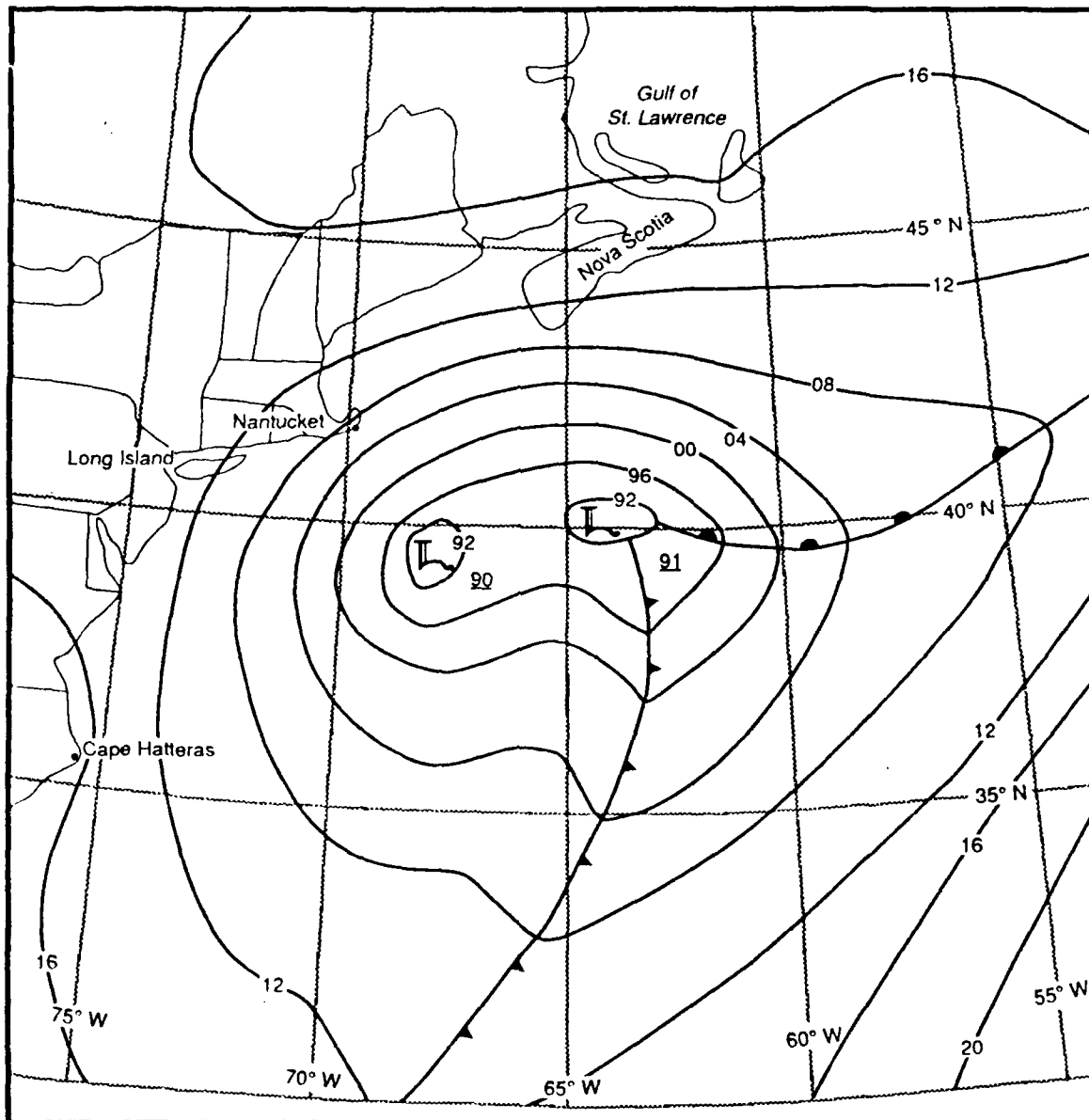


Fig. 8. Surface pressure (mb) analysis by Titley for 0000 UTC 18 December 1988. Contour interval is 4 mb.

with regions of Q vector convergence. Along with these subjective evaluations, two objective methods of measuring the "goodness" of the divergence field were employed.

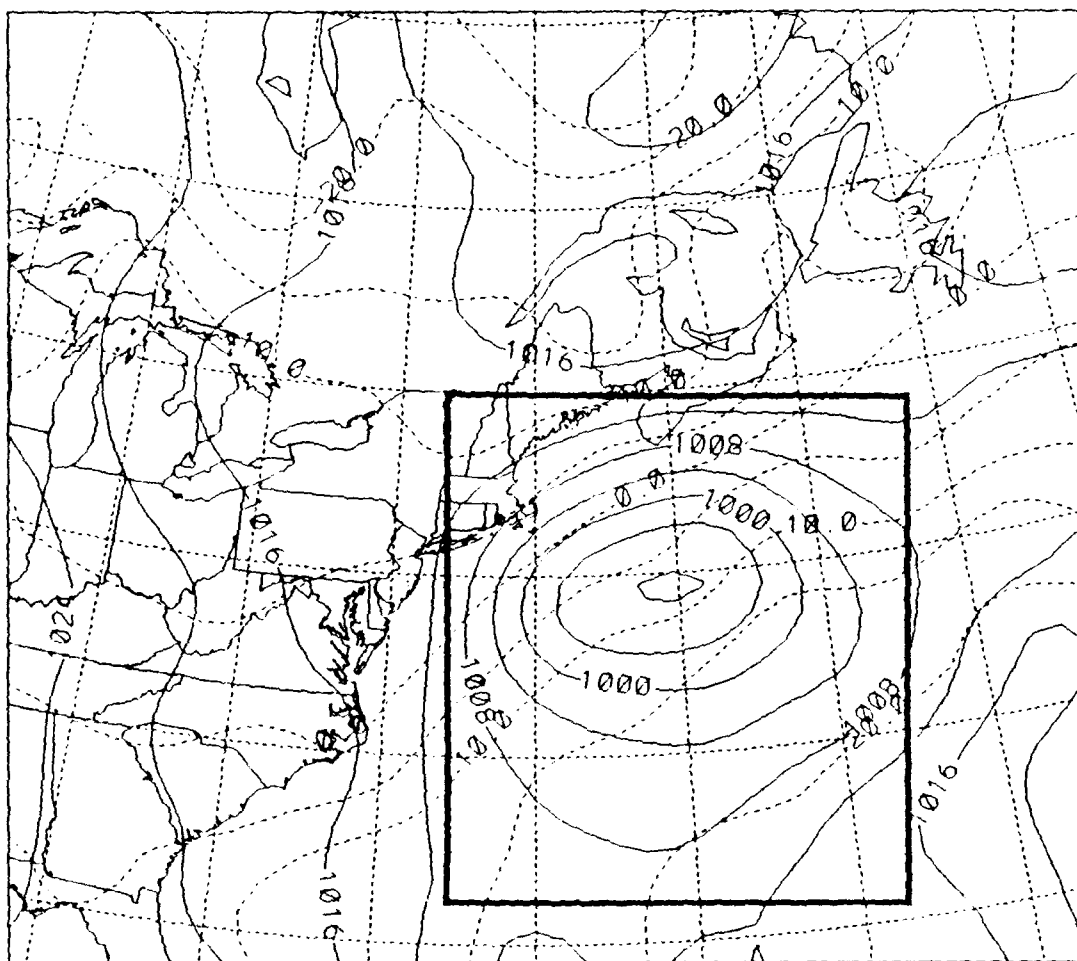


Fig. 9. Objective analysis of pressure (mb) and temperature (°C) for 0000 UTC 18 December 1988. Contour intervals as in Fig. 7. Bold lines indicate bounds of "cyclone domain".

The first method to objectively verify the vertical motion fields compared the divergence field of Q to the vertical velocity measured by research aircraft during the IOP 3 and IOP 5 cyclones. A moving 20 minute average of the vertical velocity measurements within 90 minutes of a synoptic time were compared to a linearly interpolated value of $-2\nabla \cdot Q$ for the same point in space. Separate correlations were made for all observations of vertical motion and only the vertical motion observations

below 1500 m. Although the units of the vertical velocity measurements and the forcing terms of (1) are not the same, a positive correlation was expected.

The second objective evaluation of the \mathbf{Q} vector divergence field was with isallobaric fields calculated from the gridded pressure fields 3 h and 6 h in the future. For each objective analysis, the area affected by the cyclone circulation was subjectively determined. This area was then defined by the lower-left and upper-right grid points, and a rectangle connecting these grid points was constructed (see Fig. 9). All subsequent calculations involving \mathbf{Q} vectors and pressure tendencies were confined to this "cyclone-relative" domain. This method ensured that the only areas of significant \mathbf{Q} vector convergence or divergence studied are those regions relevant to the storm.

In the short term (0-6 h), the surface low center can be expected to track toward the maximum pressure falls, which are hypothesized to be under the regions of strongest uplift in the mid-troposphere, represented here by the $-2\nabla \cdot \mathbf{Q}$ values. Both qualitative and quantitative comparisons were made to evaluate the method. Scatter plots of future pressure tendency (3 h and 6 h) vs. $-2\nabla \cdot \mathbf{Q}$ were constructed for both the IOP 3 and IOP 5 cyclones. Linear regression equations and correlation coefficients were also calculated and displayed. In addition, the mean pressure change at each point where $|\nabla \cdot \mathbf{Q}| \geq 10 \times 10^{-16} \text{ m kg}^{-1} \text{ s}^{-1}$ was calculated every 3 h and 6 h, provided at least 10 grid points in the field met this criterion. A 95% confidence interval was then calculated. The mean pressure change and the confidence intervals were plotted for pressure tendencies both 3 h and 6 h into the future.

The statistical method described above uses adjacent points that are not independent to calculate the confidence intervals. Due to the low number of data points that met the $|10| \times 10^{-16} \text{ m kg}^{-1} \text{ s}^{-1}$ criterion at any time, these points were composited for each IOP for 3 h and 6 h pressure changes. About 20% of the points were sampled at random, and the 95% confidence intervals for Δp for 3 h and 6 h were calculated. For each time and each IOP, the change in surface pressure was statistically different (to a 95% confidence level) between areas whose $-2\nabla \cdot \mathbf{Q} \geq 10 \times 10^{-16} \text{ m kg}^{-1} \text{ s}^{-1}$ and regions where $-2\nabla \cdot \mathbf{Q} \leq -10 \times 10^{-16} \text{ m kg}^{-1} \text{ s}^{-1}$. This statistically significant difference, along with the regions of \mathbf{Q} vector convergence (divergence) occurring ahead of (behind) the storm track as physically expected, lends credence to the objective results.

IV. CASE STUDIES

A. IOP 3

1. Synoptic Overview

The rate of intensification of the IOP 3 storm is typical for a rapidly deepening cyclone (Fig. 6). The maximum deepening rate from the hand analyses was $\sim 7 \text{ mb (6h)}^{-1}$ between 1200 UTC 17 December and 1200 UTC 18 December 1988. However, the track of the IOP 3 storm (Fig. 10) is unusual for a cyclogenesis event along the North American seaboard. This storm had three significant, discrete centers at the surface during its existence. The main surface low formed about 300 km east of Cape Hatteras (HAT) at 1200 UTC 17 December, moved northeastward at about 50 km h^{-1} until 0600 UTC 18 December, then headed north-northeast at 80 km h^{-1} and reached southeast Labrador by 1800 UTC 18 December. The initial pressure of the surface wave east of HAT was 1007 mb. By 18 UTC 18 December, the storm reached its minimum pressure of about 975 mb as it passed over the eastern Gulf of St. Lawrence. Thus, the net intensification was 32 mb over 30 h.

As shown by the 0000 UTC 17 December 500 mb height and absolute vorticity analysis in Fig. 11, three vorticity maxima contributed to the formation and intensification of the IOP 3 cyclone. Initially, two vorticity maxima located near the North Carolina coast were responsible for the multiple surface circulations that were observed during the early period of development. The much stronger vorticity maximum in Fig. 11 was

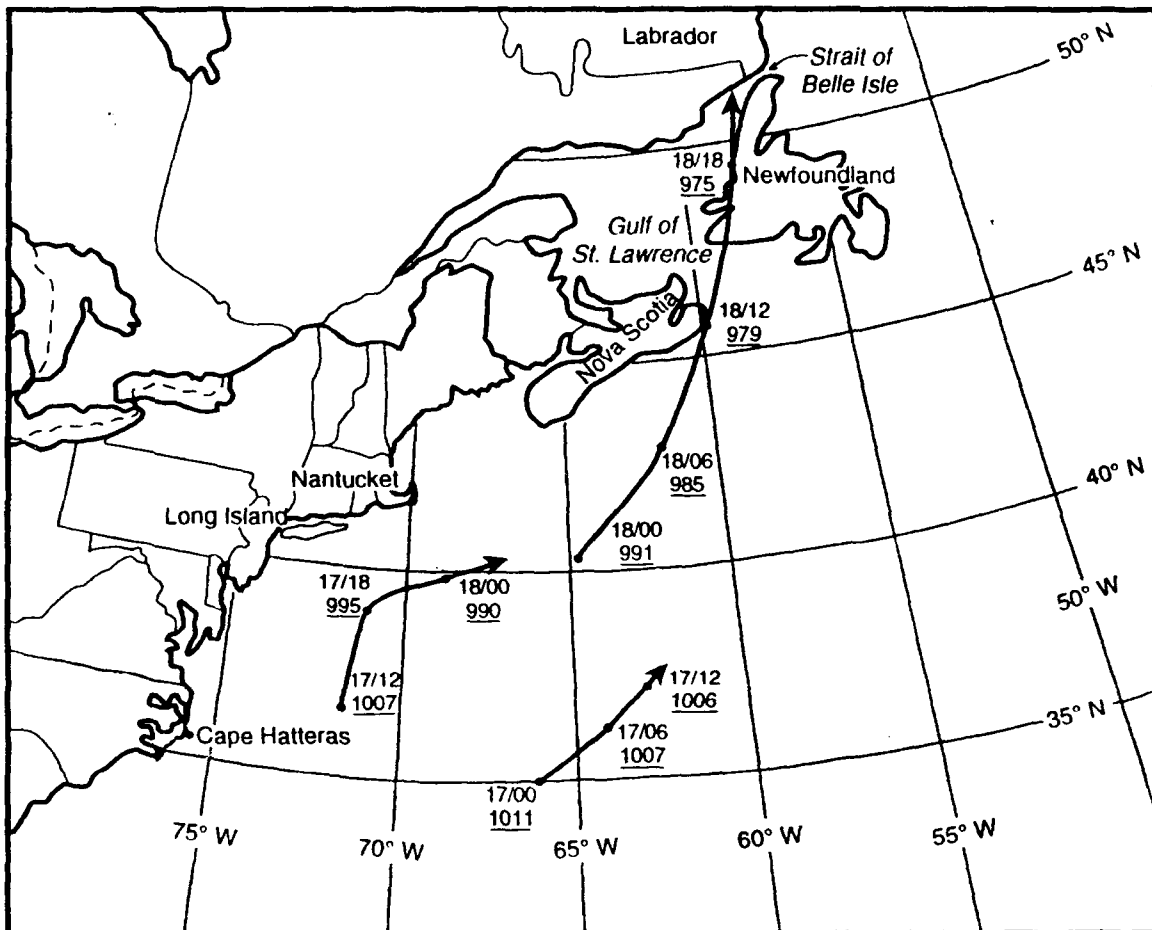


Fig. 10. Tracks (solid) of IOP 3 storms as analyzed by Sanders (1989). Underlined number is pressure (mb). Time is (day/hour) UTC December 1988.

associated with a vigorous short-wave disturbance over northern Illinois. This vorticity maximum subsequently propagated southeast towards the mid-Atlantic coast to support the rapid development phase of the IOP 3 cyclone.

The 1200 UTC 17 December surface analysis (Fig. 12), based on numerous ship and ERICA drifting buoy reports, reveals three separate lows, although the low 400 km southeast of HAT is weak and does not appear on other past or future surface analyses. Consequently, this low was not included in Fig. 10. The eastern low is 1000

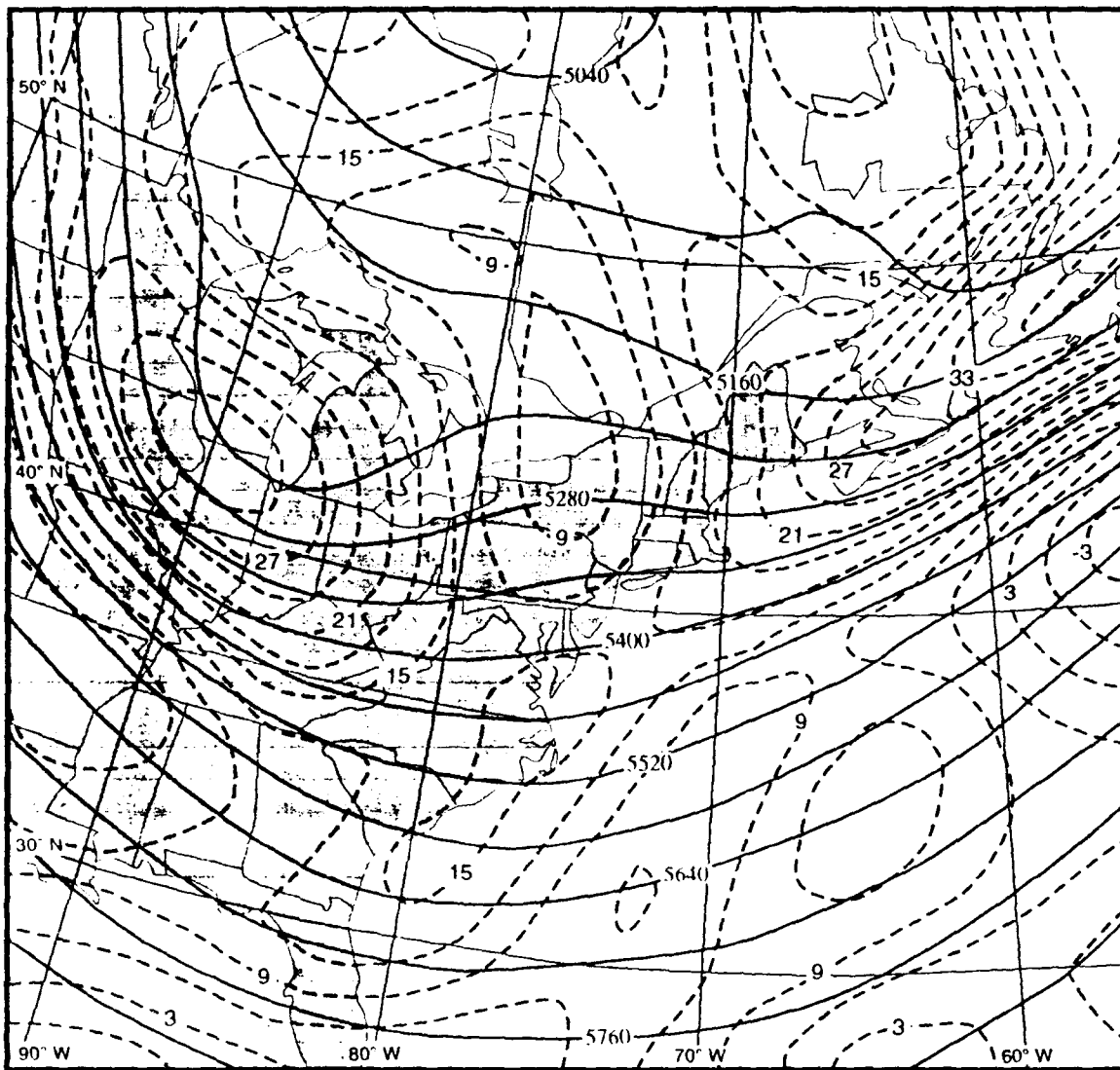


Fig. 11. 500 mb height (solid, contour interval 60 dam) and absolute vorticity (dashed, contour interval $3 \times 10^{-5} \text{ s}^{-1}$) analysis at 0000 UTC 17 December 1988.

km east-northeast of HAT and is propagating towards the east-northeast as a stable wave. Notice the similarity between the thickness field (Fig. 13) and the surface temperature field (Fig. 12) over the ocean. This similarity supports the hypothesis that the surface Q vectors may be representative of the entire lower troposphere, rather than just the boundary layer.

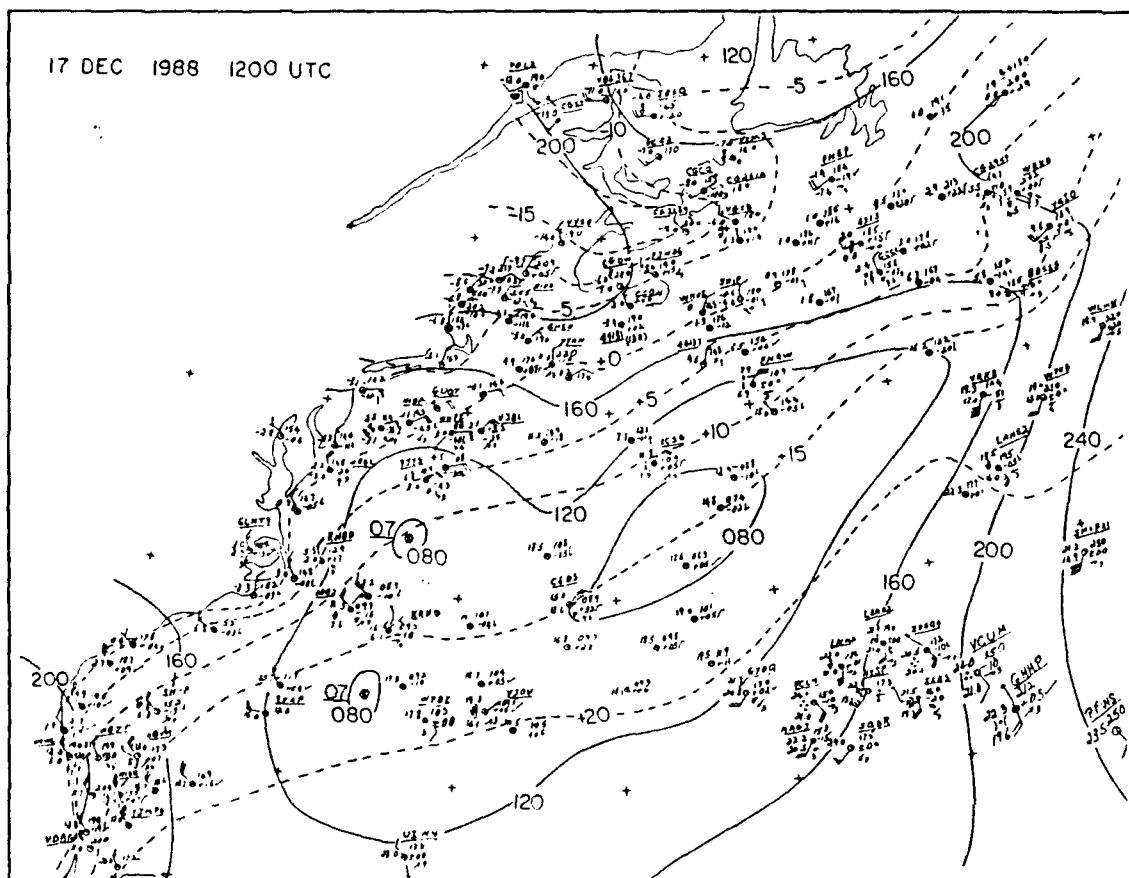


Fig. 12. Surface pressure (solid, contour interval 4 mb) and temperature (dashed, contour interval 5°C) analysis at 1200 UTC 17 December 1988.

The intensifying 500 mb short-wave trough previously over Illinois is over the Appalachian Mountains at 1200 UTC 17 December, and is moving into the long-wave trough along the eastern seaboard (Fig. 14). A vorticity maximum exceeding $30 \times 10^{-5} \text{ s}^{-1}$ is associated with the trough over eastern Kentucky, and an area of strong CVA over the Virginia and Delmarva coast and adjacent waters is positioned above the surface low east-northeast of HAT. A 70 m s^{-1} jet streak is associated with this trough at 300 mb (Fig. 15). The leading edge of this jet streak is over the North Carolina coast, which

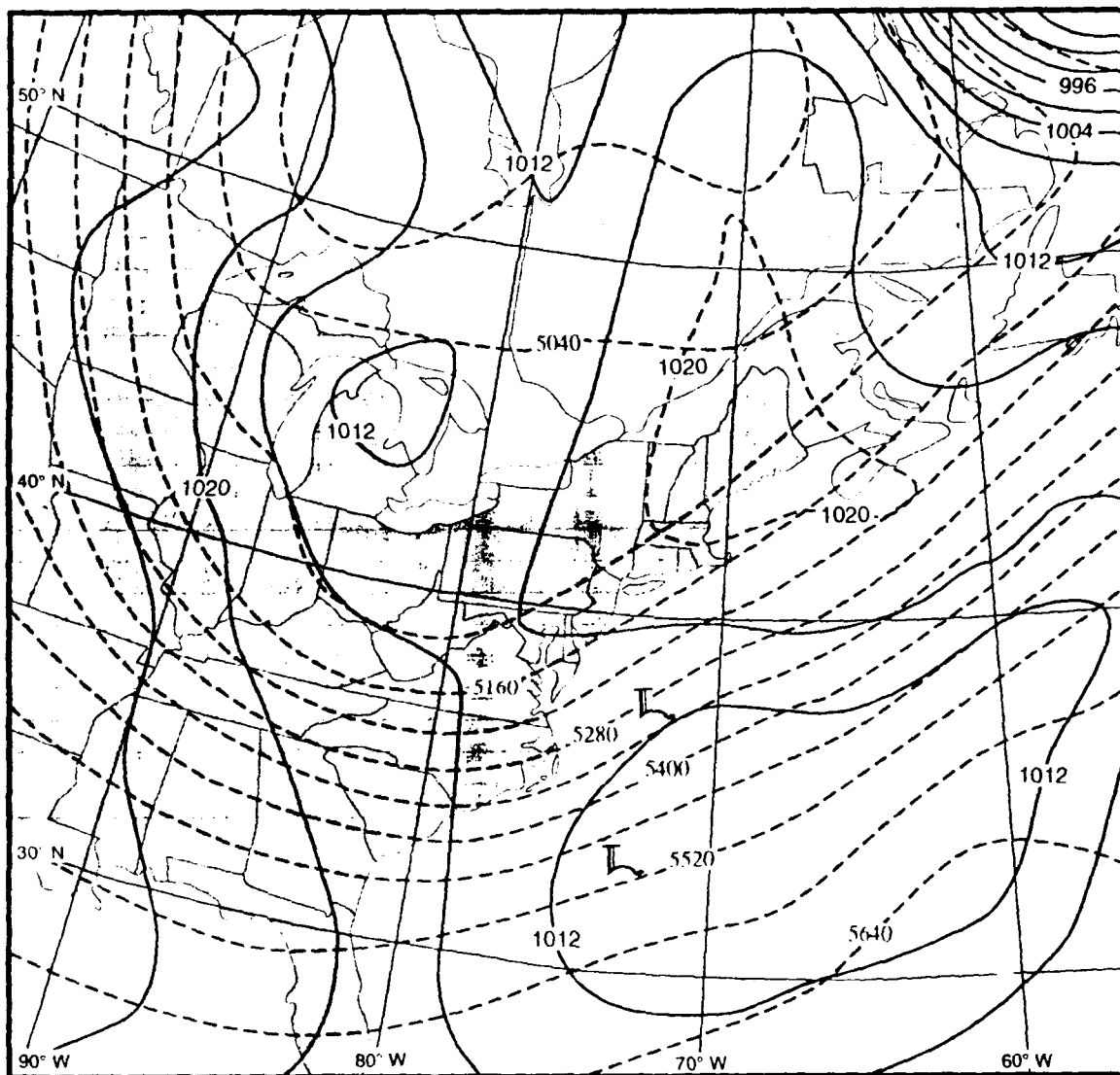


Fig. 13. Surface pressure (solid, contour interval 4 mb) and 1000-500 mb thickness (dashed, contour interval 60 dam) analysis at 1200 UTC 17 December 1988. "L" marks position of surface lows as shown in Fig. 12.

places the low east-northeast of HAT under the left-front quadrant and provides upper-level divergence above the surface low.

Significant deepening of the surface low is occurring by 1800 UTC 17 December (Fig. 16). Aircraft and ship observations indicate the main low is about 400

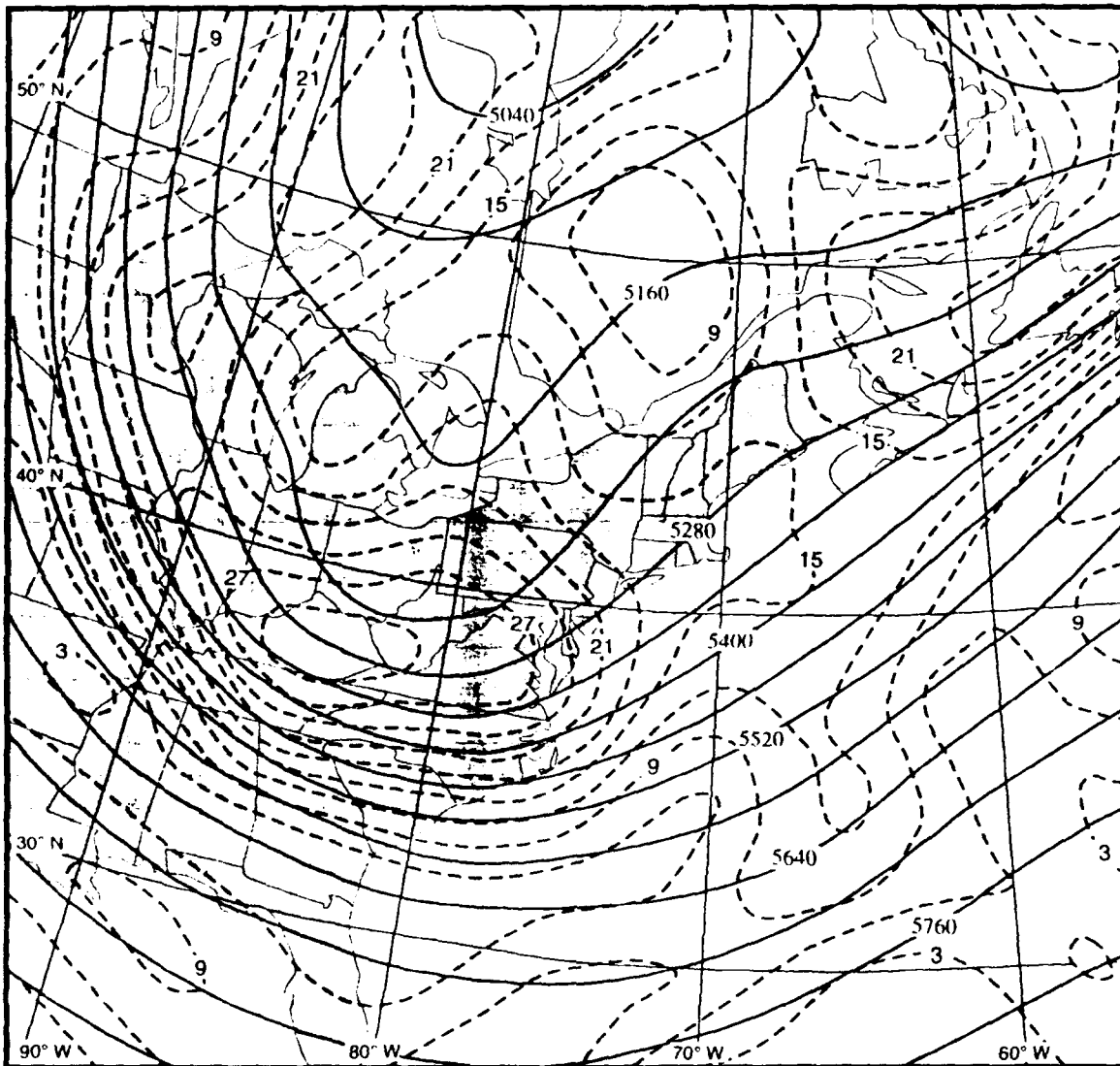


Fig. 14. 500 mb height and absolute vorticity analysis as in Fig. 11, except for 1200 UTC 17 December 1988.

km southeast of New York City. The position of the low is just south of the north wall of the Gulf Stream (Fig. 17). Temperatures immediately south of the Gulf Stream are 21-23°C, and are 10-12°C just 100 km north of the Gulf Stream. Significant surface baroclinicity is associated with the warm front, with surface temperatures between 15-17°C in the warm sector and only 1-3°C about 200 km north of the surface warm front

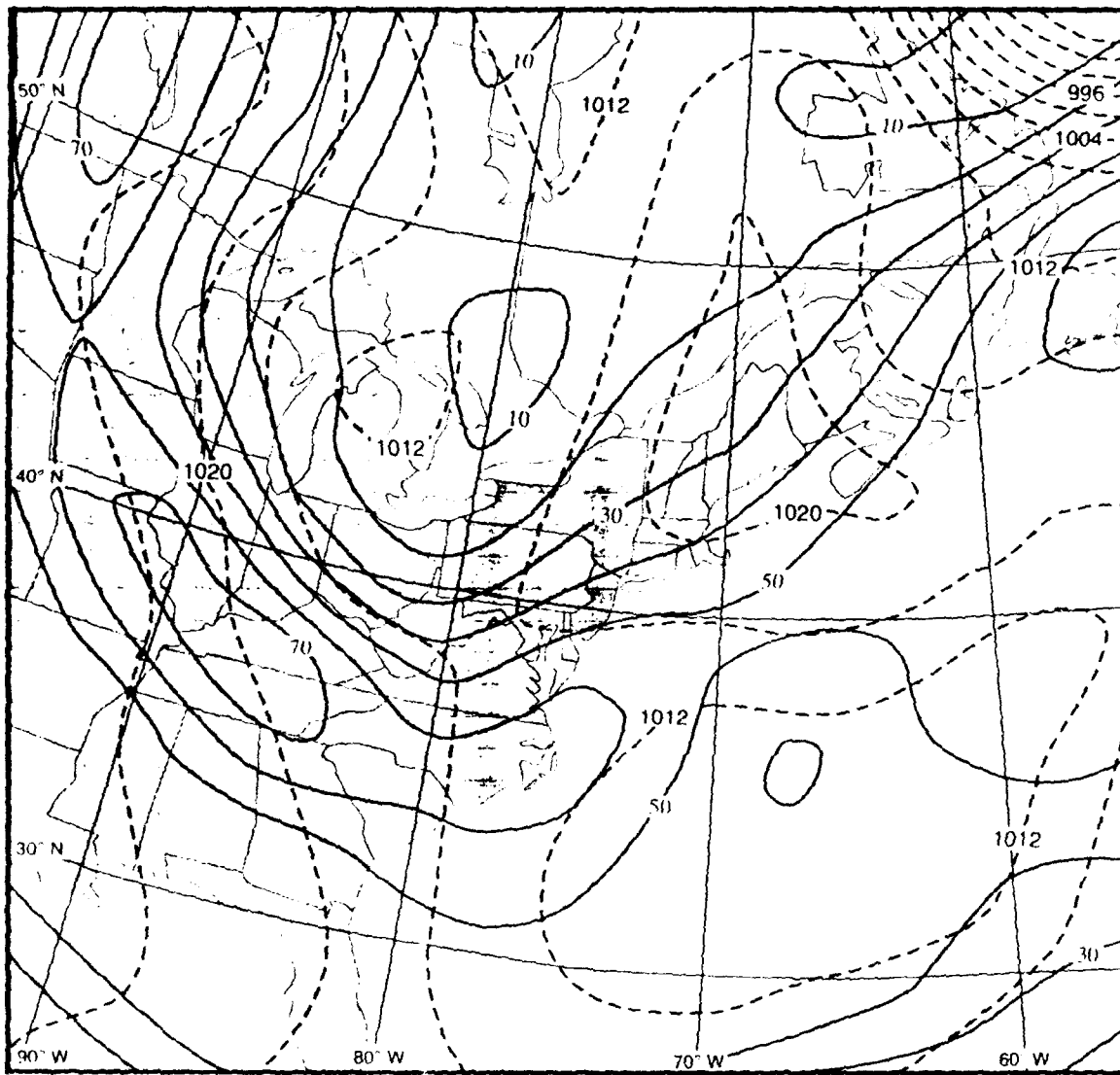


Fig. 15. 300 mb isotach (solid, contour interval 10 m s^{-1}) and surface pressure (dashed, contour interval 4 mb) analysis at 1200 UTC 17 December 1988.

(Fig. 16). This baroclinity is favorable for producing geostrophic warm advection and upward motion to the east of the low. Ships "YJWD", "CGBW" and buoy "WHOI" observations south of Nova Scotia show strong ageostrophic flow in the cold air. This ageostrophic flow is parallel to the surface temperature gradient, a situation similar to that described by Nuss and Kamikawa (1990) for a rapidly developing cyclone east of Japan.

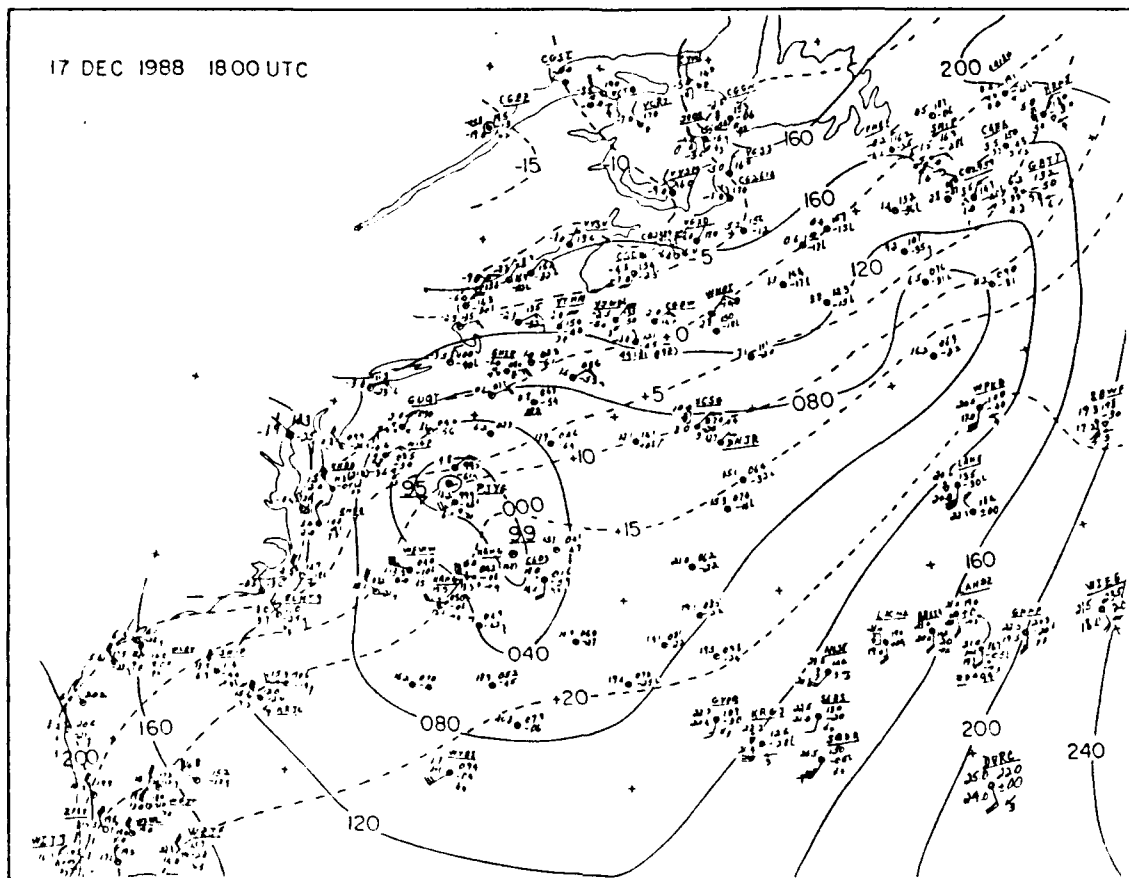


Fig. 16. Surface pressure and temperature analysis as in Fig. 7, except for 1800 UTC 17 December 1988.

In the Nuss and Kamikawa case, the ageostrophic flow was occurring in a region where the boundary layer was well mixed to 850 mb. Although this study has not explicitly calculated the vertical stability north of the warm front, it is not unreasonable to expect a well-mixed boundary layer as air over eastern Quebec and Newfoundland with surface temperatures well below 0°C is being advected over slope water with temperatures between 3-8°C. As discussed by Nuss and Kamikawa, strong ageostrophic flow in a well-mixed boundary layer would suggest that surface frontogenesis is being enhanced by a strong direct thermal circulation.

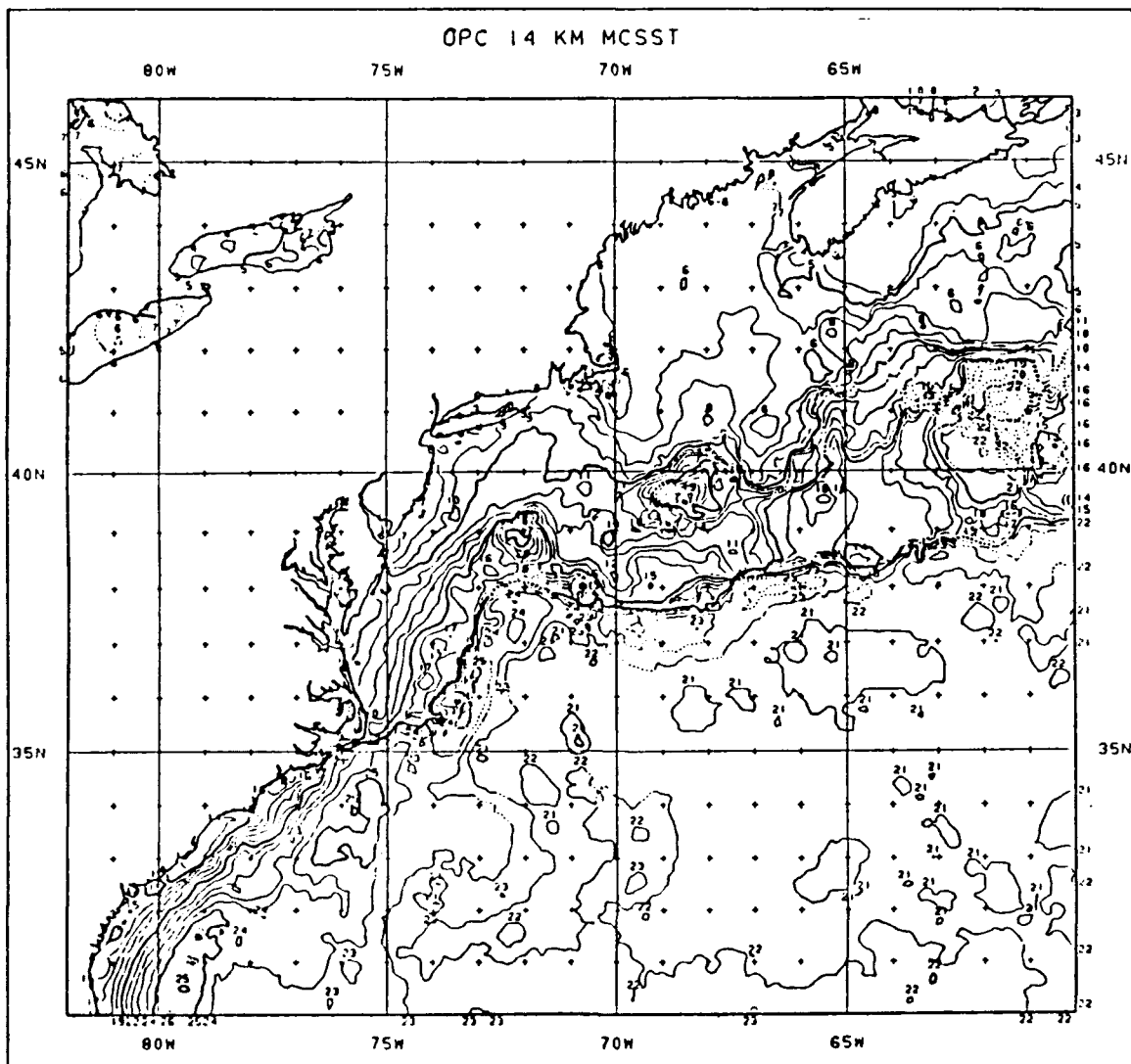


Fig. 17. Sea-surface temperatures (°C) during IOP 3 (Hadlock and Kreitzberg 1988).

At 0000 UTC 18 December (Fig. 7), very good ship, buoy and aircraft reports confirm two distinct surface low centers. The western low has a central pressure of 991 mb and is located 200 km southeast of Nantucket (ACK) over the cold slope water. Another center is forming 250 km east-northeast of the main low. The 500 mb height analysis (not shown) has a strong ($30 \times 10^{-5} \text{ s}^{-1}$) vorticity maximum 300 km south of ACK,

with strong CVA over the new low. The older low is southwest of the strongest CVA. The 300 mb isotach analysis (Fig. 18) has a jet streak with winds in excess of 60 m s^{-1} about 250 km east-northeast of HAT. The left-front quadrant of this jet streak supports the eastern low, which becomes the dominant surface low. The 300 mb analysis does not show an "outflow" jet as described by Kocin and Uccellini (1990) developing above a region of ascent north of the warm front. This may inhibit the strength of the direct secondary circulation associated with the warm front, and explain why there are not as many surface reports of strong ageostrophic winds as there were at 1800 UTC 17 December. The apparent lack of a sustained, vigorous direct circulation in the vicinity of the warm front may be one reason why this storm did not intensify at a more rapid rate.

At 1200 UTC 18 December (Fig. 19), the dual centers have consolidated into one low pressure system. The storm is approaching maximum intensity, with aircraft and land reports supporting a 980 mb analyzed central pressure. Winds over the ocean within 600 km of the storm are mostly $15\text{--}20 \text{ m s}^{-1}$, with one ship 300 km south of the low ("GBTT") reporting a wind speed of 25 m s^{-1} . The storm is now well north of the Gulf Stream, and is occluding. The 500 mb shortwave and vorticity maximum are almost centered above the surface low, which causes the CVA to be northeast of the surface low over the Gulf of St. Lawrence and Newfoundland (Fig. 20). This inhibits substantial further deepening of the surface low. Likewise, the 300 mb analysis (not shown) has a broad 60 m s^{-1} jet streak extending from Newfoundland southwest to 32°N , 73°W . Because this jet streak is embedded in a mean flow in excess of 40 m s^{-1} , only weak

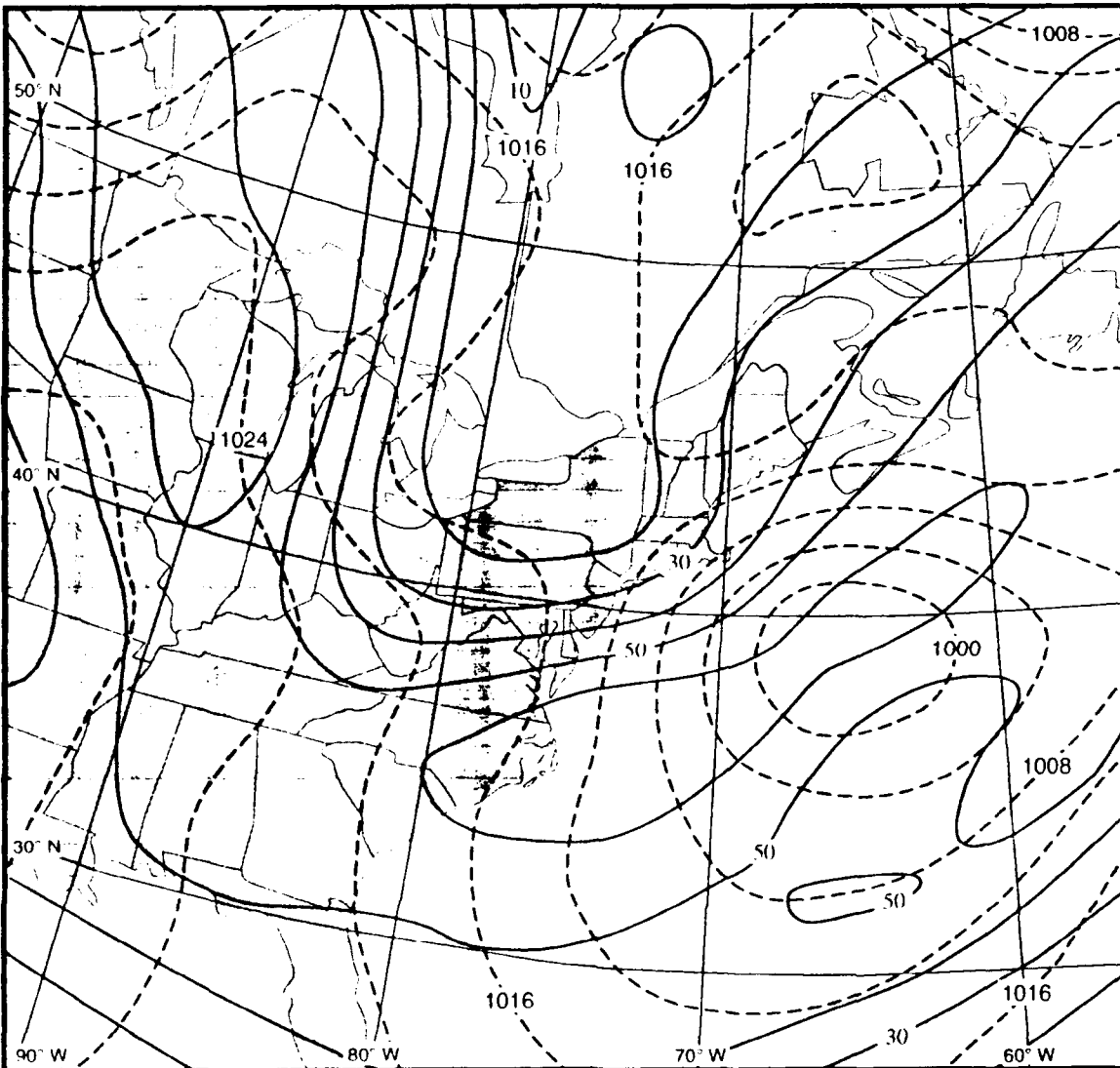


Fig. 18. 300 mb isotach and surface pressure analysis as in Fig. 15, except for 0000 UTC 18 December 1988.

divergence is probably occurring aloft. The strongest divergence aloft is probably in the left-front quadrant over Newfoundland, which is northeast of the surface low.

At 1800 UTC 18 December, the surface low (not shown) has moved into the Gulf of St. Lawrence, with an analyzed central pressure of 975 mb. Much of the circulation of the surface storm is now over land. Consequently, analyses beyond 1800

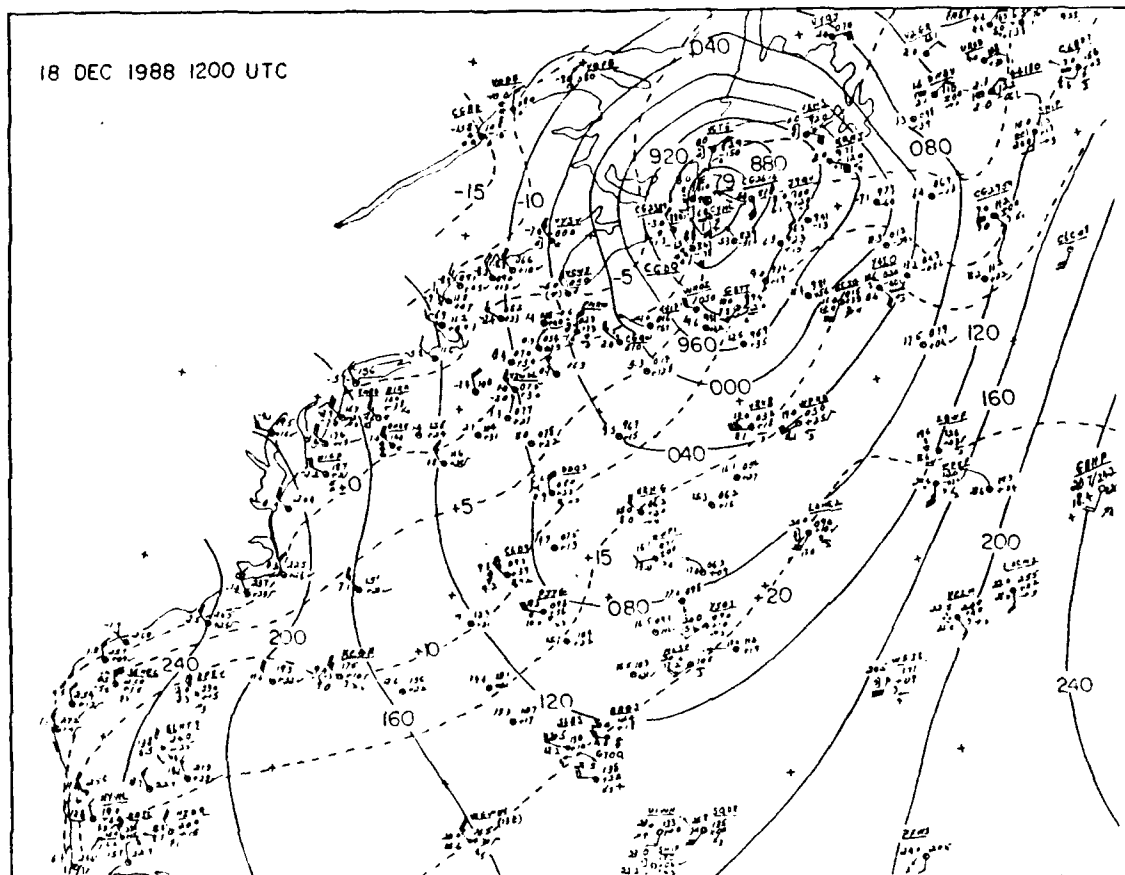


Fig. 19. Surface pressure and temperature analysis as in Fig. 7, except for 1200 UTC 18 December 1988.

UTC 18 December will not be included in this study, although the IOP lasted until 0000 UTC 19 December.

2. Q Vectors and Satellite Imagery

While the storm is initially developing (0000-0600 UTC 17 December 1988), the magnitude of $-2\nabla \cdot \mathbf{Q}$ is relatively small (less than $10 \times 10^{-16} \text{ m kg}^{-1} \text{ s}^{-1}$), and the \mathbf{Q} vectors have the greatest ageostrophic circulation near the axis of the inverted trough along 60°W (not shown). At 0600 UTC 17 December (Fig. 21), the \mathbf{Q} vectors have two areas of convergence: one area associated with the warm advection in the apex of the

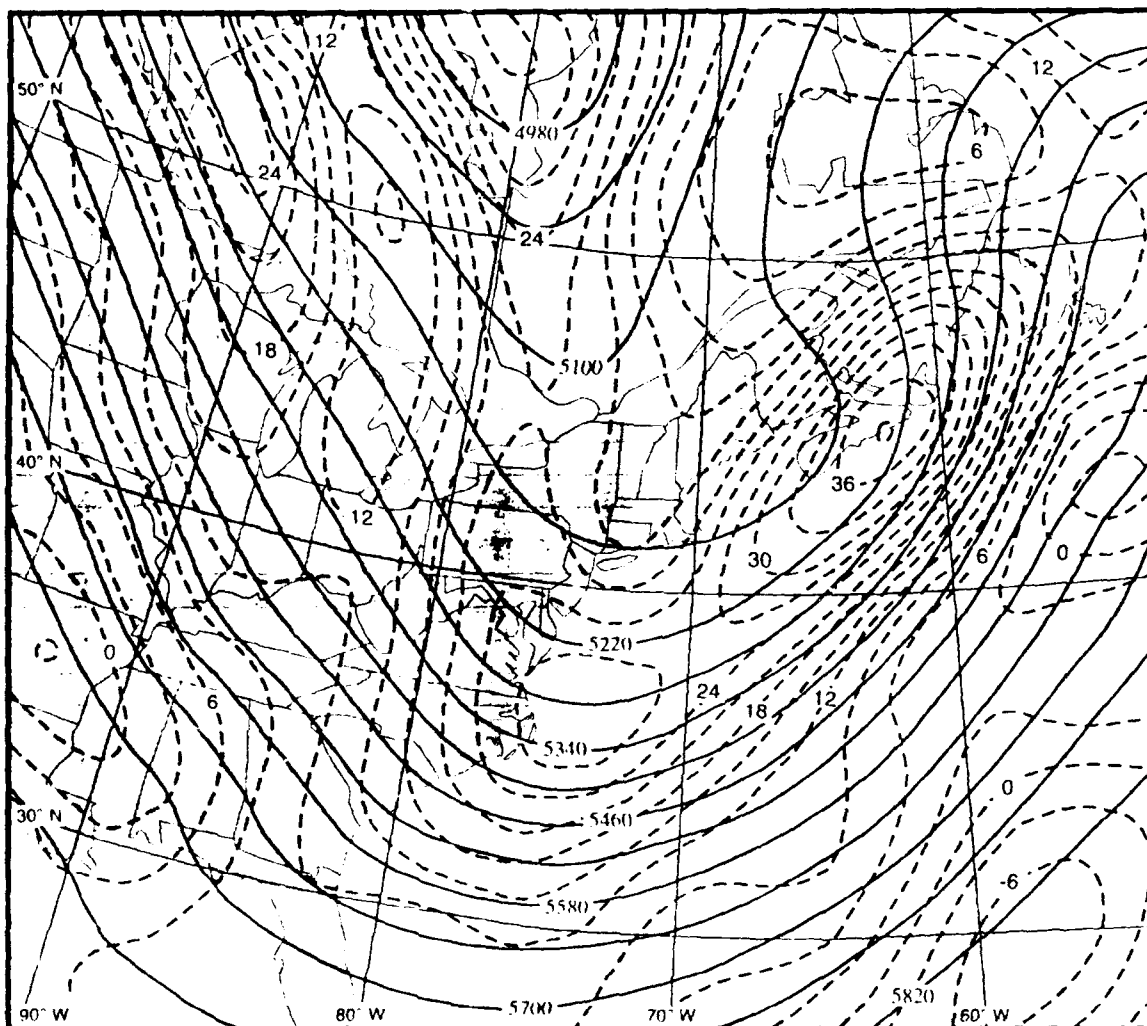


Fig. 20. 500 mb height and absolute vorticity analysis as in Fig. 11, except for 1200 UTC 18 December 1988.

inverted trough, and a second area extending from Long Island southwest to 33°N, 65°W that has maximum convergence about 600 km east-northeast of HAT. The cause of this second area of convergence is slight warm advection in confluent geostrophic flow occurring at the surface. This Q vector convergence east of HAT is about 100 km east of, and precedes by 6 h, the formation of the first significant low in IOP 3. The 0601 UTC 17 December IR GOES imagery (Fig. 22) confirms the significance of the forcing

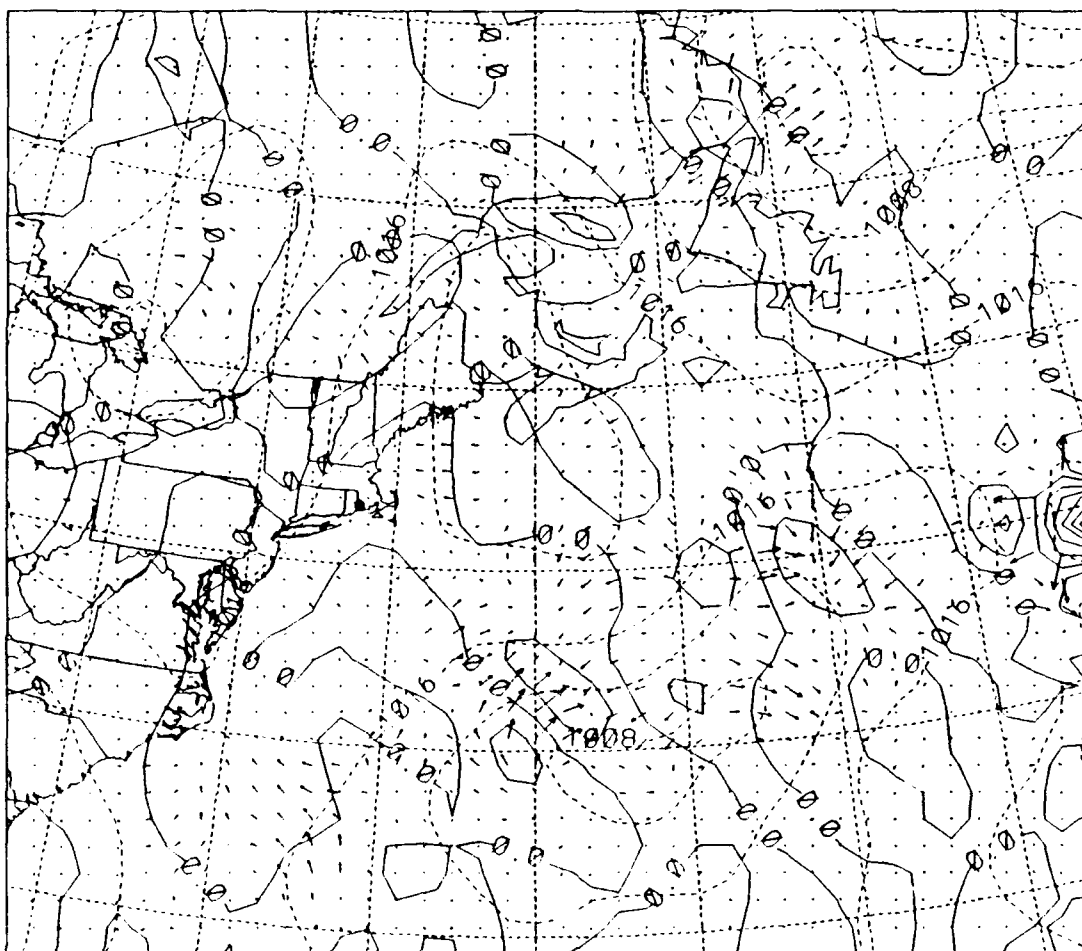


Fig. 21. $-2\nabla\cdot\mathbf{Q}$ (solid, contour interval $10\times 10^{-16} \text{ m kg}^{-1} \text{ s}^{-1}$), surface isobars (dashed, contour interval 4 mb) and \mathbf{Q} vectors (arrows) at 0600 UTC 17 December 1988.

in this region and indicates low to mid-level clouds in this area of convergence. Although it is not apparent from the satellite image alone that cyclogenesis will be occurring east of HAT in about 6 h, the \mathbf{Q} vectors suggest organized forcing of low-level vertical motion.

The \mathbf{Q} vector convergence for 0900 UTC 17 December (not shown) also has two areas of significant convergence. The first area is near $40^\circ\text{N } 61^\circ\text{W}$, and is associated with the eastern low as it progresses eastward. The second area is centered about 600 km

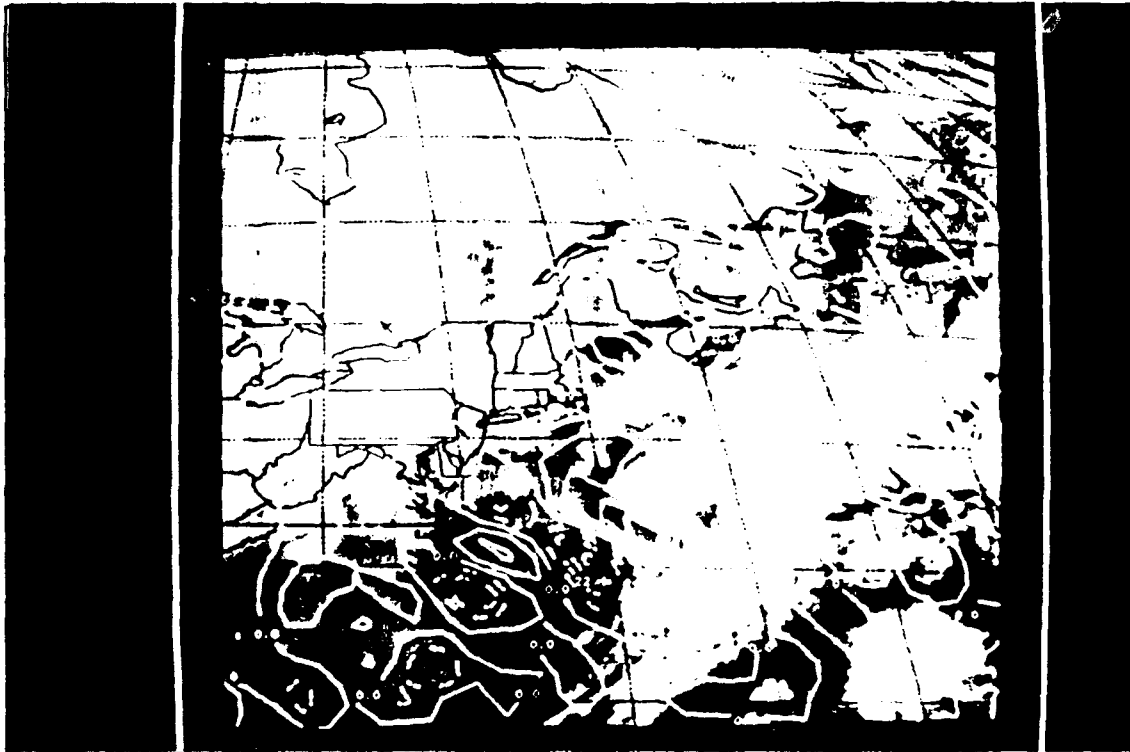


Fig. 22. GOES IR imagery, and $-2\nabla \cdot \mathbf{Q}$ (contour interval $10 \times 10^{-16} \text{ m kg}^{-1} \text{ s}^{-1}$, solid lines where $-2\nabla \cdot \mathbf{Q} > 0$) at 0601 UTC 17 December 1988.

east-northeast of HAT, and has a magnitude greater than $20 \times 10^{-16} \text{ m kg}^{-1} \text{ s}^{-1}$. This significant area of \mathbf{Q} vector convergence is caused by strong warm advection resulting from the southeasterly flow around the deepening wave. The 0901 UTC 17 December satellite imagery (not shown) still has only low clouds in the vicinity of the strongest surface forcing.

While the significant surface forcing was being depicted at 0600 UTC 17 December and 0900 UTC 17 December, there has been poor correlation between $-2\nabla \cdot \mathbf{Q}$ and any significant mid- or upper-level stratiform or convective clouds. As the surface low started to develop, the low-level forcing appeared to be ahead (to the east) of the

upper-level dynamics that will support significant deepening. Even though little (3 mb (6h)^{-1}) deepening was occurring during this time, the \mathbf{Q} vectors provided a very good indication of where the surface low eventually formed.

By 1200 UTC 17 December, the first major low of IOP 3 had formed east-northeast of HAT, where the strongest (over $20 \times 10^{-16} \text{ m kg}^{-1} \text{ s}^{-1}$) upward motion had been indicated for the past 6 h. As shown in Fig. 23, the area of maximum \mathbf{Q} vector convergence has shifted northeast to 39°N , 68°W , which was where the strongest warm advection was occurring between the high over Maine and the low east of HAT. At 1201 UTC 17 December (not shown), the GOES IR picture had convection in the vicinity of the strong \mathbf{Q} vector convergence, which implied that forcing near the surface and aloft (as depicted by the NMC 500 mb (Fig. 14) and 300 mb (Fig. 15) final analyses) was coming into phase. It is interesting to note that when the surface forcing, and the stratiform and convective clouds coincided for the first time, the surface low began a rapid deepening phase.

The storm was rapidly deepening by 1800 UTC 17 December, and the areas of strongest upward motion as inferred from the surface \mathbf{Q} vector divergence agreed well with the location of the cold-topped stratiform clouds and embedded convection as depicted by satellite imagery for the next 12 h. Between 1800 UTC 17 December (Fig. 24 and Fig. 25) and 0300 UTC 18 December, the strongest areas of \mathbf{Q} vector convergence are located in the future path of the storm, i.e., to the north and east of the storm center. This pattern of implied upward and downward vertical motion agrees well with established conceptual models of extratropical cyclones (e.g., Petterssen 1956).

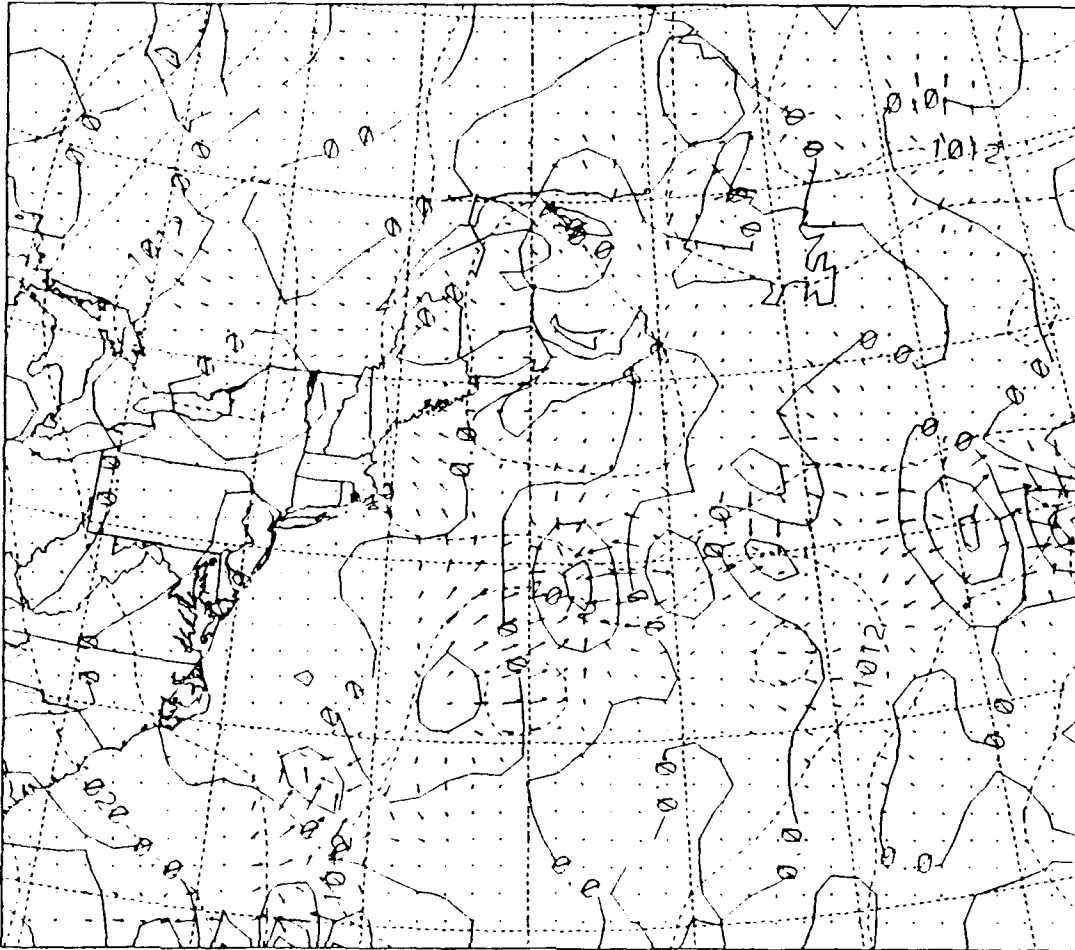


Fig. 23. $-2\nabla \cdot \mathbf{Q}$, surface isobars and \mathbf{Q} vectors as in Fig. 21, except for 1200 UTC 17 December 1988.

Fig. 25 has the maximum \mathbf{Q} vector convergence at the southern and western edge of the deep cloud field, rather than in the center of the deepest clouds. Part of this lag can be attributed to the visible satellite photograph time of 1901 UTC 17 December, while the \mathbf{Q} vectors were calculated using data from 1800 UTC 17 December. The area of maximum \mathbf{Q} vector convergence is closely correlated with the strongest warm advection at the surface, and lies just north of the surface warm front. While the low is still deepening, the storm is in its optimum phase for continued development. The correlation

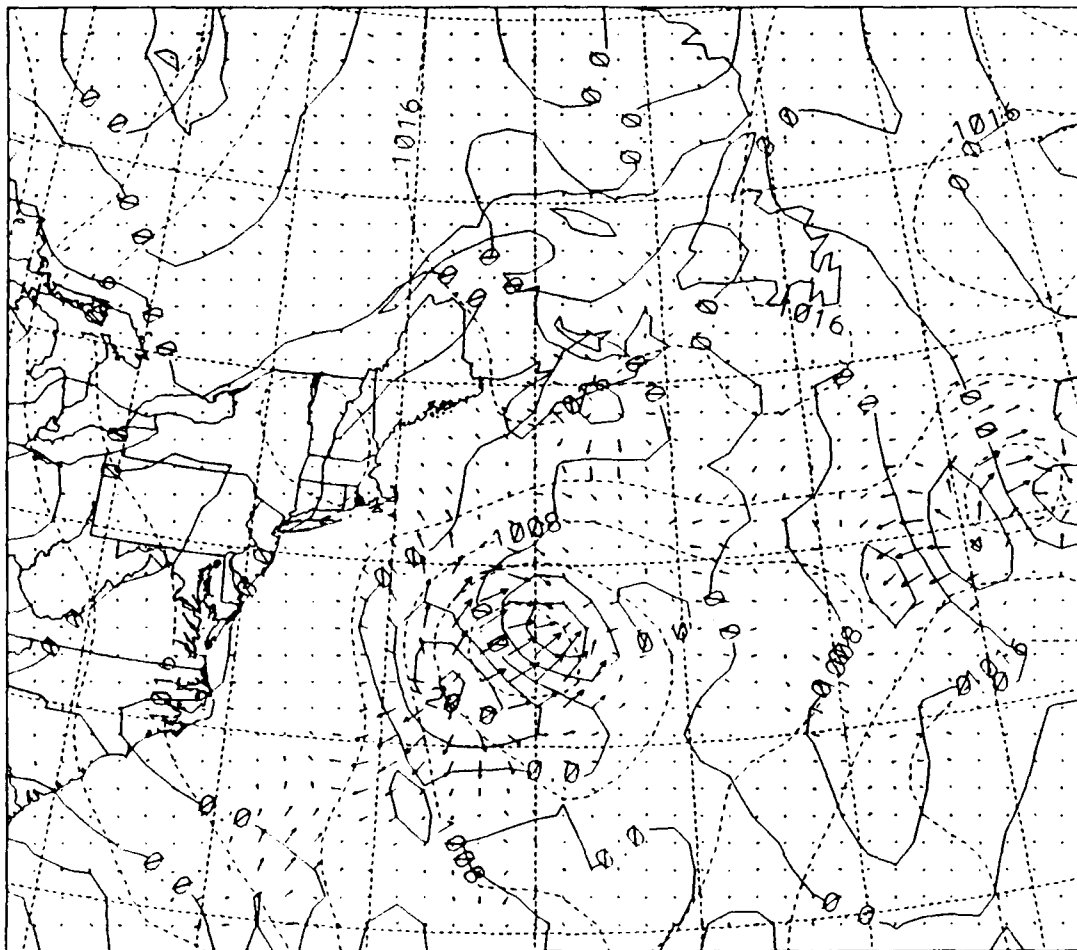


Fig. 24. $-2\nabla\cdot Q$, surface isobars and Q vectors as in Fig. 21, except for 1800 UTC 17 December 1988.

between the surface forcing and the cold-topped stratiform clouds may indicate that both surface and upper-level forcing are in phase, and the storm is deepening with maximum efficiency. This relationship is best shown in Fig. 26 and Fig. 27, which depict the Q vector forcing and satellite imagery respectively for 0300 UTC 18 December. Future studies are suggested to examine vertical cross-sections of the low during this part of its life cycle to verify that the lower- and upper-level forcing is in phase and that the Q vectors are accurately depicting the vertical motions.

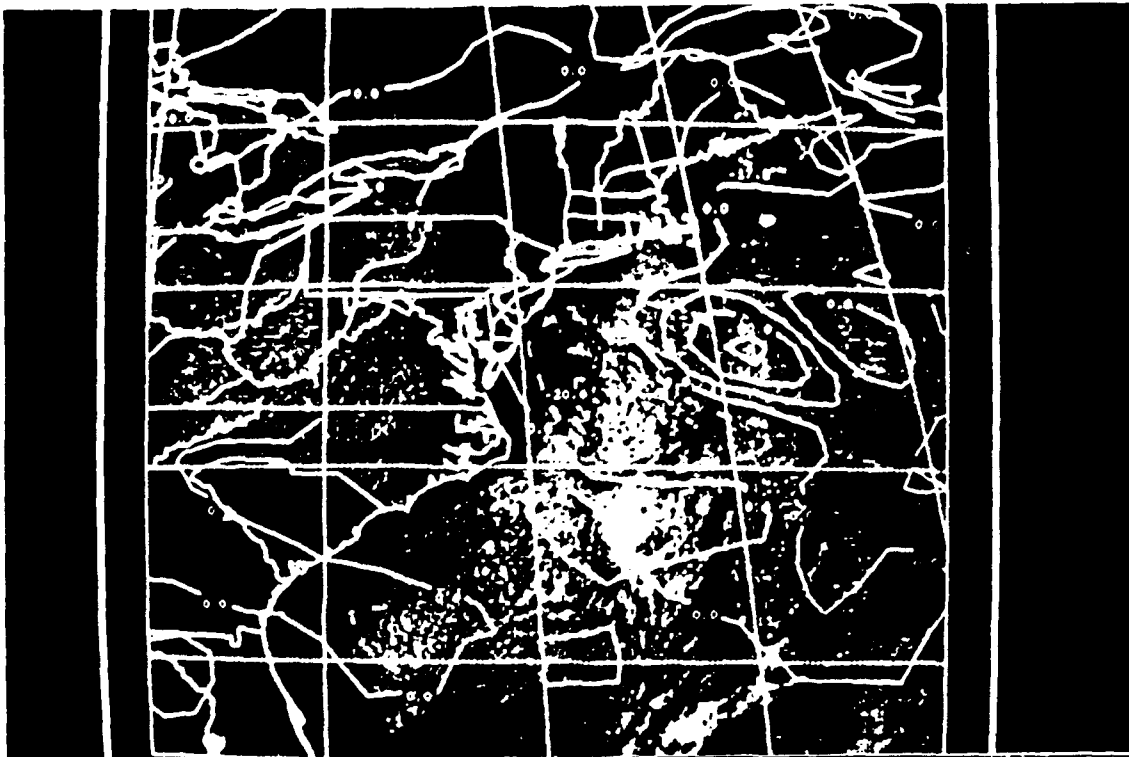


Fig. 25. GOES Visible imagery and $-2\nabla\cdot\mathbf{Q}$ (contour interval $10\times 10^{-16} \text{ m kg}^{-1} \text{ s}^{-1}$, solid lines where $-2\nabla\cdot\mathbf{Q} > 0$) at 1901 UTC 17 December 1988.

Beginning at 0600 UTC 18 December (Fig. 28), and becoming more pronounced by 1200 UTC 18 December (not shown), the extensive stratiform clouds and precipitation (as determined by GOES IR imagery) has outrun (moved farther to the north) the maximum forcing at the surface as shown by \mathbf{Q} vectors. Only low clouds exist in the Gulf of St. Lawrence, where a maximum in \mathbf{Q} vector convergence is found. However, the surface \mathbf{Q} vectors in Fig. 28 accurately depict the triple point of the storm, and its associated deep convection. Although the cyclone was still deepening through this time period, the upper-level support for the storm, as evidenced by the location of the maximum CVA at 500 mb (Fig. 20) and the position of the 300 mb jet streak (not shown)

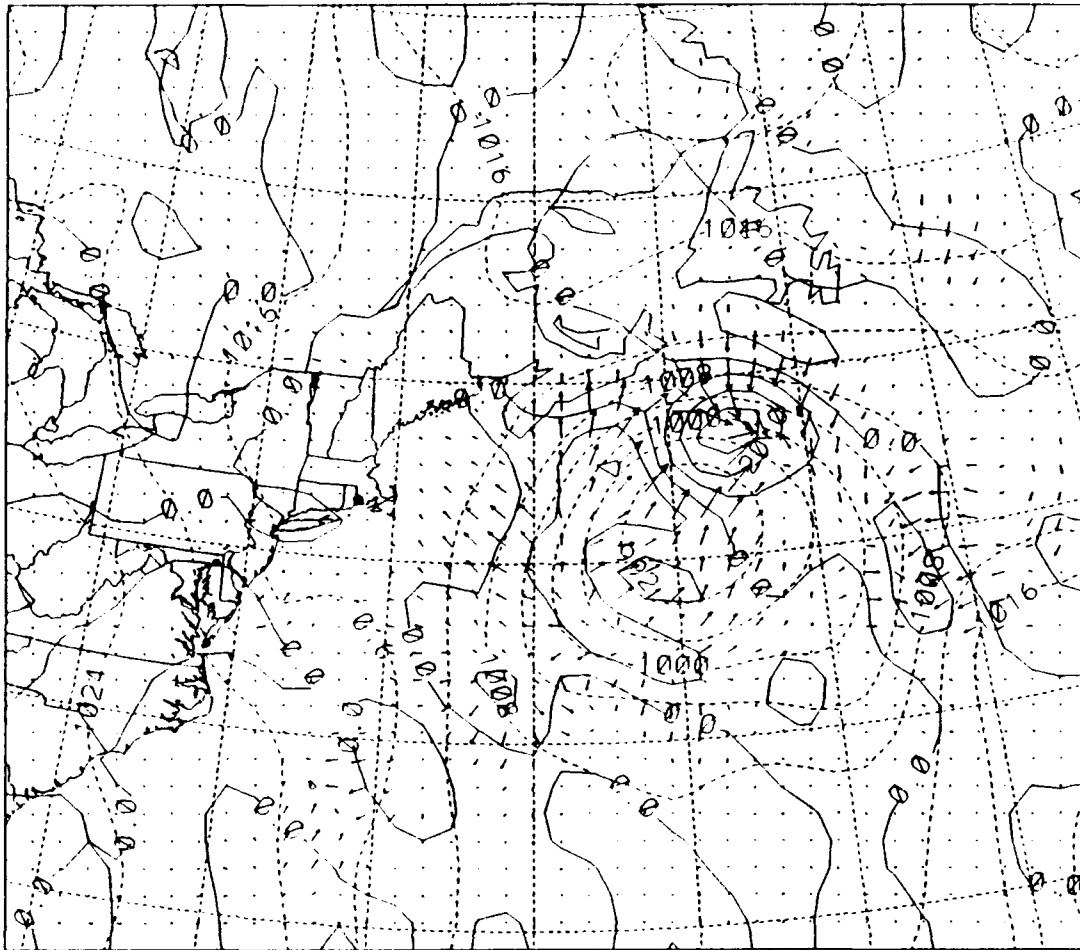


Fig. 26. $-2\nabla \cdot \mathbf{Q}$, surface isobars and \mathbf{Q} vectors as in Fig. 21, except for 0300 UTC 18 December 1988.

relative to the storm, has moved farther north than the surface center. This reduces the efficiency of the upper-level forcing on the surface cyclone. The IR imagery clearly shows that the mid- and high-level clouds follow the maximum divergence aloft. As the surface storm starts to occlude, less coupling exists between the low-level forcing and the dynamics forcing vertical motion aloft, which probably accounts for the lower correlation between the clouds and the surface \mathbf{Q} vector forcing.

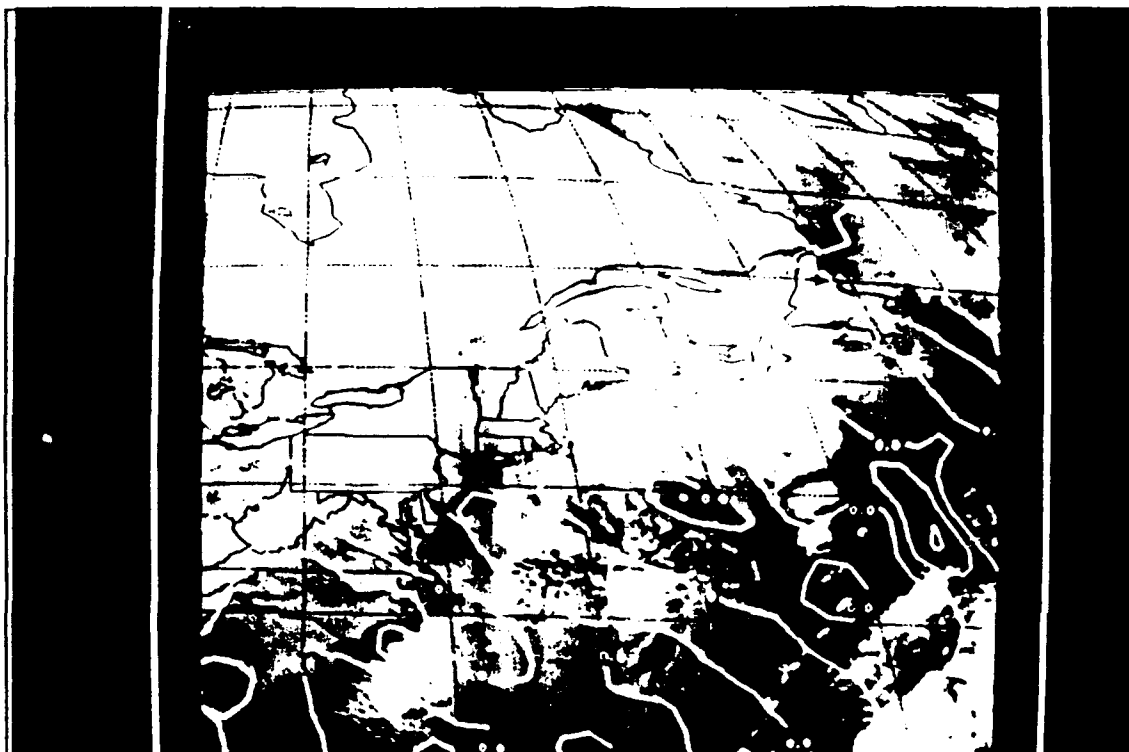


Fig. 27. GOES IR imagery and $-2\mathbf{V} \cdot \mathbf{Q}$ as in Fig. 22, except for 0301 UTC 18 December 1988.

By 1800 UTC 18 December (not shown), the upper-level dynamics supporting the low are north-northeast of the surface low. The IOP 3 cyclone has reached its minimum central pressure of 975 mb, and although it is still supporting winds over 25 m s^{-1} , the coldest-topped clouds and heaviest precipitation have moved north and northeast of the storm. The areas of maximum surface \mathbf{Q} vector convergence do not correlate well with the high, cold cloud shield, although surface observations reported snow in regions where \mathbf{Q} vector convergence existed. The \mathbf{Q} vectors and their associated divergence fields are also probably less representative of the low-level vertical motion at this phase of the storm due to its proximity to land as shown in Fig. 29. The difference

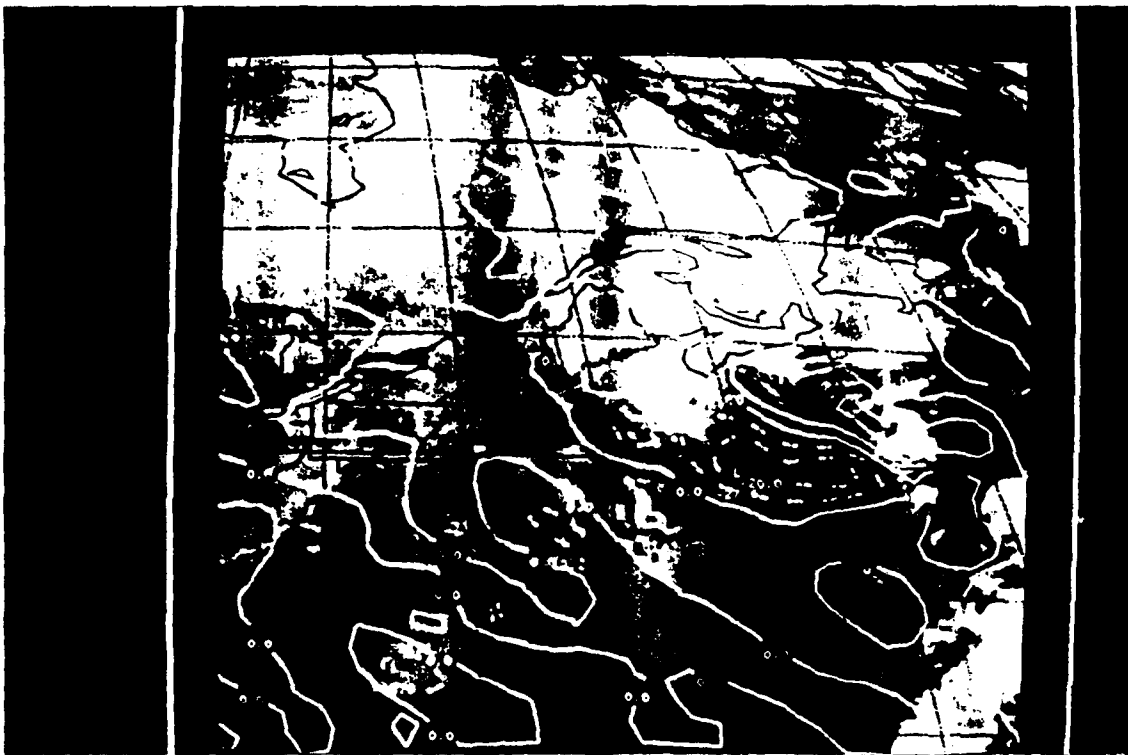


Fig. 28. GOES IR imagery and $-2\nabla \cdot \mathbf{Q}$ as in Fig. 22, except for 0601 UTC 18 December 1988.

in the temperature between the ocean and adjacent continent, although reflected throughout the lower- and middle-atmosphere, is the largest at the surface. This large temperature difference probably exaggerates and distorts the calculated low-level vertical velocity field derived by surface \mathbf{Q} vectors.

3. Objective Verification of \mathbf{Q} Vector Divergence

$-2\nabla \cdot \mathbf{Q}$ was compared to observations of vertical motion made on three flights into the storm. The correlations between the vertical velocity and $-2\nabla \cdot \mathbf{Q}$ are shown in Table 5. Two time periods had moderately positive correlations, two time periods had no correlation between the observed vertical motion and $-2\nabla \cdot \mathbf{Q}$, while the one time

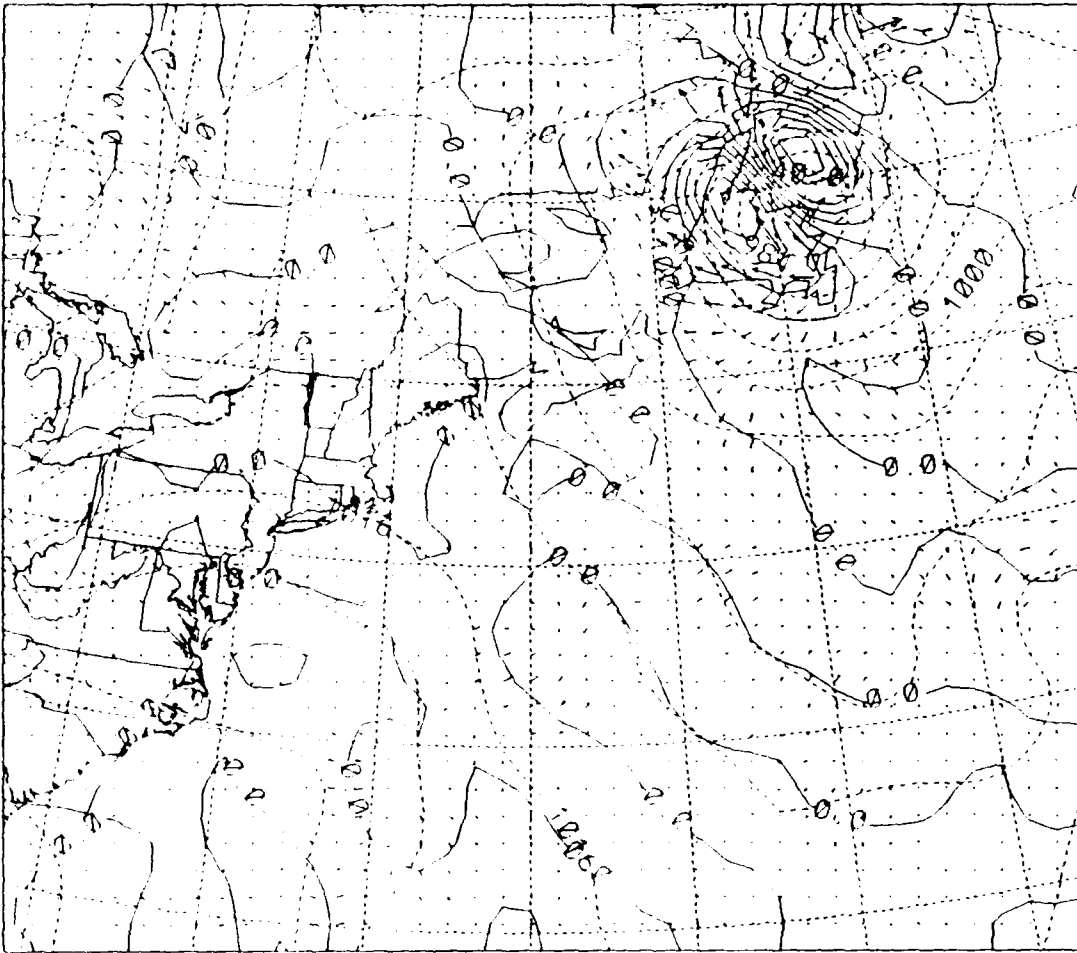


Fig. 29. $-2\nabla \cdot Q$, surface isobars and Q vectors as in Fig. 21, except for 1800 UTC 18 December 1988.

period centered around 0300 UTC 18 December had a moderately negative correlation. The high correlation in Fig. 30 is due to little variation in both the vertical velocity and $-2\nabla \cdot Q$ fields. The flight centered around 1200 UTC 18 Dec (Fig. 31) has a marked phase difference between the calculated and measured vertical velocities.

The generally low correlations between the vertical velocity and $-2\nabla \cdot Q$ may be due to the time difference between the aircraft measurement and the analysis. Although the 90 minute difference between aircraft and synoptic observations may not

Table 5. CORRELATION BETWEEN VERTICAL VELOCITY (w , cm s^{-1}) MEASURED BY AIRCRAFT AND $-2\nabla \cdot \mathbf{Q}$ ($\text{m kg}^{-1} \text{s}^{-1}$) DURING IOP 3.

Mean time of aircraft flight (DDHHMM UTC December 1988)	Number of observations	Correlation between w and $-2\nabla \cdot \mathbf{Q}$ for all observations	Number of observations < 1500 m	Correlation between w and $-2\nabla \cdot \mathbf{Q}$ for observations < 1500 m
171800	138	0.00	107	0.13
180000	68	0.52	54	0.65
180300	109	-0.40	85	-0.40
180900	118	0.63	54	0.41
181200	101	0.17	74	0.20

be significant in regions away from sharp gradients in the vertical velocity (i.e., fronts), this time difference should be accounted for when the aircraft is flying in the vicinity of a front. This explains the 30 minute phase difference shown in Fig. 31, and the relatively high correlations between $-2\nabla \cdot \mathbf{Q}$ and the vertical velocity as displayed in Fig. 30. Other sources of error include the aircraft sampling a region of mesoscale embedded convection for a time sufficient to alias the 20 minute average vertical velocity, and errors in the surface analysis with respect to the location of the strongest temperature gradients and regions of curvature in the pressure field. A combination of these errors and the phase differences does not allow conclusive results to be made from this method of verification.

Another method of evaluating the \mathbf{Q} vectors is to compare them to the isallobars for 3 h and 6 h in the future. Comparing the 1200 UTC 17 December \mathbf{Q} vectors with isallobars for 3 h (Fig. 32) and 6 h (Fig. 33) in the future graphically shows

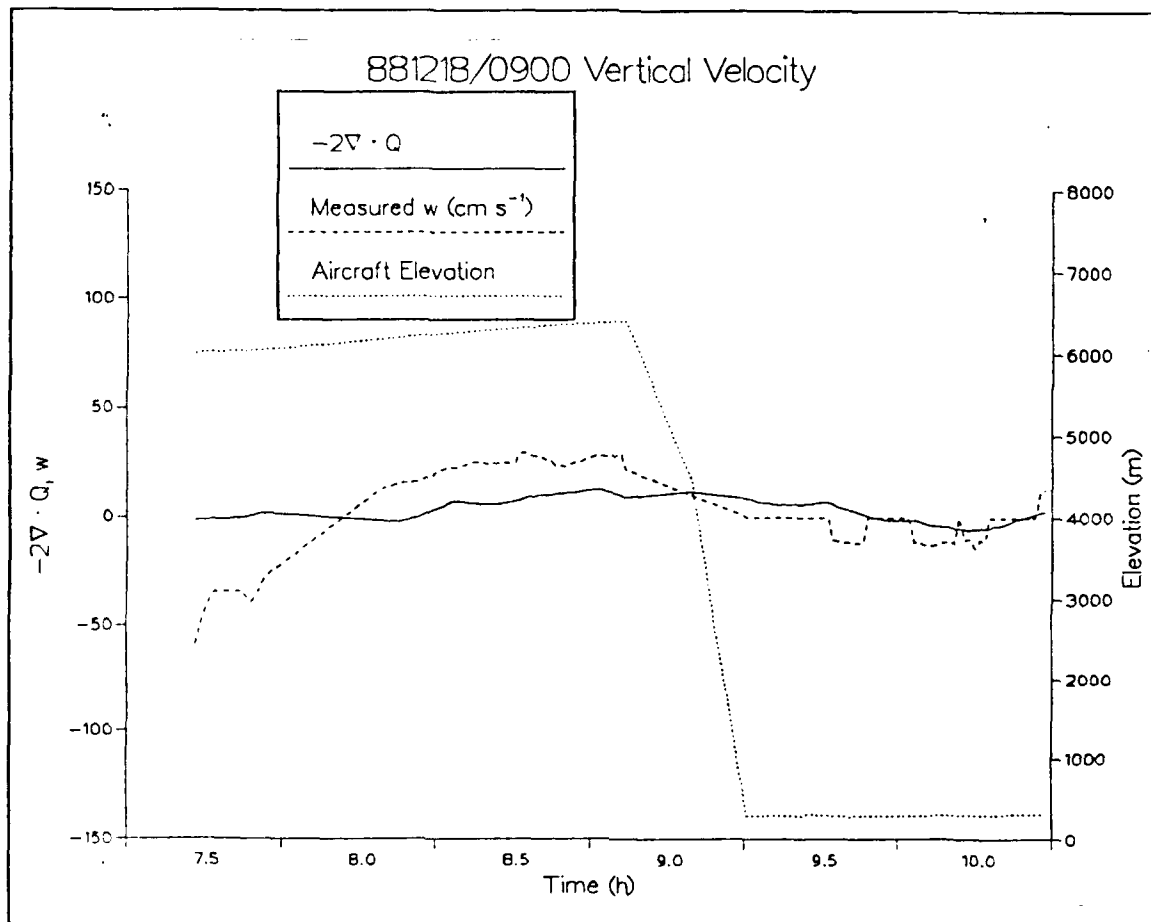


Fig. 30. Vertical velocity (cm s^{-1} , 20 minute average), $-2\nabla \cdot \mathbf{Q}$ ($\times 10^{-16} \text{ m kg}^{-1} \text{ s}^{-1}$) and aircraft elevation (m) centered around 0900 UTC 18 December 1988.

the relationship between these two fields. Such comparisons will reveal any qualitative similarities between the two fields that may not be apparent in the correlation calculations. The \mathbf{Q} vectors are convergent near the maximum pressure falls in Fig. 32, and Fig. 33 has convergent \mathbf{Q} vectors centered between two areas of pressure falls of 10-12 mb. Similar results are seen for \mathbf{Q} vectors calculated at 0000 UTC 18 December, and surface pressure tendencies for 3 h (Fig. 34) and 6 h (Fig. 35) in the future.

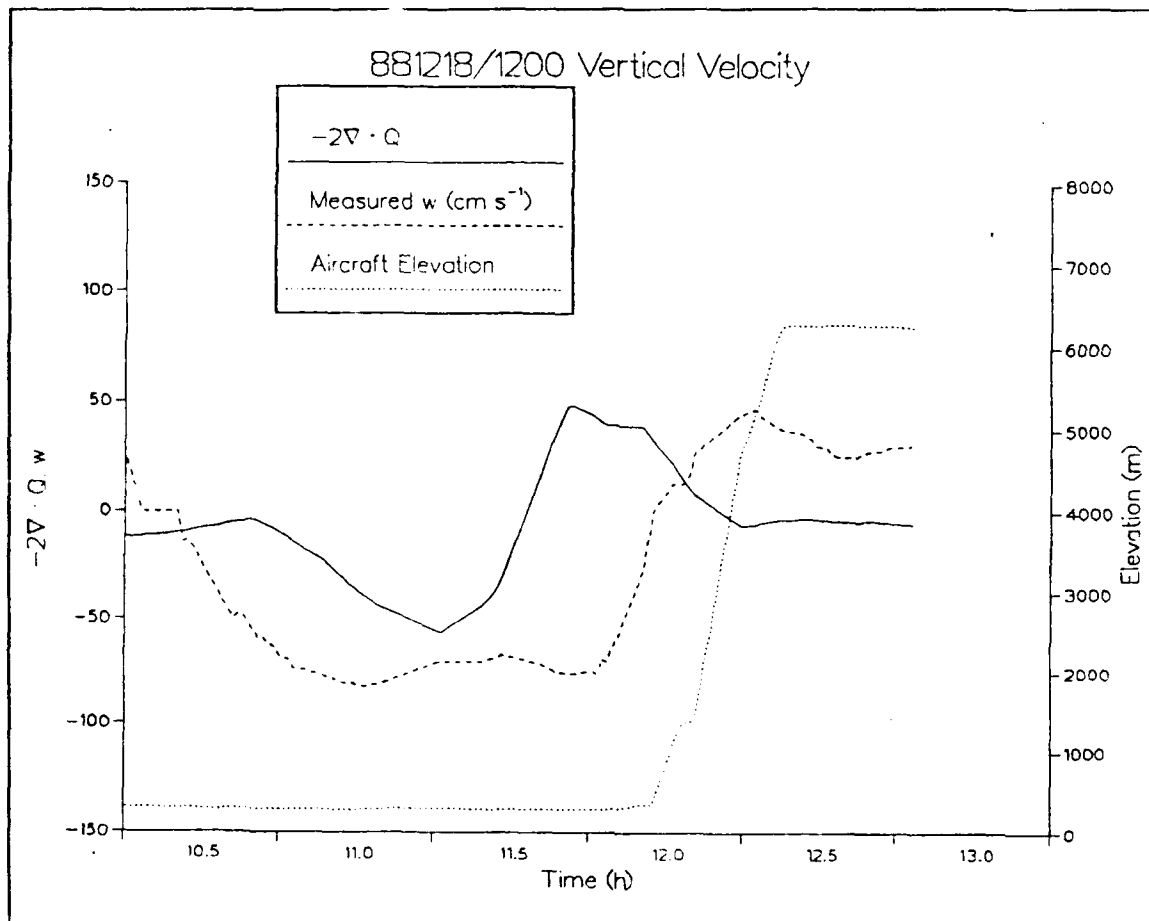


Fig. 31. Vertical velocity, $-2\nabla \cdot \mathbf{Q}$ and aircraft elevation as in Fig. 30, but centered around 1200 UTC 18 December 1988.

A more quantitative comparison is to create a scatter plot of $-2\nabla \cdot \mathbf{Q}$ vs. the pressure change for 3 h and 6 h in the future, and compute the correlation coefficients and linear regression equation. Table 6 lists the correlation coefficients and the regression equations for the IOP 3 cyclone. Correlations are negative, which is expected, since $-2\nabla \cdot \mathbf{Q} > 0$ is an area of \mathbf{Q} vector convergence that implies upward vertical motion and falling surface pressures. Correlations are consistently between -0.4 and -0.6, depending upon the minimum magnitude of $-2\nabla \cdot \mathbf{Q}$ used. The scatter plots for 3 h and 6 h in the

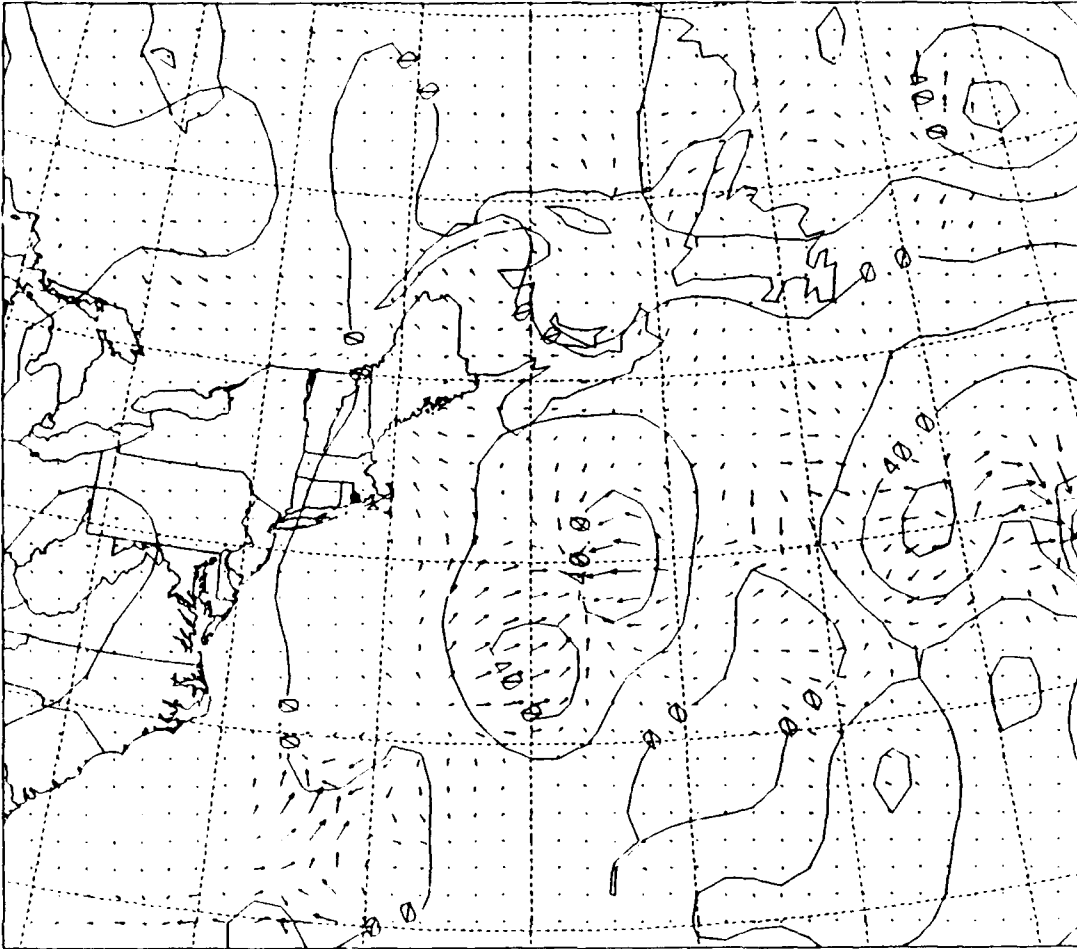


Fig. 32. Q vectors (arrows) at 1200 UTC 17 December 1988 and isallobars ($\text{mb} \cdot 10$ per 3 h, solid) for 1500-1200 UTC 17 December 1988.

future are displayed in Fig. 36 and Fig. 37. These figures show that the correlation between $-2\nabla \cdot Q$ and future pressure tendencies is high for regions of Q vector divergence, especially where $-2\nabla \cdot Q \leq -20 \times 10^{-16} \text{ m kg}^{-1} \text{ s}^{-1}$. There is more scatter for areas where $-2\nabla \cdot Q$ is positive, primarily because areas located near the center of the low where $-2\nabla \cdot Q > 0$ may experience a net rise in pressure if the low is to the north or east of that position after 3 h or 6 h.

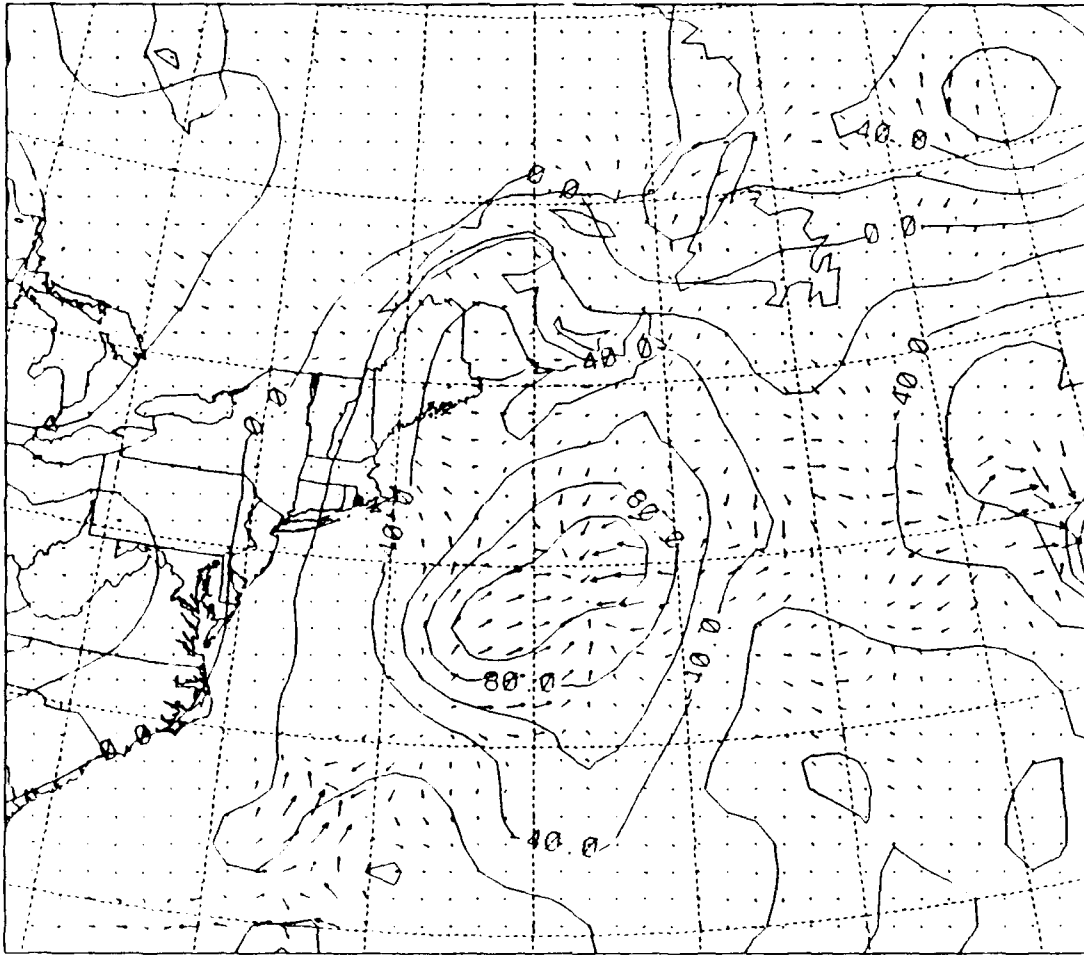


Fig. 33. Q vectors (arrows) at 1200 UTC 17 December and isallobars (mb*10 per 6 h, solid) for 1800-1200 UTC 17 December 1988.

Table 7 and Table 8 are comparisons of the Q vector divergence with the future 3-h and 6-h pressure changes, respectively, during the IOP 3 cyclone. This table also reveals significant differences between areas of convergence and divergence, especially after 1200 UTC 17 December, which is the start of the storm's rapid deepening phase. Between 0600 UTC 17 December and 1200 UTC 18 December, areas that had $-2\nabla \cdot \mathbf{Q}$ values of at least $10 \times 10^{-16} \text{ m kg}^{-1} \text{ s}^{-1}$ (convergence) experienced an average 3.0 and 4.4 mb decrease in pressure over the following 3 h and 6 h, respectively. Areas with

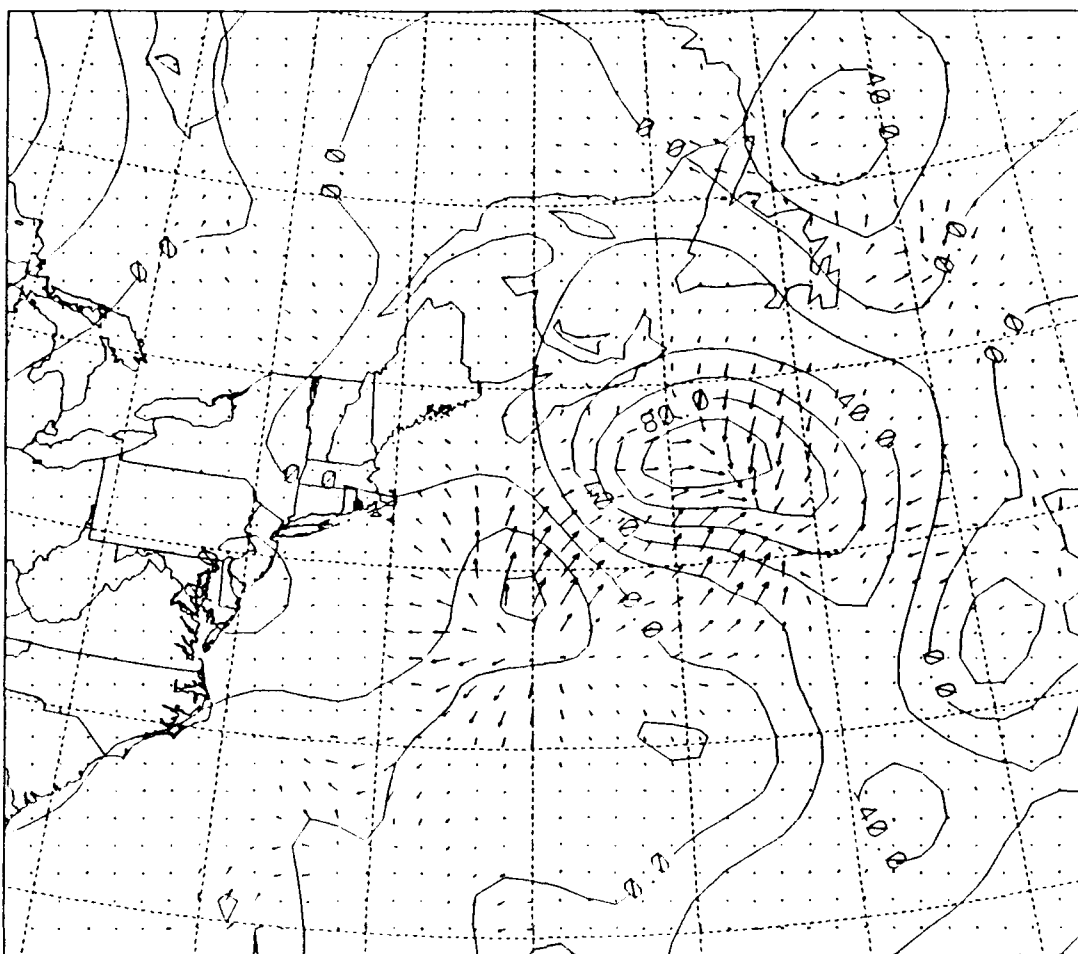


Fig. 34. Q vectors (arrows) at 0000 UTC 18 December 1988 and isallobars ($\text{mb} \cdot 10$ per 3 h, solid) for 0300-0000 UTC 18 December 1988.

$-2\nabla \cdot Q$ values of $-10 \times 10^{-16} \text{ m kg}^{-1} \text{ s}^{-1}$ or less (divergence) had average rises in pressure of 1.6 and 3.2 mb during the next 3 h and 6 h. For times after 0600 UTC 17 December, areas with convergence values of at least $10 \times 10^{-16} \text{ m kg}^{-1} \text{ s}^{-1}$ had, to a 95% confidence level, a statistically significant lower pressure 3 h (Fig. 38) and 6 h (Fig. 39) in the future than regions with divergence values of $10 \times 10^{-16} \text{ m kg}^{-1} \text{ s}^{-1}$ or greater.

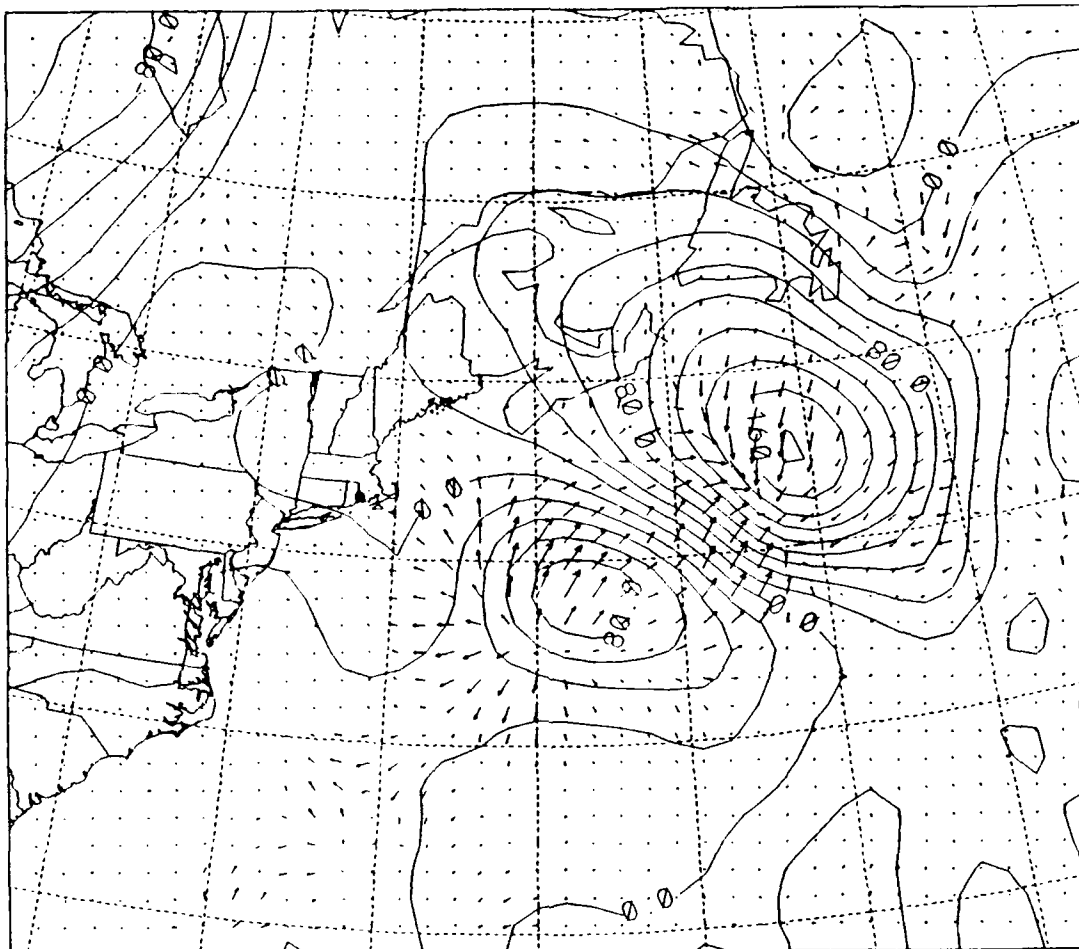


Fig. 35. Q vectors (arrows) at 0000 UTC 18 December 1988 and isallobars (mb*10 per 6 h, solid) for 0600-0000 UTC 18 December 1988.

Table 6. CORRELATION COEFFICIENTS AND LINEAR REGRESSION EQUATIONS FOR THE IOP 3 CYCLONE.

Δt (h in the future)	Number of Data Points	Standard Deviation of the Regression Line	Regression Equation	Correlation between the Pressure Change and $-2\nabla \cdot Q$
Regression Equation is in the form $y = a + bx$, where y = Pressure change (mb*10) Δt hours in the future $x = -2\nabla \cdot Q \times 10^{-16} \text{ m kg}^{-1} \text{ s}^{-1}$				
3	581	42.2	$y = -6.6 - 0.96x$	-0.42
6	581	74.6	$y = -4.2 - 1.7x$	-0.42

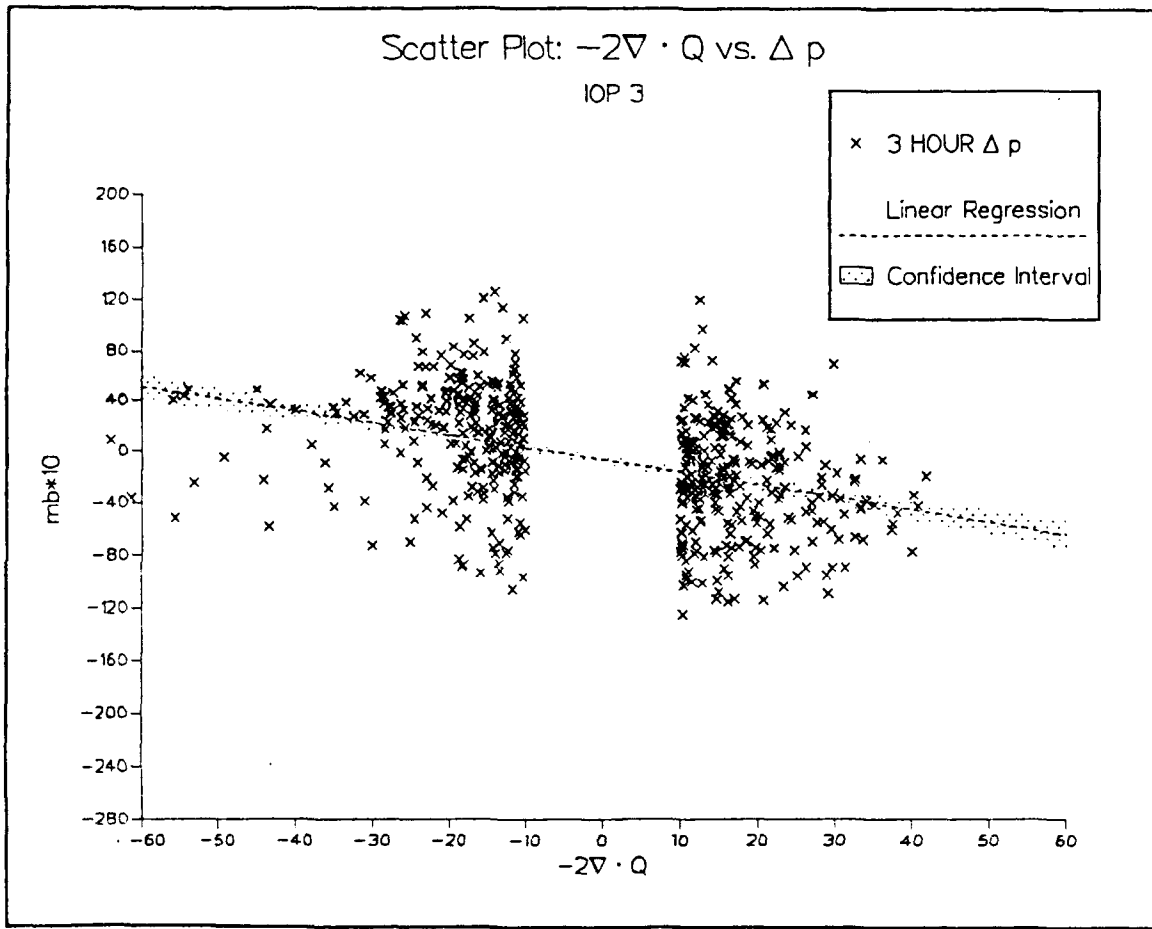


Fig. 36. Scatter plot of $-2\nabla \cdot Q$ ($\times 10^{-16} \text{ m kg}^{-1} \text{ s}^{-1}$) vs. the future 3 h pressure tendency ($\text{mb} \times 10$), linear regression line (dashed) and 95% confidence interval (dotted) for IOP 3.

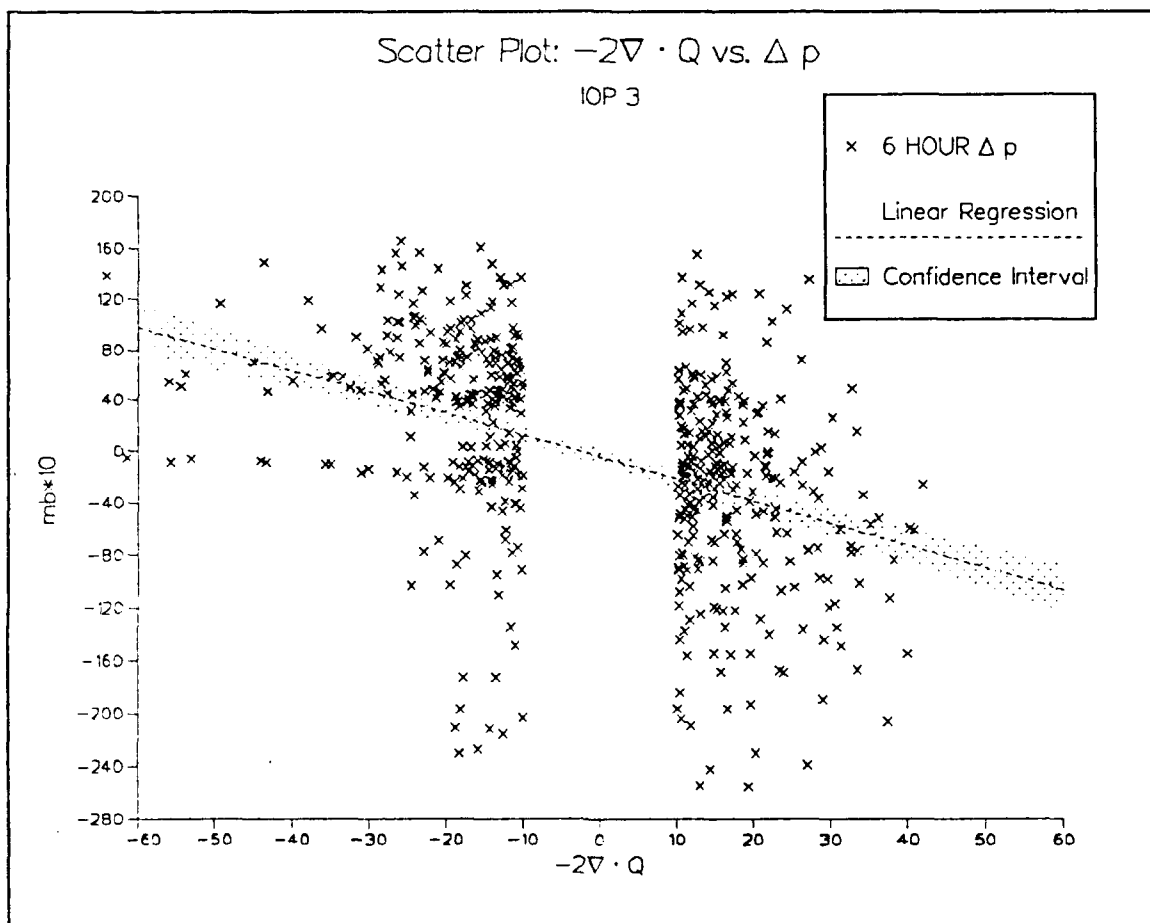


Fig. 37. Scatter plot of $-2\nabla \cdot Q$ ($\times 10^{-16} \text{ m kg}^{-1} \text{ s}^{-1}$) vs. the future 6 h pressure tendency (mb*10), linear regression line (dashed) and 95% confidence interval (dotted) for IOP 3.

Table 7. $-2\nabla \cdot \mathbf{Q}$ VS. 3 H FUTURE PRESSURE TENDENCY FOR THE IOP 3 CYCLONE.

Time (DDHH UTC December 1988)	Threshold value for $-2\nabla \cdot \mathbf{Q}$ ($\times 10^{-16} \text{ m kg}^{-1} \text{ s}^{-1}$)	Number of grid points	Mean pressure change (mb) in 3 h	Standard Deviation
1706	-10	19	-1.1	1.2
	+10	26	-1.2	1.6
1712	-10	19	-4.4	1.9
	+10	23	-5.0	2.2
1718	-10	22	2.8	1.9
	+10	18	-2.0	2.3
1800	-10	21	1.5	3.6
	+10	21	-7.4	3.0
1806	-10	31	2.9	1.3
	+10	27	-1.0	4.1
1812	-10	39	4.3	6.2
	+10	46	-2.2	4.8

Table 8. $-2\nabla \cdot \mathbf{Q}$ VS. 6 H FUTURE PRESSURE TENDENCY FOR THE IOP 3 CYCLONE.

Time (DDHH UTC December 1988)	Threshold value for $-2\nabla \cdot \mathbf{Q}$ ($\times 10^{-16} \text{ m kg}^{-1} \text{ s}^{-1}$)	Number of grid points	Mean pressure change (mb) in 6 h	Standard Deviation
1706	-10	19	-1.5	1.7
	+10	26	-2.2	2.3
1712	-10	19	-1.3	0.5
	+10	23	-6.0	2.9
1718	-10	22	5.3	2.3
	+10	18	-2.1	5.0
1800	-10	21	4.3	4.5
	+10	21	-10.3	5.0
1806	-10	31	8.1	2.6
	+10	27	-2.3	5.3
1812	-10	39	5.6	10.5
	+10	46	-5.3	11.6

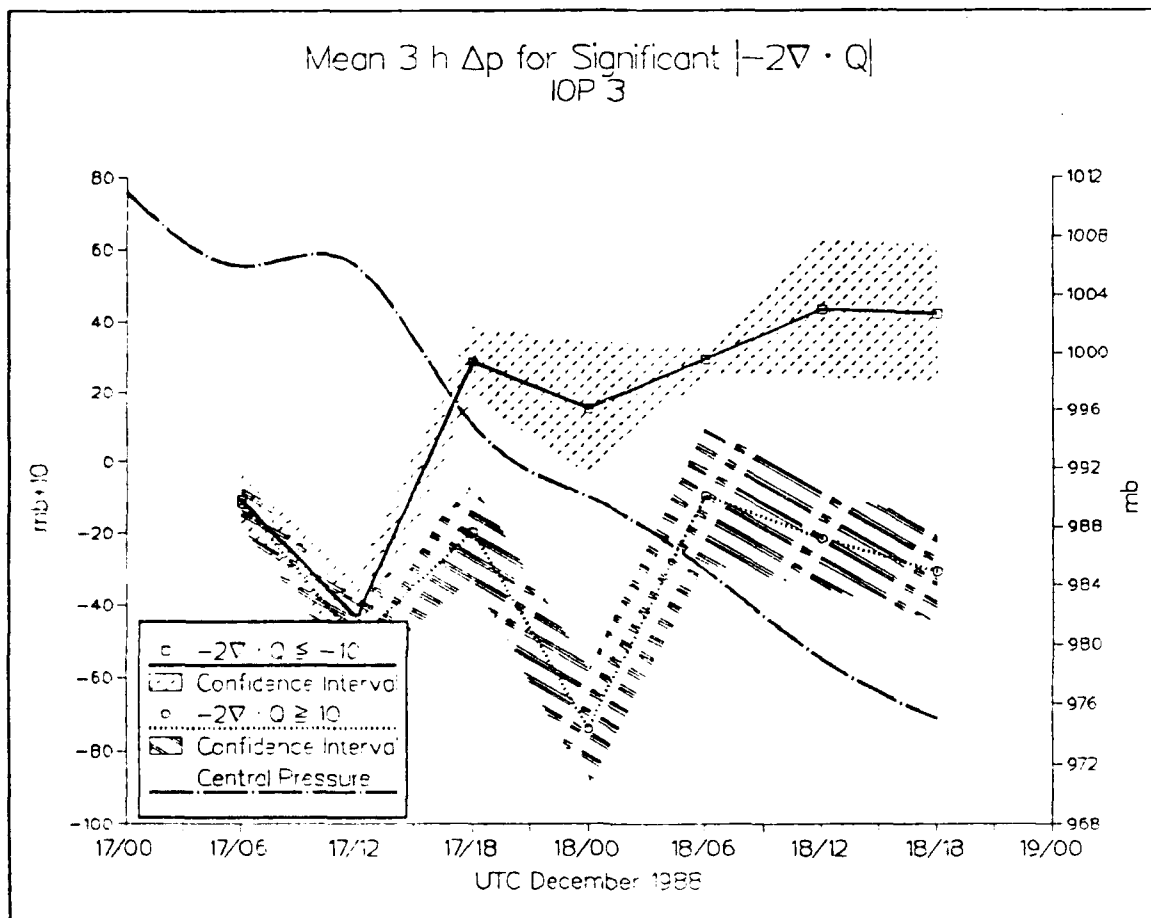


Fig. 38. Mean 3 h pressure tendency for significant (see text) $|-2\nabla \cdot Q|$ (solid and dotted lines), 95% confidence intervals (hatched) and analyzed central pressure of the IOP 3 storm (dash-dot).

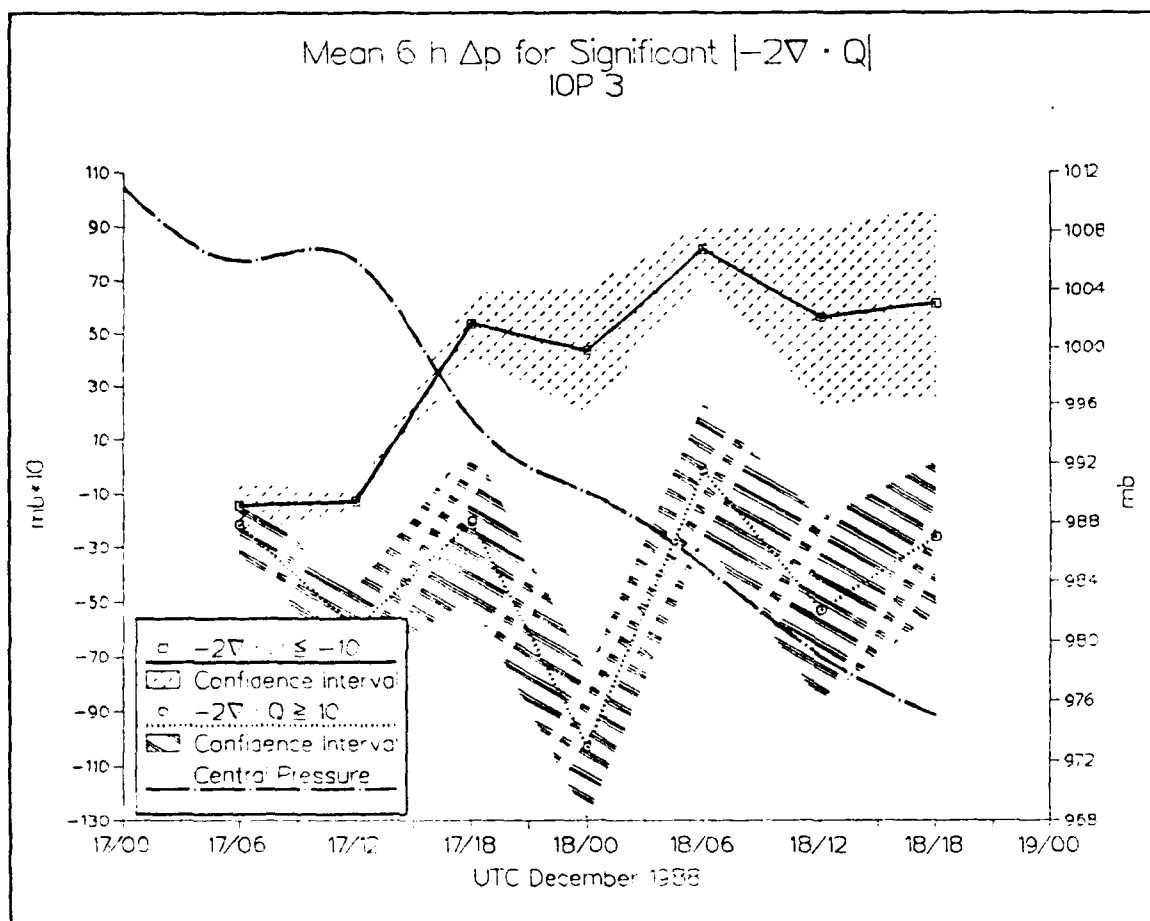


Fig. 39. As in Fig. 38, except for 6 h pressure tendency.

B. IOP 5

1. Synoptic Overview

The IOP 5 cyclone (Fig. 40) experienced rapid deepening, with the central pressure decreasing 20 mb between 1200 UTC 19 January and 0000 UTC 20 January 1989, and 32 mb in the 24 h commencing at 1200 UTC 19 January. This deepening rate of 10 mb (6h)^{-1} met the ERICA criteria for rapid intensification, although Sanders' analysis of the IOP 5 storm had less rapid deepening than was initially shown by Forbes (Hadlock *et al.* 1989). This storm initially developed just east of New Jersey (Fig. 41) and moved east-northeast at 50 km h^{-1} until 0000 UTC 20 January, when it increased in speed to 65 km h^{-1} . As the track approached the eastern edge of the ERICA domain, accurate surface analyses were inhibited toward the end of the IOP.

By 0000 UTC 19 January (Fig. 42), pressures along the mid-Atlantic coast had fallen 4-6 mb in the past 6 h in response to an intensifying short-wave approaching from the west. Although not shown in Fig. 41, this marks the beginning of the surface cyclogenesis for IOP 5. The thermal structure (Fig. 42) initially had a weaker gradient than in IOP 3, but the surface low developed on the southern edge of the gradient, and rapidly created an intense thermal gradient through self-development processes. As in the IOP 3 cyclone, this storm was also a case of an initial surface disturbance being overtaken by a strong short-wave in the mid-troposphere. However, the IOP 5 storm lacked a distinct long-wave trough along the eastern US, and the upper-level flow was more zonal (Fig. 43) than in the IOP 3 cyclone. The IOP 5 cyclone was initially typical of the

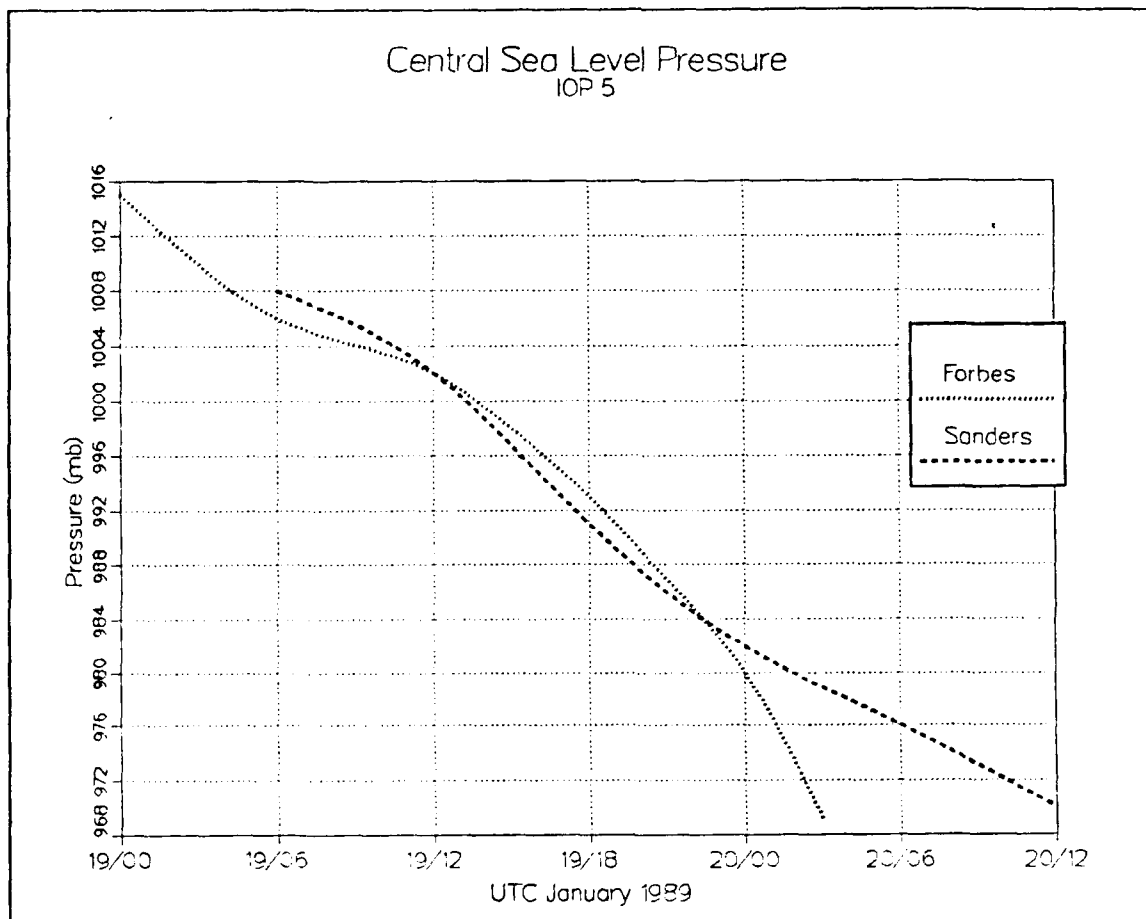


Fig. 40. Analyzed central pressure (mb) vs. time for IOP 5.

"secondary redevelopment" pattern of cyclogenesis as discussed by Kocin and Uccellini (1990).

The 1200 UTC 19 January surface pressure and temperature analyses (Fig. 44) indicated that the low has tracked along the south wall of the Gulf Stream (Fig. 45), so that the surface flux of sensible heat tends to maintain a moderate to strong surface baroclinic zone to the east of the storm. Surface temperatures range from 15°C just south of the warm front to 2°C about 400 km north of the warm front. The southern baroclinic

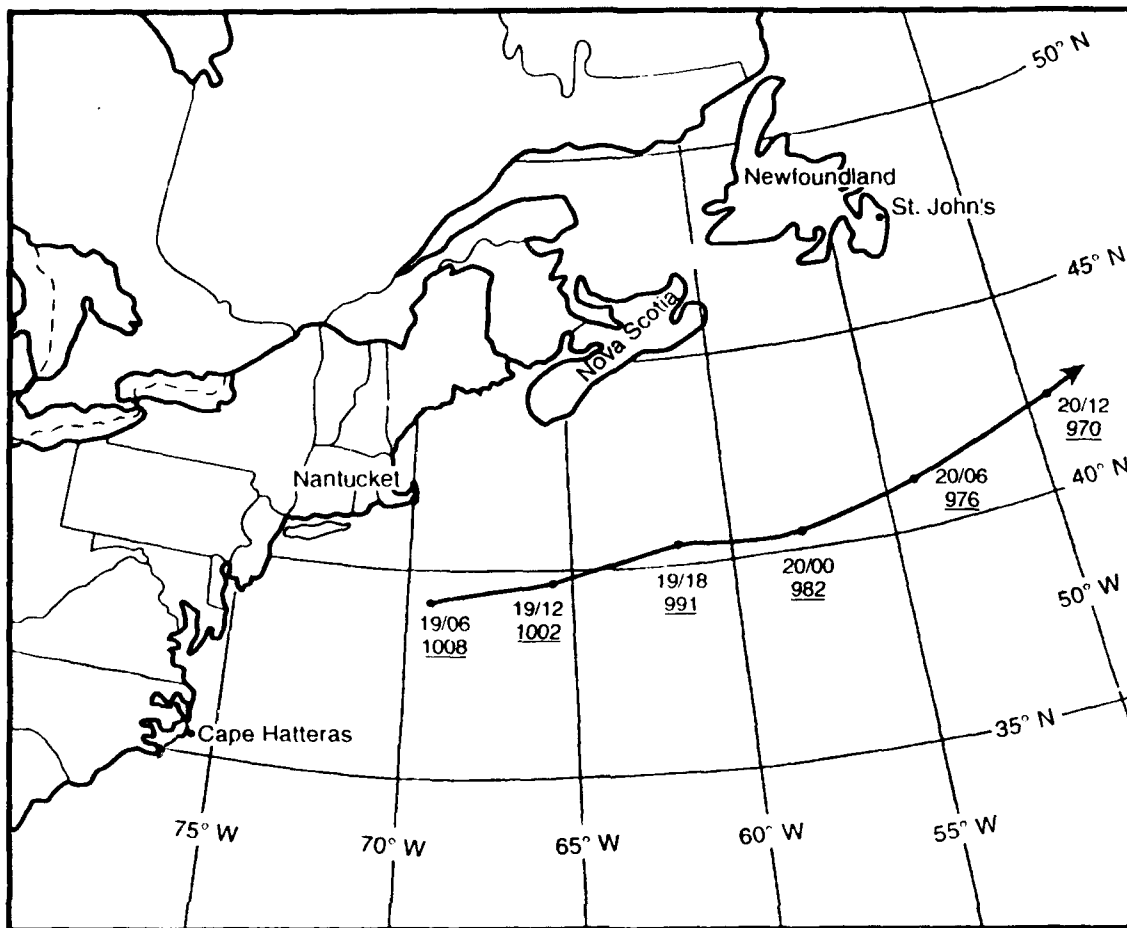


Fig. 41. Storm track as in Fig. 10, except for IOP 5 storm. Time is UTC, January 1989.

zone has become the dominant thermal feature in the 1000-500 mb thickness field at 1200 UTC 19 January, with the surface low located in an optimum position on the southern edge of the anticyclonically curving thickness field.

A significant change has occurred in the structure of the wind field north of the low during the past 6 h. Surface wind observations from ships "CGBL", "DLEZ" and buoy "44137" (Fig. 44) depict significant ageostrophic flow north of the warm front. As previously described in IOP 3 and by Nuss and Kanikawa (1990), this flow is parallel

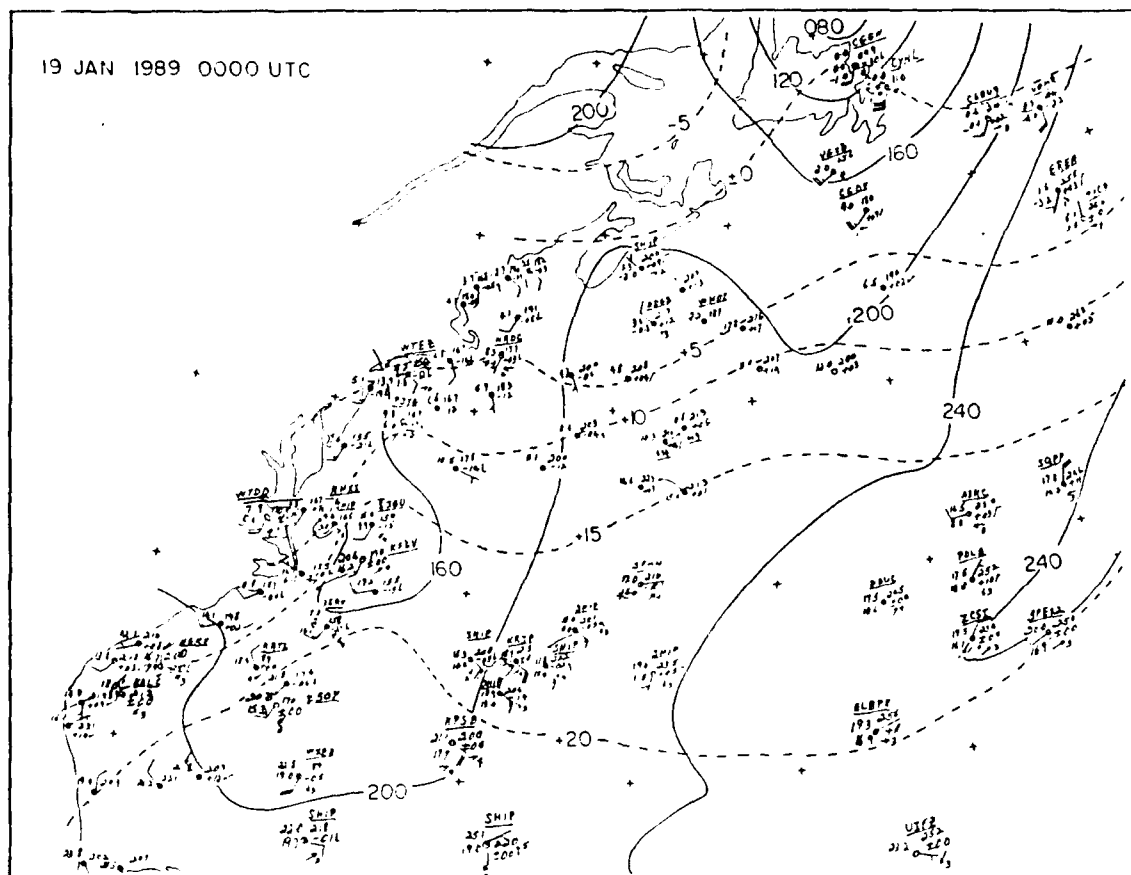


Fig. 42. Surface pressure and temperature analysis as in Fig. 7, except for 0000 UTC 19 January 1989.

to the surface isotherms. As in IOP 3, specific sounding data have not been examined. Nevertheless, low-level air appears to be originating over Newfoundland and Labrador and then is being advected south and west across sea-surface temperatures 15-25°C warmer than the initial surface temperatures. Consequently, this layer is most likely well mixed through at least the lowest 1-2 km of the atmosphere. This strong ageostrophic flow may be linked to a thermally direct circulation from a developing 300 mb jet streak northeast of the surface low, south of Newfoundland (Fig. 46). As noted by Kocin and Uccellini (1990), this direct circulation contributes to the intensification of the cyclone.

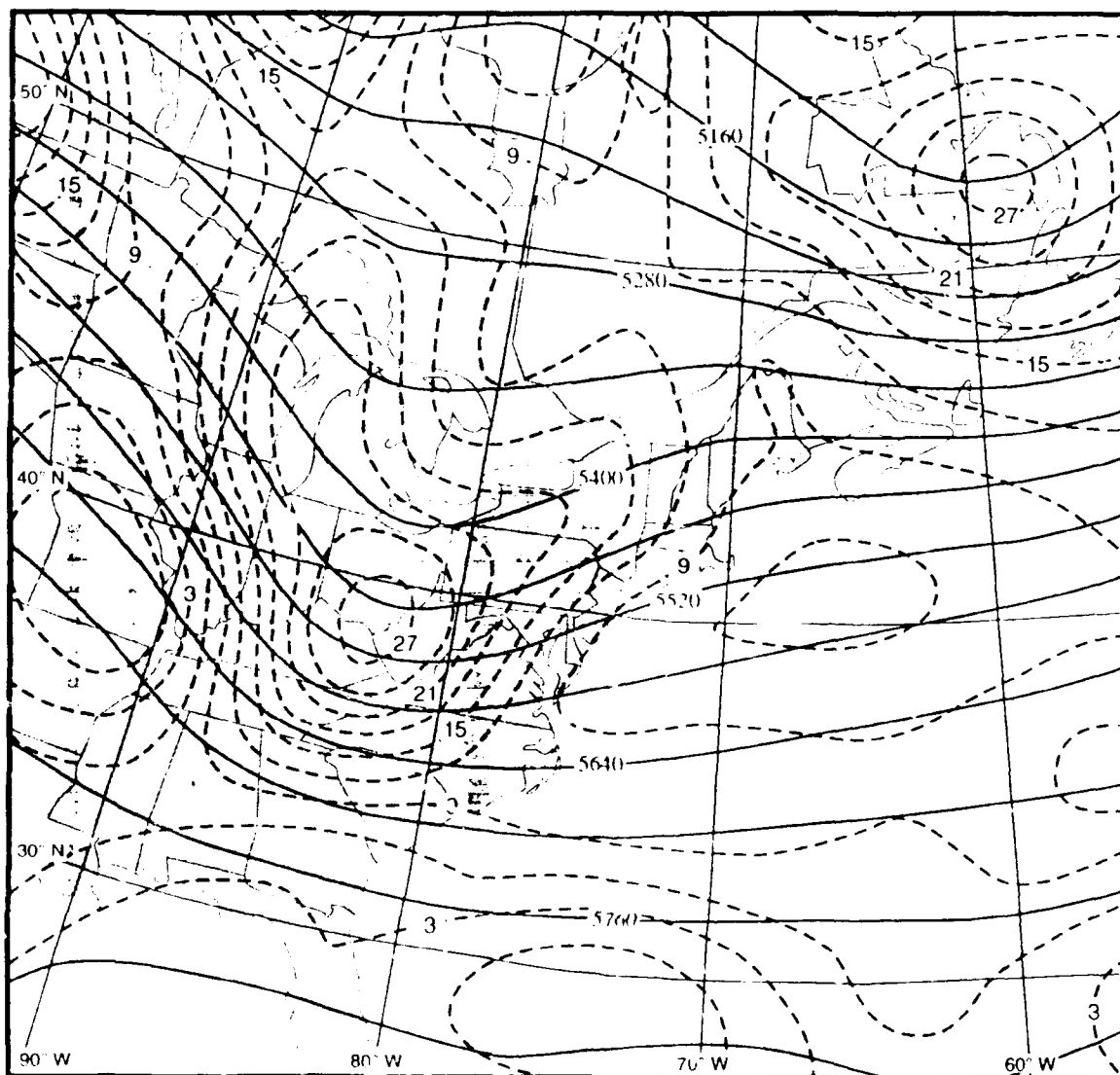
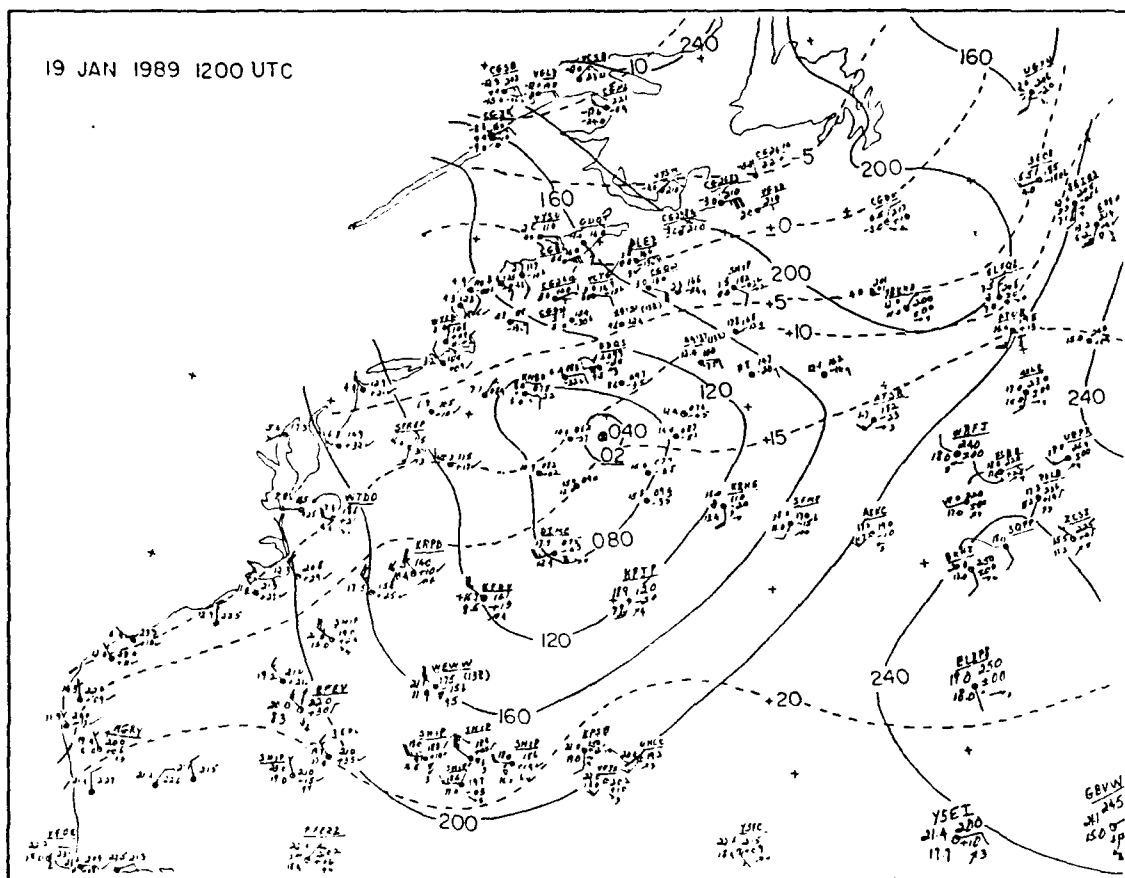


Fig. 43. 500 mb height and absolute vorticity analysis as in Fig. 11, except for 0000 UTC 19 January 1989.

The ageostrophic flow north of the warm front and associated direct circulation persisted for over 24 h in IOP 5, and may be one reason why IOP 5 deepened more quickly than IOP 3, despite the similarity of the 500 mb short waves in both storms.

The 500 mb and 300 mb flows are also favorable for additional deepening of the IOP 5 cyclone. The 500 mb amplifying short-wave is now analyzed as a vorticity



maximum in excess of $30 \times 10^{-5} \text{ s}^{-1}$, and is 250 km east of New Jersey (Fig. 47), which results in strong CVA to the east over the surface low. At 300 mb, in addition to the developing outflow jet supporting the warm front described above, the surface low is located under the left-front quadrant of a 60 m s^{-1} jet streak. The indirect secondary circulation associated with this jet streak further enhances the development of the surface storm.

The storm deepened 20 mb between 1200 UTC 19 January and 0000 UTC 20 January, when it was about 550 km southeast of Nova Scotia with a central pressure of

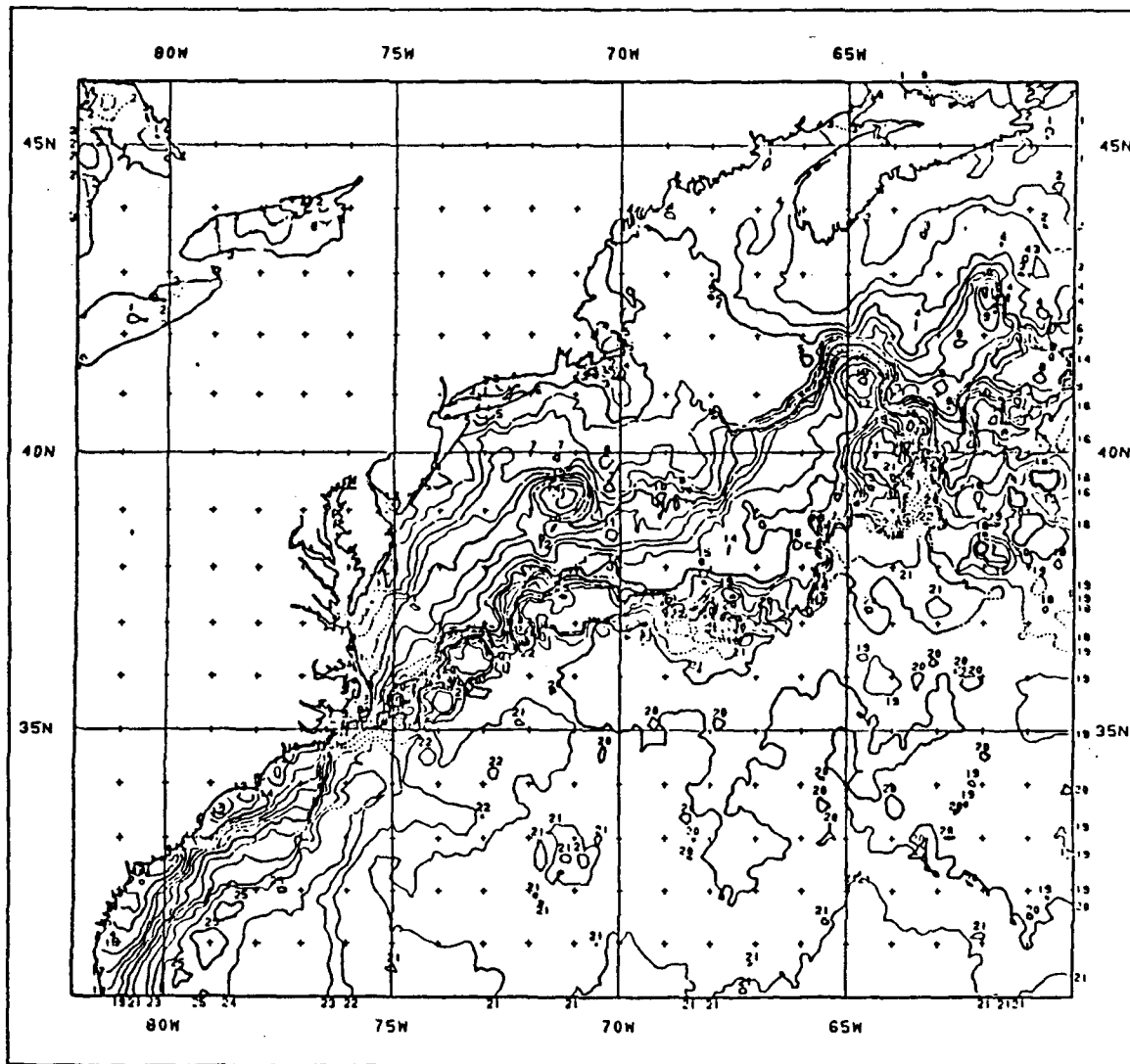


Fig. 45. Sea-surface temperatures as in Fig. 17, except for 18-20 January 1989.

982 mb (Fig. 48). Sustained wind speeds between $15\text{--}20\text{ m s}^{-1}$ are now being reported within 500 km of the storm center. The storm center is beginning to move northward into the lower surface temperatures, and the 1000-500 mb thickness chart (not shown) indicates the cyclone is beginning to occlude. The temperature gradient north of the warm front has further intensified to a 15°C temperature difference over 300 km, which

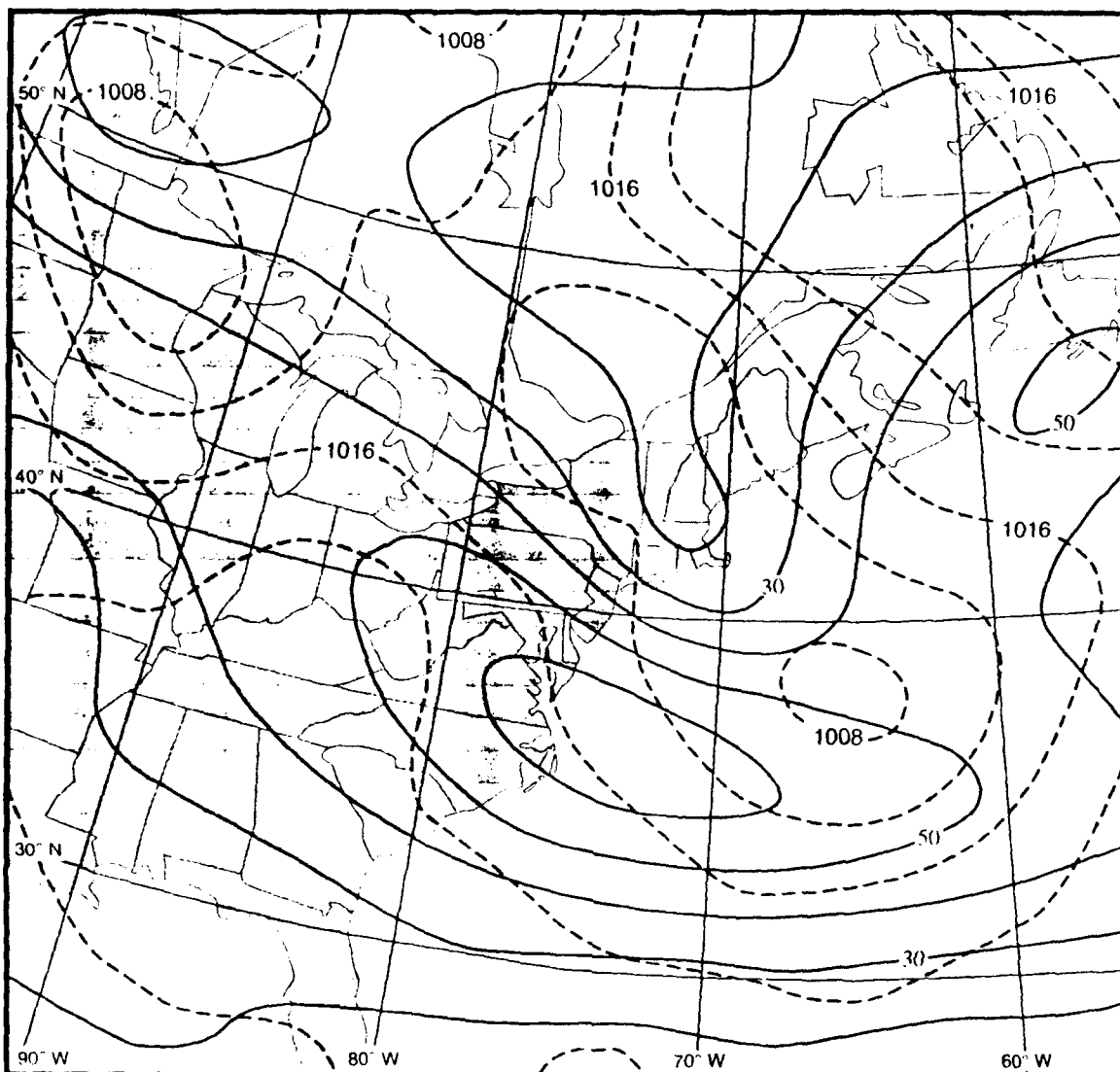


Fig. 46. 300 mb isotach and surface pressure analysis as in Fig. 15, except for 1200 UTC 19 January 1989.

is about three times as intense as the temperature gradient to the west along the cold front. Strong ageostrophic winds continue to be observed north of the warm front.

The 500 mb short-wave has continued to amplify, and the vorticity maximum has increased to more than $33 \times 10^{-5} \text{ s}^{-1}$ (Fig. 49). Although the surface low pressure is still under strong CVA, the most intense CVA is now north and east of the storm center. The

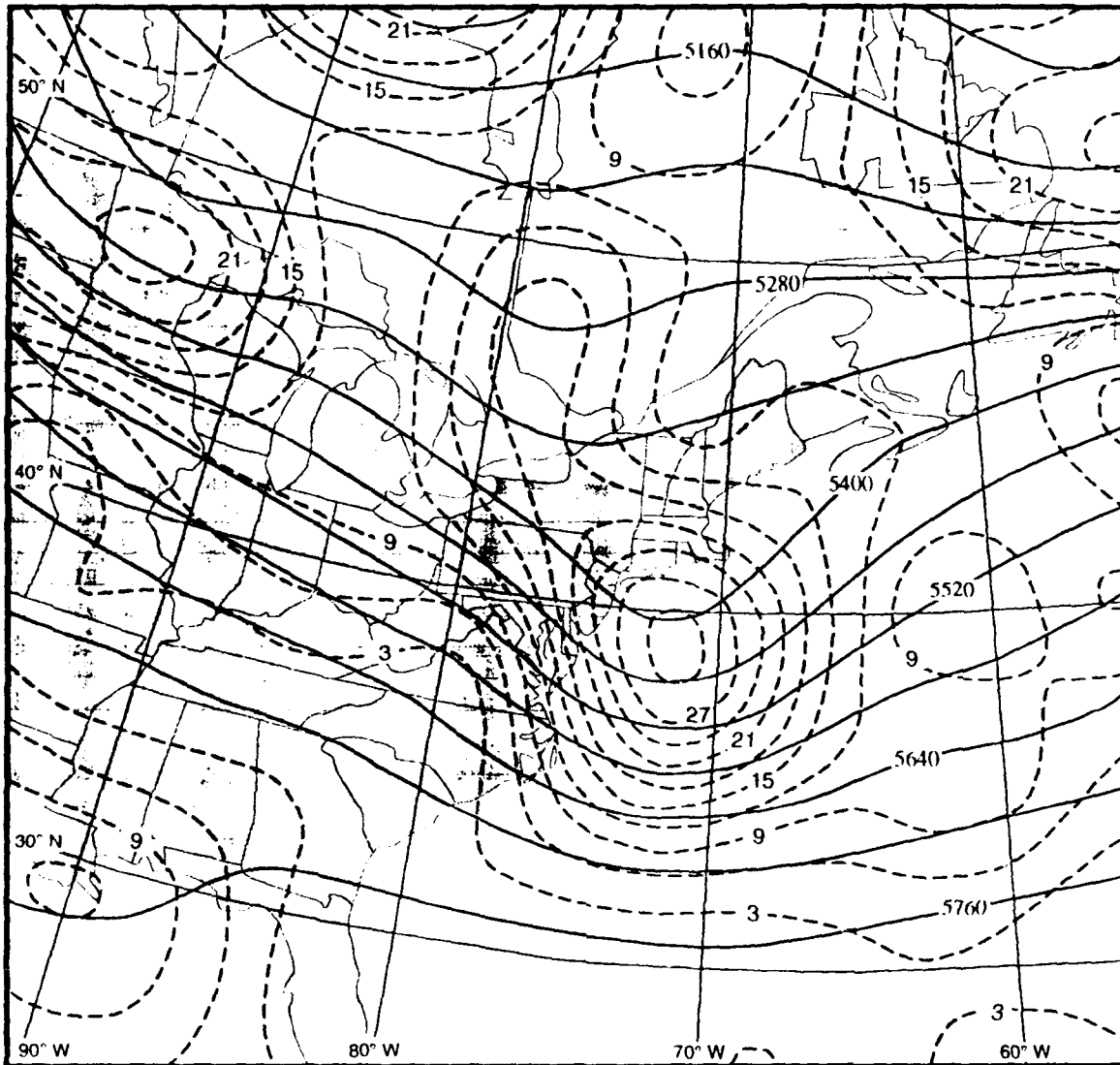


Fig. 47. 500 mb height and absolute vorticity analysis as in Fig. 11, except for 1200 UTC 19 January 1989.

short wave does not phase into a long wave trough, but continues to propagate eastward. This explains why the IOP 5 cyclone had less of a northerly track than did the IOP 3 cyclone. At 300 mb (Fig. 50), the NMC final analysis has the storm center under the left-front quadrant of a 50 m s^{-1} jet streak, which implies divergence aloft over the surface low. Another 50 m s^{-1} jet streak is east of Newfoundland, north-northeast of the storm,

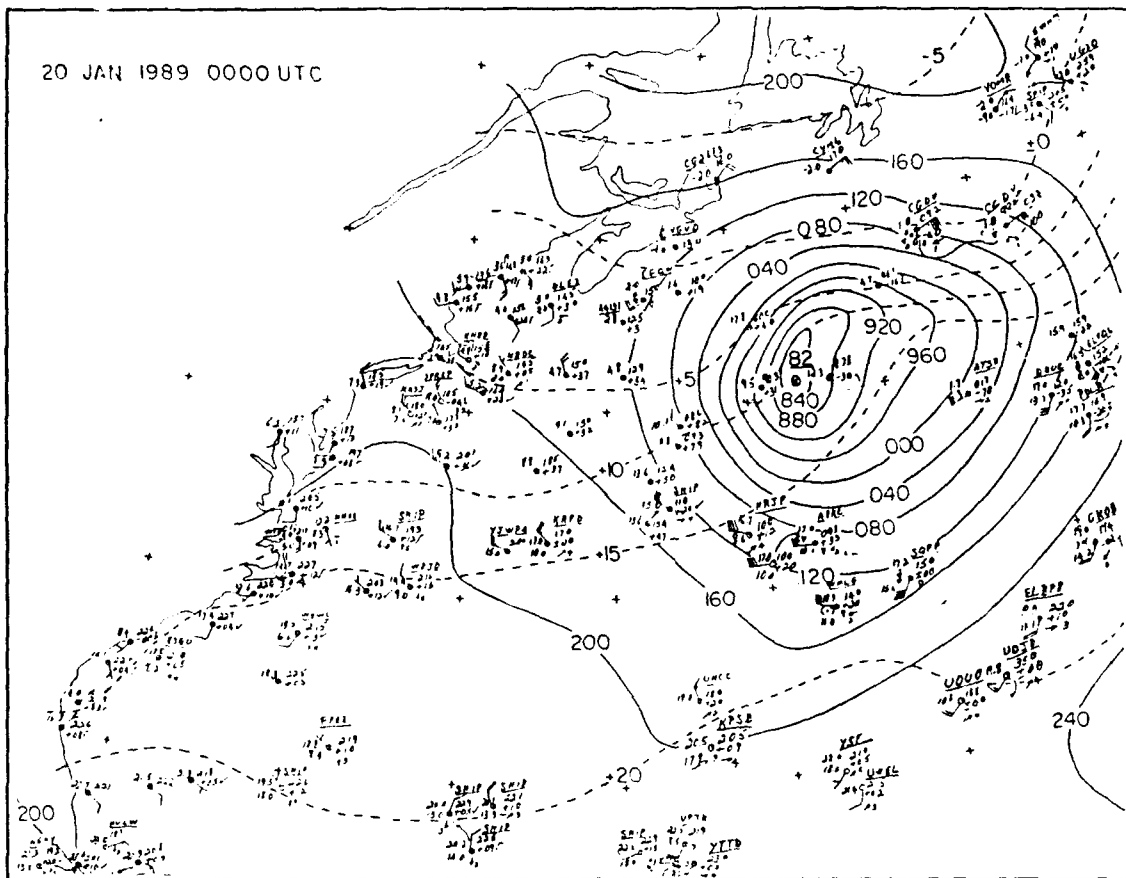


Fig. 48. Surface pressure and temperature analysis as in Fig. 7, except for 0000 UTC 20 January 1989.

which places the storm under the right-rear quadrant. This second jet streak is most likely maintaining a secondary direct circulation in conjunction with the cold low-level air north of the warm front.

At 1200 UTC 20 January (not shown), the occlusion process has continued, but the warm front has maintained intensity and ageostrophic flow is present. This may partially explain how the storm has deepened at least 12 mb in the past 12 h after the low occluded. A closed low was present at 500 mb (not shown), and most of the CVA was now to the northeast of the storm center. At 300 mb (not shown), a 50 m s^{-1} jet streak

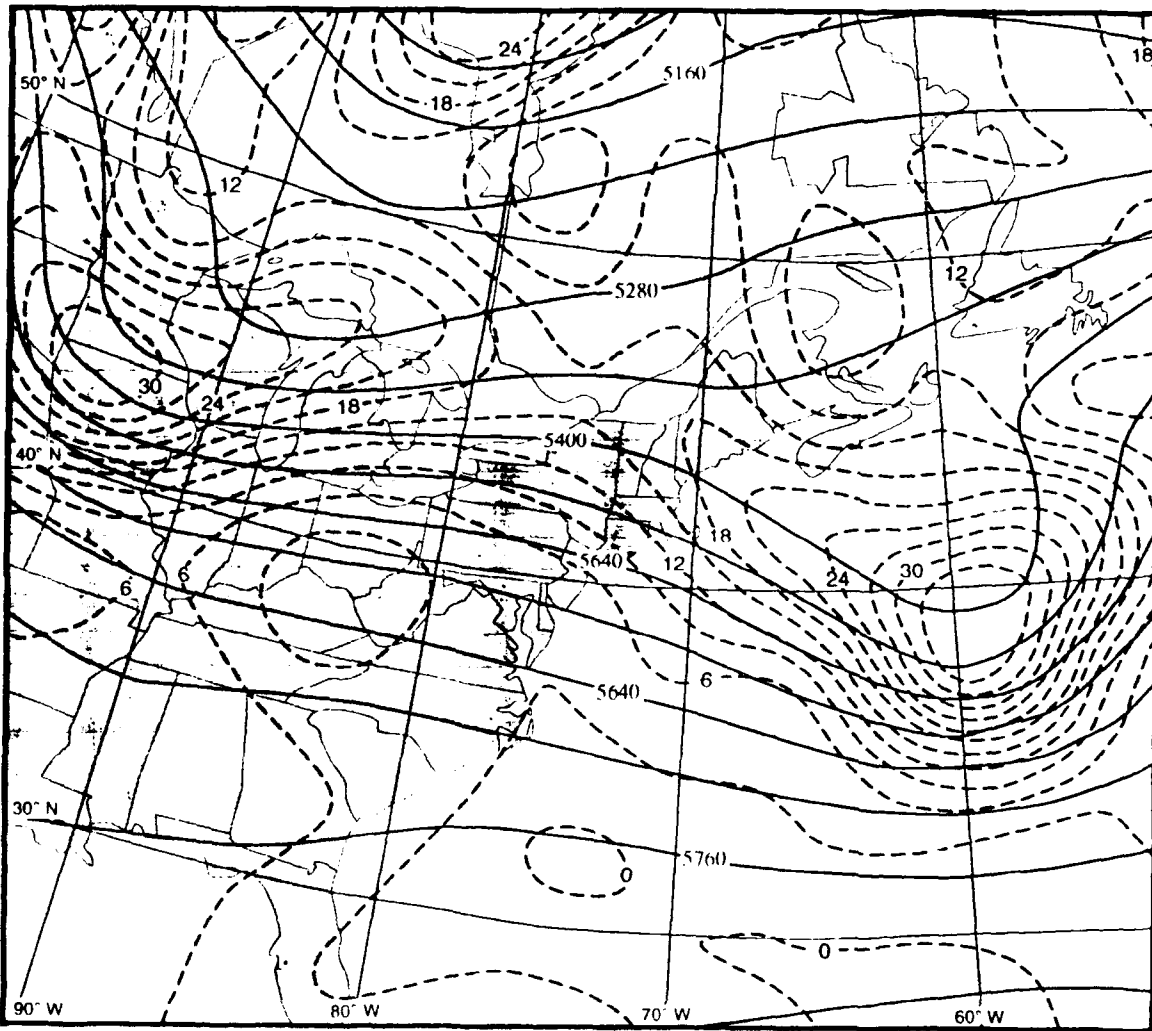


Fig. 49. 500 mb height and absolute vorticity analysis as in Fig. 11, except for 0000 UTC 20 January 1989.

well north of the storm may still have been supporting the warm front with the associated thermally direct circulation, but the center of the storm no longer has a jet streak in a favorable location to enhance development.

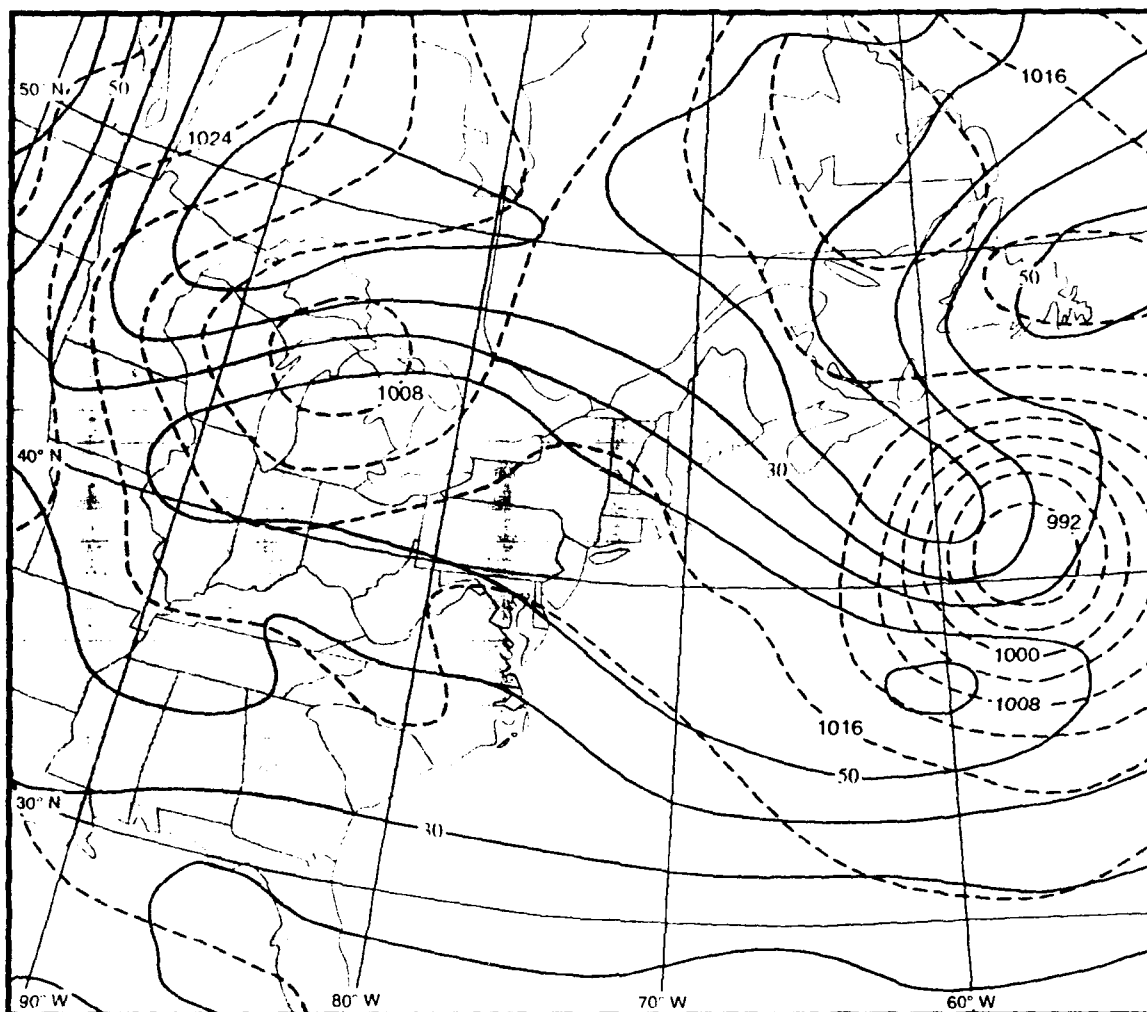


Fig. 50. 300 mb isotach and surface pressure analysis as in Fig. 15, except for 0000 UTC 20 January 1989.

2. Q Vectors and Satellite Imagery

As indicated in the synoptic overview, little surface development was evident between 1800 UTC 18 January and 0000 UTC 19 January 1989. Thus, no significant areas of Q vector divergence or convergence formed. An area of convergence with magnitudes between 5 and $7 \times 10^{-16} \text{ m kg}^{-1} \text{ s}^{-1}$ does persist about 400 km east-southeast of HAT (Fig. 51). The magnitude of $-2\nabla \cdot Q$ is weak, but it correlates very well with an area of convection on the IR satellite imagery for 0001 UTC 19 January (Fig. 52). The

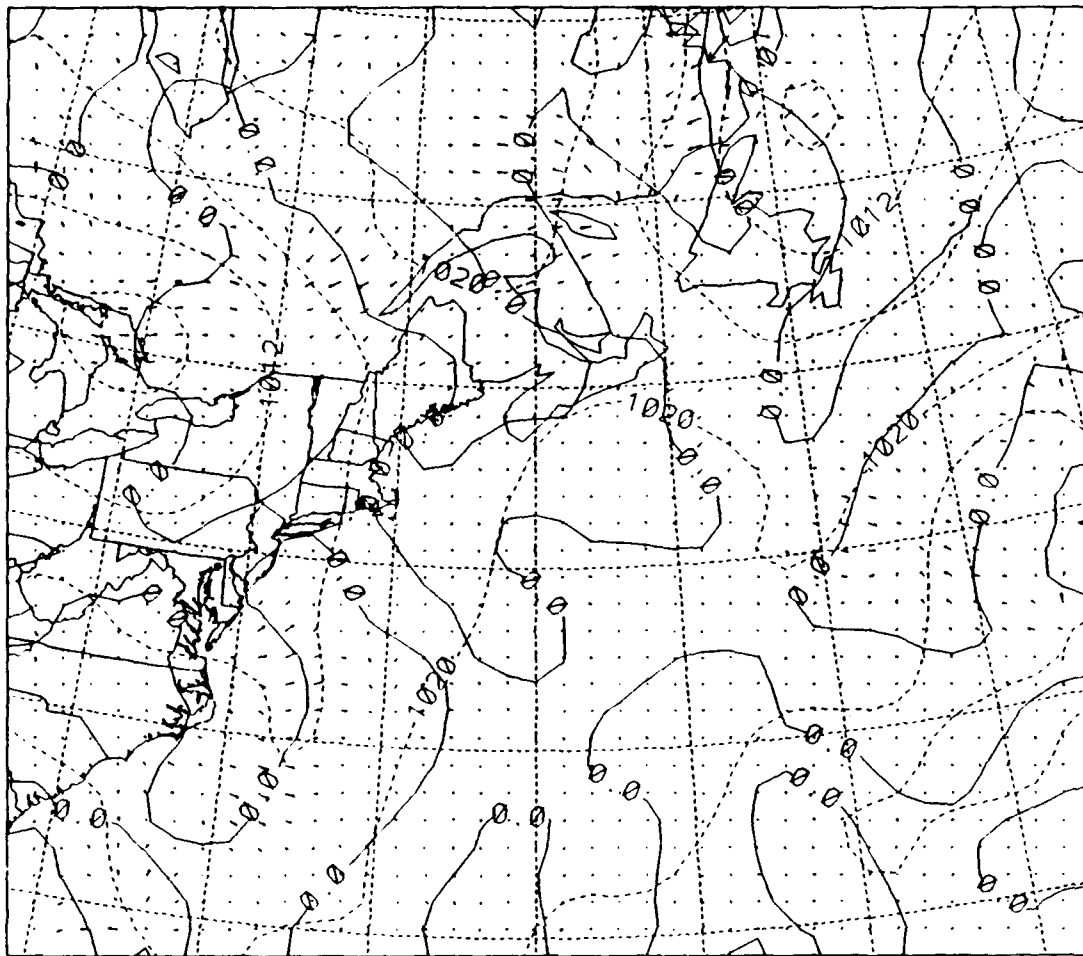


Fig. 51. $-2\nabla \cdot \mathbf{Q}$, surface isobars and \mathbf{Q} vectors as in Fig. 21, except for 0000 UTC 19 January 1989.

maximum forcing also correlates well with the surface low that develops east-northeast of HAT at 0300 UTC 19 January (Fig. 53). Additionally, the area of divergence immediately to the west matches well with the scattered cumulus and stratocumulus on the satellite imagery. As this time is still 12-18 h before the rapid deepening commences, it is not surprising that the surface forcing commences with such a small magnitude in this IOP.



Fig. 52. GOES IR imagery and $-2\mathbf{V} \cdot \mathbf{Q}$ as in Fig. 22, except for 0001 UTC 19 January 1989.

The comparison of \mathbf{Q} vector divergence and cloud development between 0300 and 0900 UTC 19 January demonstrates the usefulness of this diagnostic tool. Specifically, the satellite IR imagery (Fig. 54) shows a close match between areas of developing convection and \mathbf{Q} vector convergence, as well as areas that are either clear or contain only scattered boundary-layer clouds and \mathbf{Q} vector divergence. The area of organized convection, (as implied by the coldest cloud-top temperatures in the IR imagery) about 700 km east-northeast of HAT coincides extremely well with an area of \mathbf{Q} vector convergence with a magnitude of $16 \times 10^{-16} \text{ m kg}^{-1} \text{ s}^{-1}$. The area of strongest

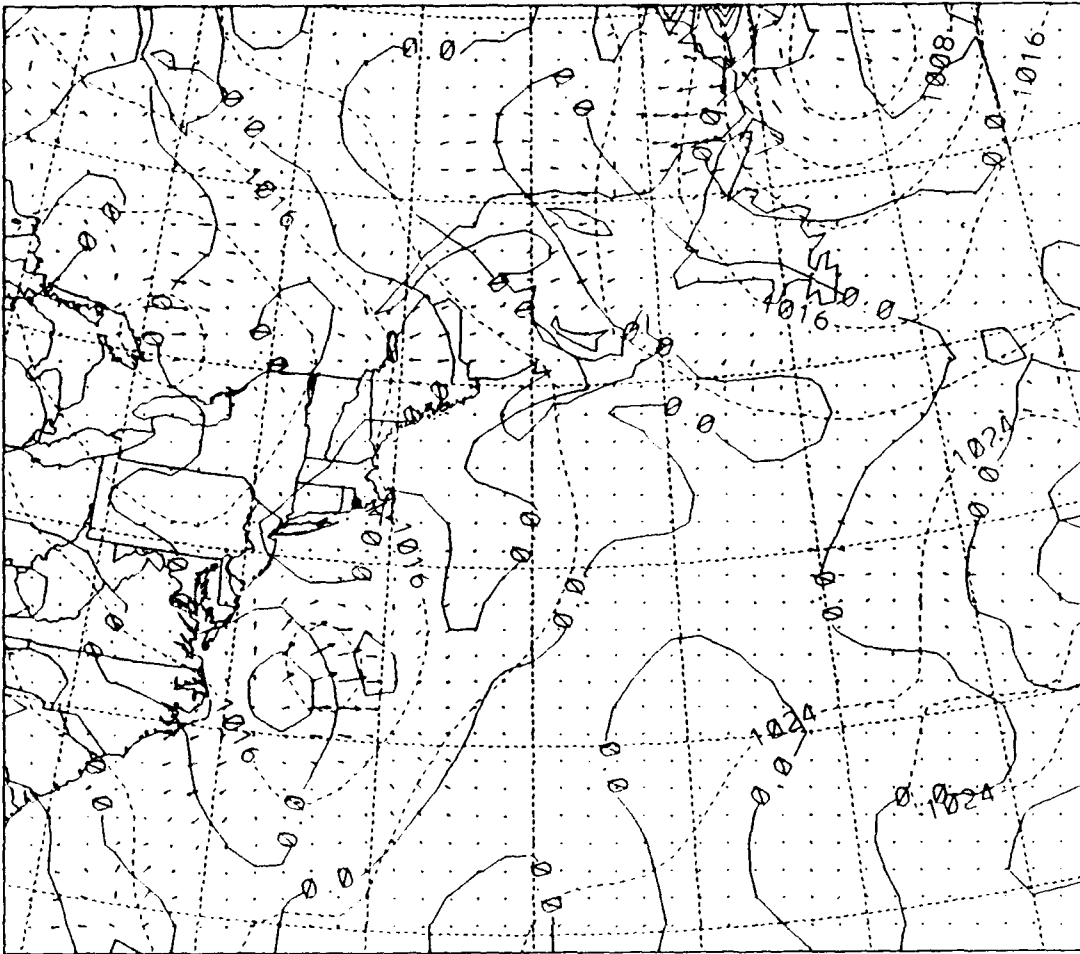


Fig. 53. $-2\nabla \cdot \mathbf{Q}$, surface isobars and \mathbf{Q} vectors as in Fig. 21, except for 0300 UTC 19 January 1989.

divergence also matches well with the relatively cloud-free area immediately to the west of the developing low.

As the surface low rapidly develops between 1200 UTC and 1800 UTC 19 January, the surface \mathbf{Q} vector field has maximum convergence values approaching $20 \times 10^{-16} \text{ m kg}^{-1} \text{ s}^{-1}$ east-northeast of the 1200 UTC 19 January position of the low (Fig. 55). The 1201 UTC 19 January satellite IR image (Fig. 56) indicates mid- and upper-level stratiform clouds in this vicinity. Convergence values increase to over

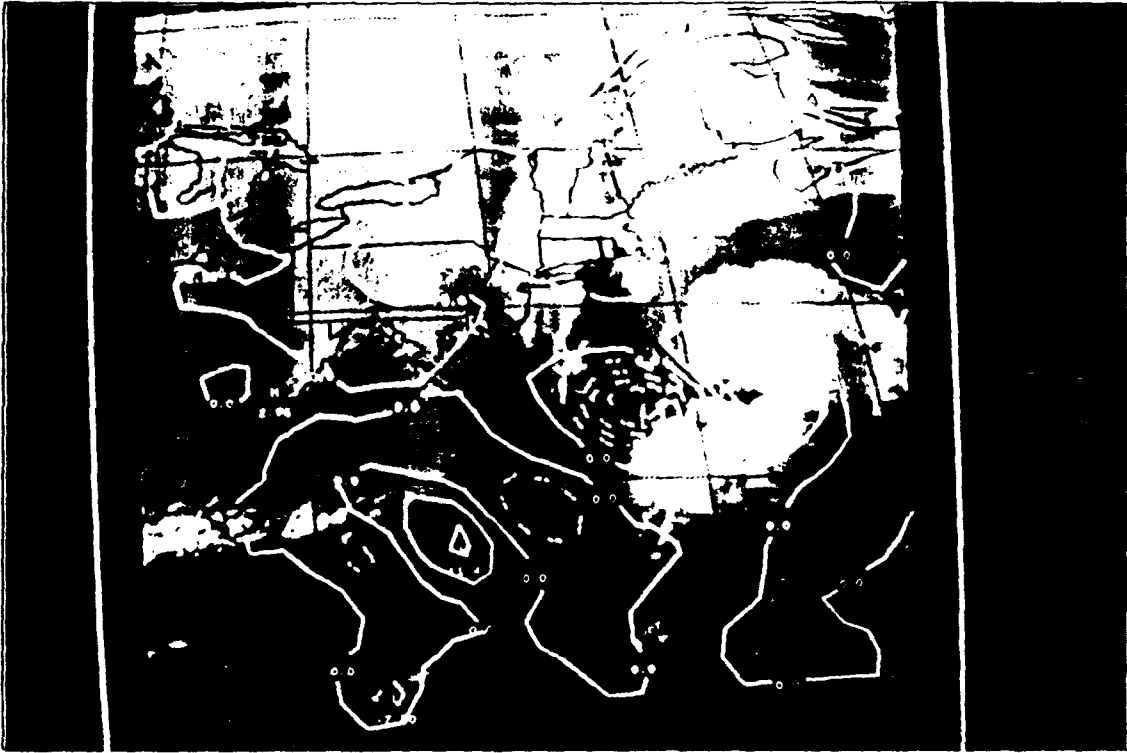


Fig. 54. GOES IR imagery and $-2\nabla \cdot \mathbf{Q}$ as in Fig. 22, except for 0601 UTC 19 January 1989.

$30 \times 10^{-16} \text{ m kg}^{-1} \text{ s}^{-1}$ by 1500 UTC 19 January, with the largest values east-northeast of the low center. These values, in addition to providing a clue about the imminent intensification of IOP 5, also give qualitative information about the storm track. The maximum \mathbf{Q} vector convergence values are a consistent indicator of where the storm center will be located about 3 h in the future.

From 2100 UTC 19 January to the end of the development phase of the IOP 5 cyclone at 1200 UTC 20 January, the \mathbf{Q} vector convergence patterns (e.g., Fig. 57) follow the same basic pattern as described above, and confirm the diagnostic capability of surface \mathbf{Q} vectors. The magnitude of the \mathbf{Q} vector convergence increases to over

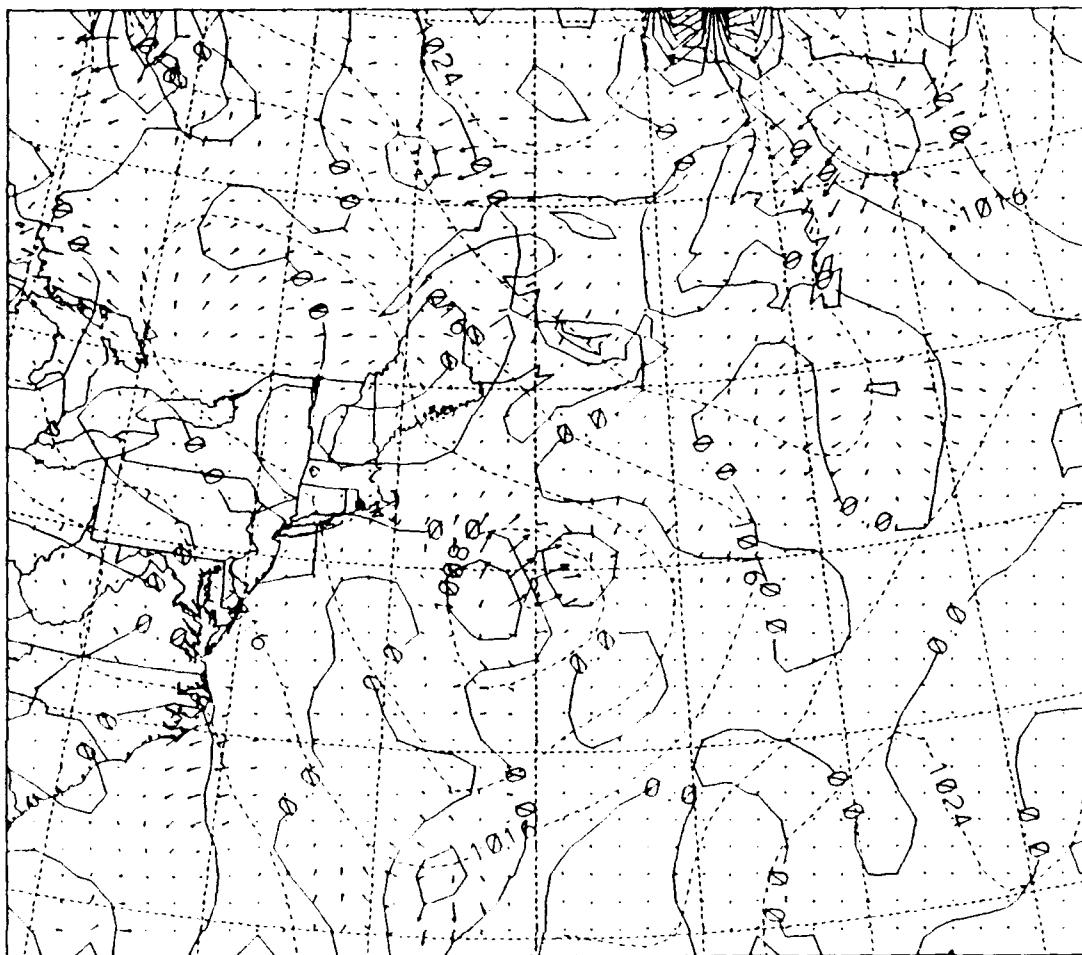


Fig. 55. $-2\nabla\cdot\mathbf{Q}$, surface isobars and \mathbf{Q} vectors as in Fig. 21, except for 1200 UTC 19 January 1989.

$40 \times 10^{-16} \text{ m kg}^{-1} \text{ s}^{-1}$, and the area of maximum convergence closely matches the position of the surface low 3 h in the future.

3. Objective Verification of \mathbf{Q} Vector Divergence

As in the IOP 3 cyclone, \mathbf{Q} vectors and their associated divergence were objectively compared to aircraft measurements of vertical velocity and to 3 h and 6 h future pressure tendencies. The correlations obtained by both methods were similar to those obtained for the IOP 3 case.

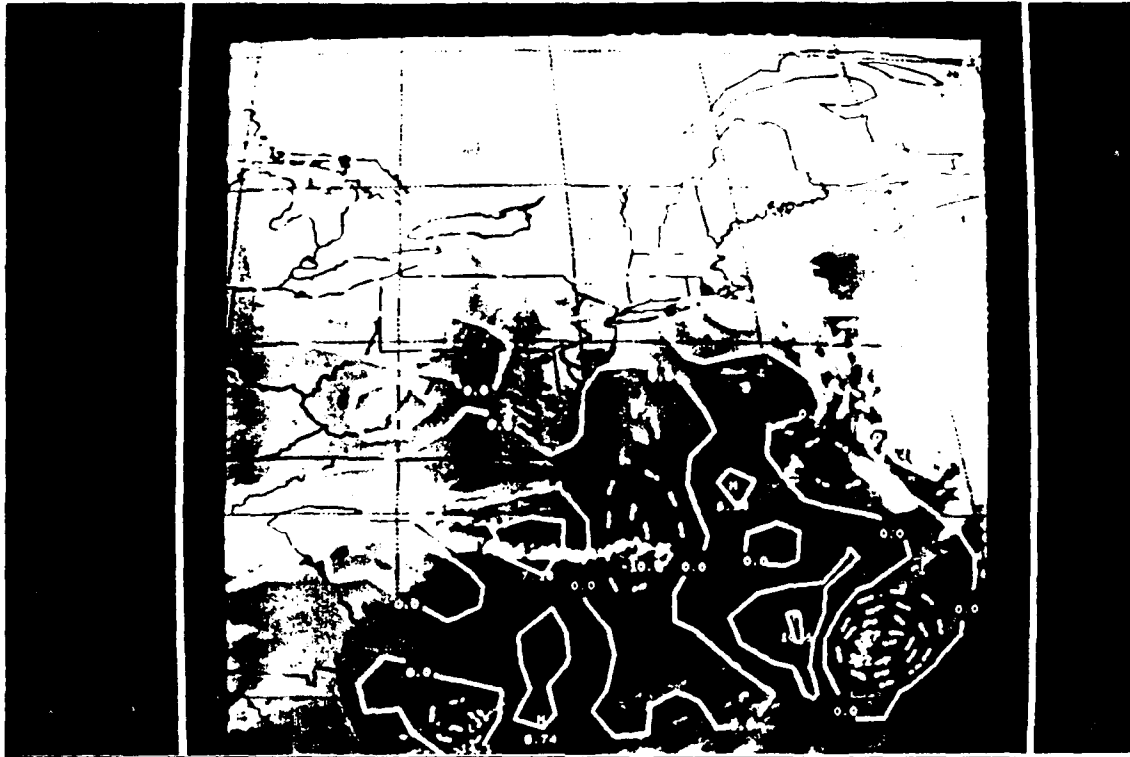


Fig. 56. GOES IR imagery and $-2\nabla\cdot Q$ as in Fig. 22, except for 1201 UTC 19 January 1989.

Five research flights (four WP-3D missions and one "Electra" mission) were conducted during IOP 5, and $-2\nabla\cdot Q$ was compared to the vertical velocity measurements for each flight. These correlations are shown in Table 9. One time period had a strong positive correlation between the vertical velocity and $-2\nabla\cdot Q$, four time periods showed little correlation, and two time periods had a moderately negative correlation between $-2\nabla\cdot Q$ and the measured vertical velocity. Fig. 58 is typical of the flights that had a low correlation value. As in the IOP 3 cyclone, the difference between the time the aircraft measured the vertical velocity and the synoptic time is probably responsible for most of

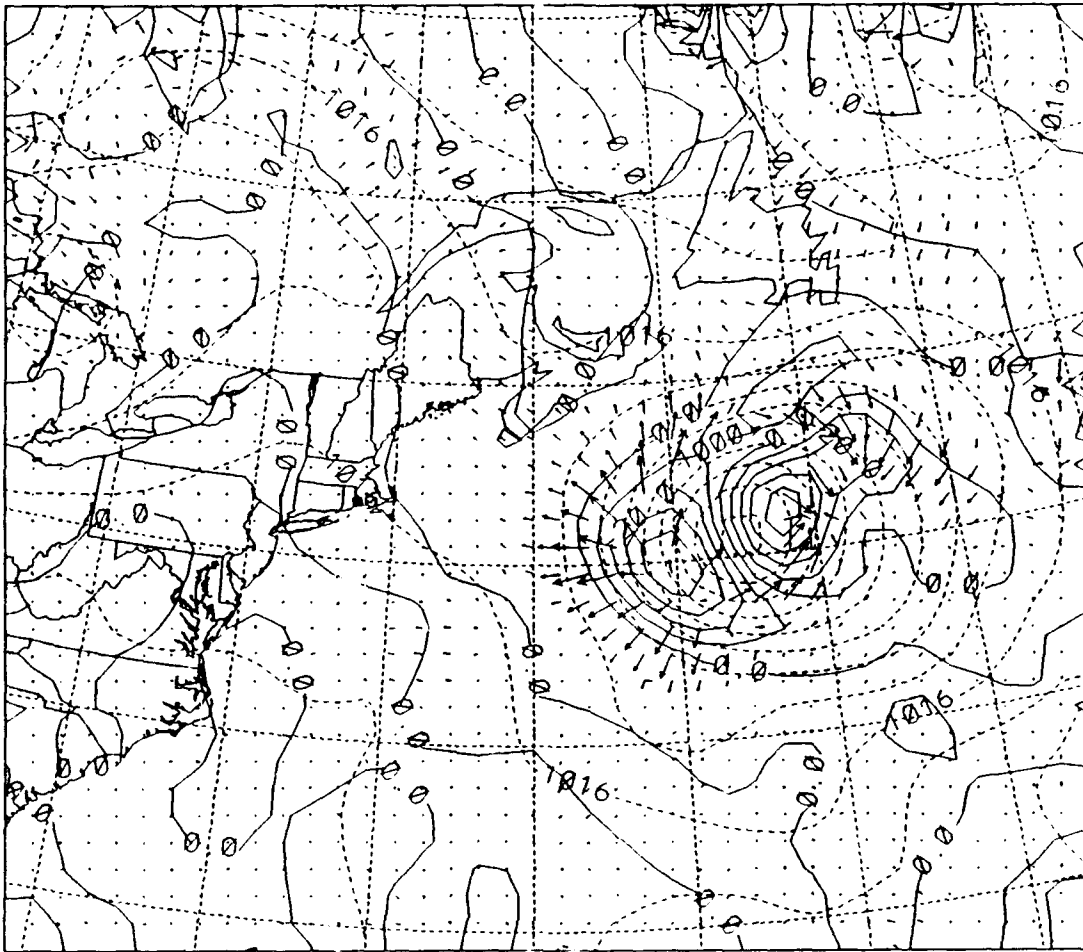


Fig. 57. $-2\nabla \cdot \mathbf{Q}$, surface isobars and \mathbf{Q} vectors as in Fig. 21, except for 0000 UTC 20 January 1989.

the phase differences observed, and no conclusive results can be made from this method of verification.

In the comparison of the \mathbf{Q} vectors with the future 3-h pressure changes, significant differences between areas of convergence and divergence are evident as they were in IOP 3. Fig. 59 has convergent \mathbf{Q} vectors at 0000 UTC 20 January close to the center of the region of 10-12 mb pressure falls, and the divergent \mathbf{Q} vectors are near the area where the pressure rose 6-8 mb in the following 3 h. A comparison of the 0000

Table 9. CORRELATION BETWEEN VERTICAL VELOCITY (w , cm s^{-1}) MEASURED BY AIRCRAFT AND $-2\nabla\cdot\mathbf{Q}$ ($\text{m kg}^{-1} \text{ s}^{-1}$) DURING IOP 5.

Center time of aircraft flight (DDHHMM UTC January 1989)	Number of observations	Correlation between w and $-2\nabla\cdot\mathbf{Q}$ for all observations	Number of observations < 1500 m	Correlation between w and $-2\nabla\cdot\mathbf{Q}$ for observations < 1500 m
190900	203	0.68	174	0.03
191500	299	-0.16	206	0.15
191800	274	0.06	192	0.15
192100	303	-0.58	212	0.10
200000	314	-0.17	0	---
200300	302	-0.52	55	-0.68
200600	302	0.20	39	0.42

UTC 20 January \mathbf{Q} vectors and the 6-h isallobars (Fig. 60) has the convergent \mathbf{Q} vectors about 400 km west-southwest of the greatest pressure falls. This phase lag can be attributed to the fast movement of the IOP 5 cyclone ($\sim 65 \text{ km h}^{-1}$ after 0000 UTC 20 January). If the region of maximum \mathbf{Q} vector convergence is about 200 km east-northeast of the cyclone (as in Fig. 57), then the center of the storm will pass near that point in about 3 h, and the pressure will rise during the following 3 h.

Scatter plots of $-2\nabla\cdot\mathbf{Q}$ vs. future pressure change for 3 h (Fig. 61) and 6 h (Fig. 62) were constructed. The correlations and linear regression between $-2\nabla\cdot\mathbf{Q}$ and the future pressure changes are listed in Table 10. As with the aircraft observations, correlation coefficients are again similar to those obtained in the IOP 3 cyclone. Correlation coefficients ranged from -0.4 to -0.6 when values $\geq |10| \times 10^{-16} \text{ m kg}^{-1} \text{ s}^{-1}$

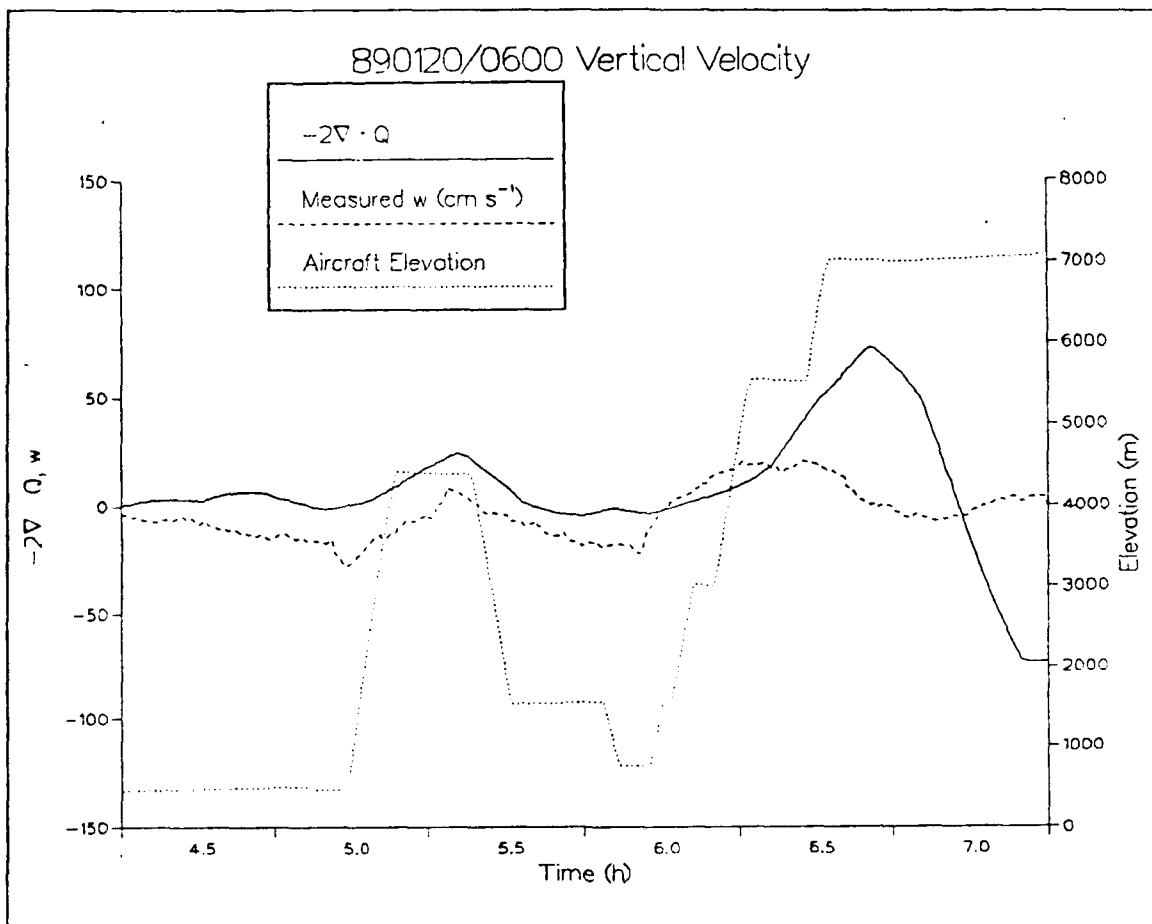


Fig. 58. Vertical velocity, $-2\nabla \cdot \mathbf{Q}$ and aircraft elevation as in Fig. 30 centered 90 minutes either side of 0600 UTC 20 January 1989.

were used. The correlation coefficient increased to -0.72 for $-2\nabla \cdot \mathbf{Q}$ values $\geq |20| \times 10^{-16} \text{ m kg}^{-1} \text{ s}^{-1}$ for pressure changes 3 h in the future. Again, the best correlations between $-2\nabla \cdot \mathbf{Q}$ and future pressure tendencies were between regions of \mathbf{Q} vector divergence and future pressure rises.

Future 3-h and 6-h pressure changes for regions of \mathbf{Q} vector divergence were compared against future pressure changes for regions of \mathbf{Q} vector convergence for each analysis time. Prior to 0300 UTC 19 January, fewer than five grid points per time period

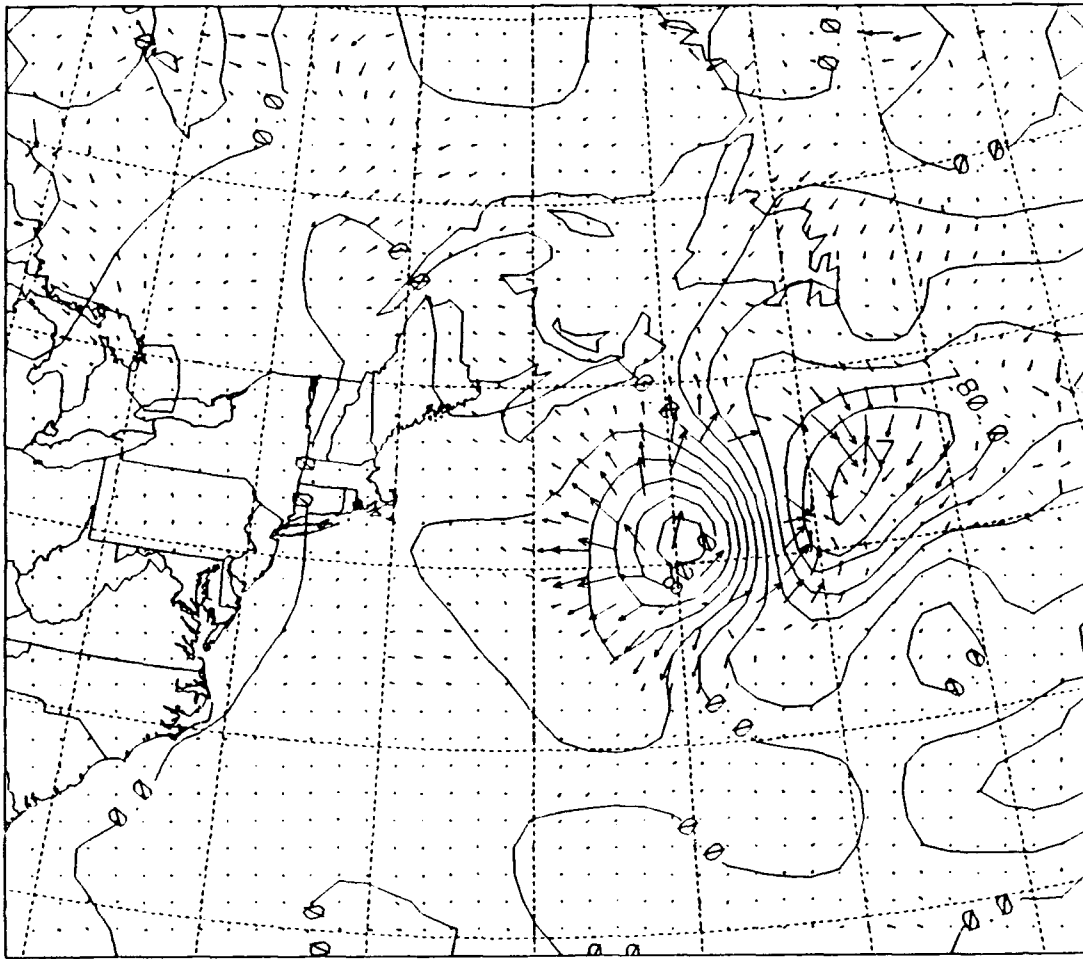


Fig. 59. Q vectors (arrows) at 0000 UTC 20 January 1989 and isallobars (mb*10 per 3 h, solid) for 0300-0000 UTC 20 January 1989.

had a magnitude greater than $10 \times 10^{-16} \text{ m kg}^{-1} \text{ s}^{-1}$. This prevents any statistically meaningful result for these early time periods. For the ten time periods starting at 0300 UTC 19 January, statistically significant different future 3 h pressures occur for areas where $|2\nabla \cdot \mathbf{Q}| \geq 10 \times 10^{-16} \text{ m kg}^{-1} \text{ s}^{-1}$ (Fig. 63). The same conclusion holds for seven of nine time periods in comparisons with pressure changes 6 h into the future (Fig. 64).

Table 11 and Table 12 show that between 0300 UTC 19 January and 0300 UTC 20 January, areas that had $-2\nabla \cdot \mathbf{Q}$ values of at least $10 \times 10^{-16} \text{ m kg}^{-1} \text{ s}^{-1}$ experienced

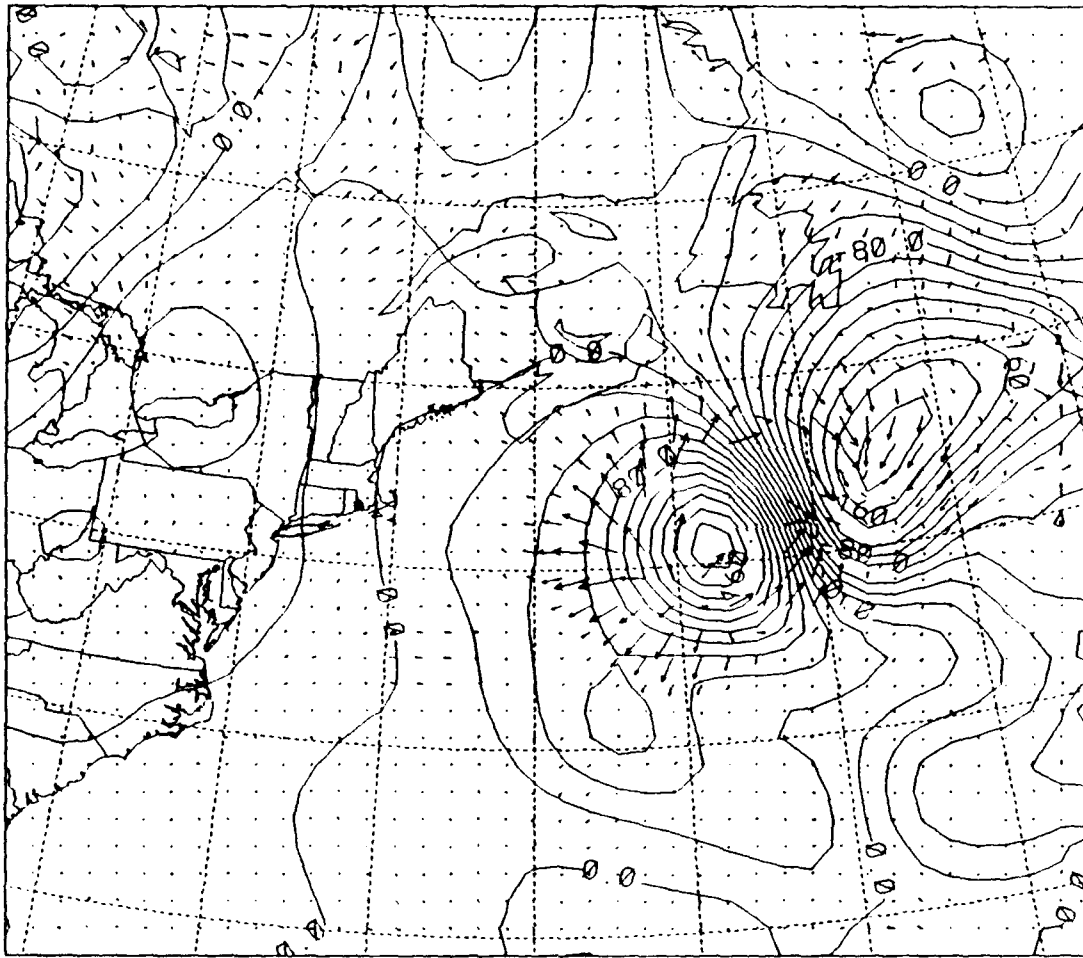


Fig. 60. Q vectors (arrows) at 0000 UTC 20 January 1989 and isallobars (mb*10 per 6 h, solid) for 0600-0000 UTC 20 January 1989.

an average 4.5 and 5.0 mb decrease in pressure over the following 3 h and 6 h, respectively. Areas whose $-2\nabla \cdot \mathbf{Q}$ values were $-10 \times 10^{-16} \text{ m kg}^{-1} \text{ s}^{-1}$ or less had average rises in pressure of 2.3 and 5.0 mb during the next 3 h and 6 h respectively.

Although the IOP lasted until 1200 UTC 20 January, analyses after 0600 UTC 20 January may be less accurate due to the storm approaching the eastern edge of the ERICA study area. Consequently, pressure tendencies involving 0900 UTC and 1200 UTC 20 January were not included in the above calculations.

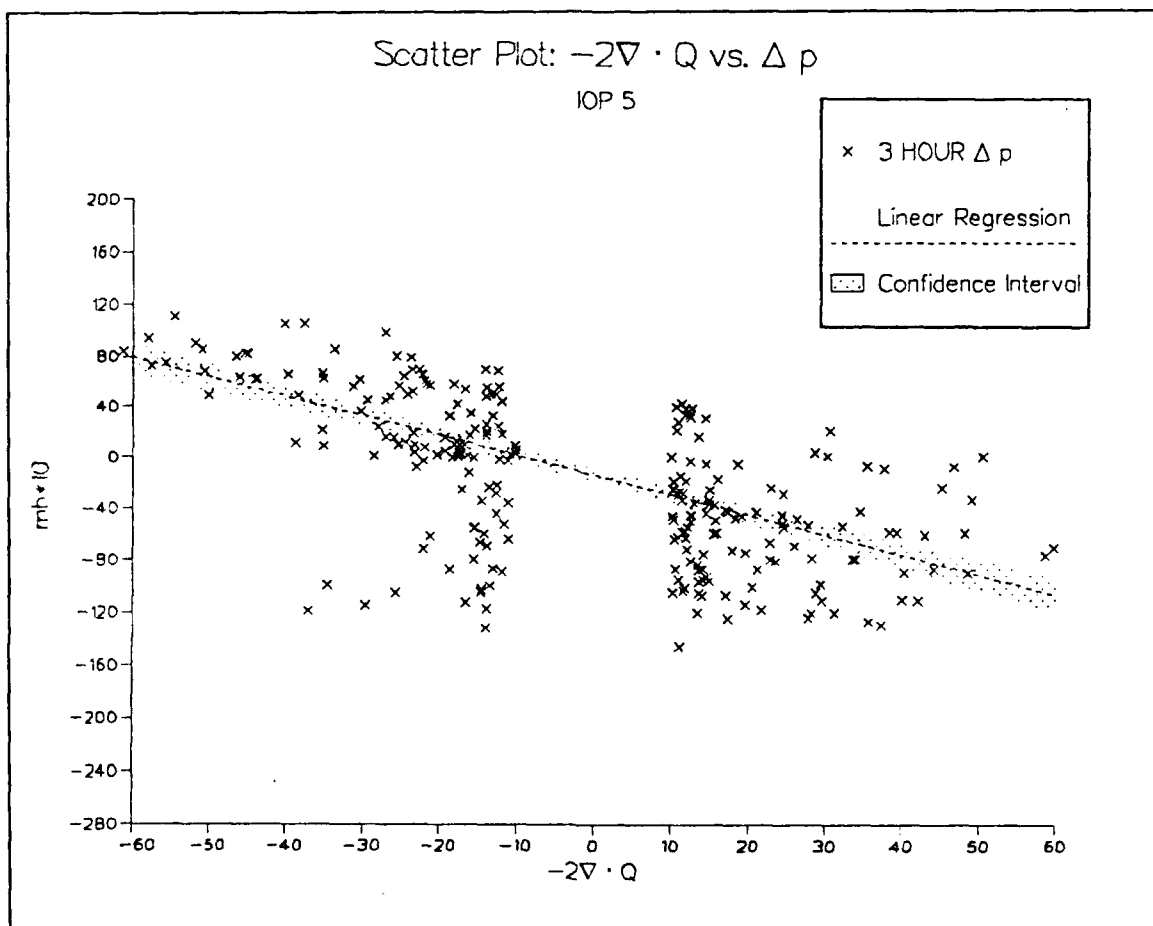


Fig. 61. Scatter plot of $-2\nabla \cdot Q$ ($\times 10^{16} \text{ m kg}^{-1} \text{ s}^{-1}$) vs. the future 3 h pressure tendency ($\text{mb} \times 10$), with linear regression line (dashed) and 95% confidence interval (dotted) for IOP 5.

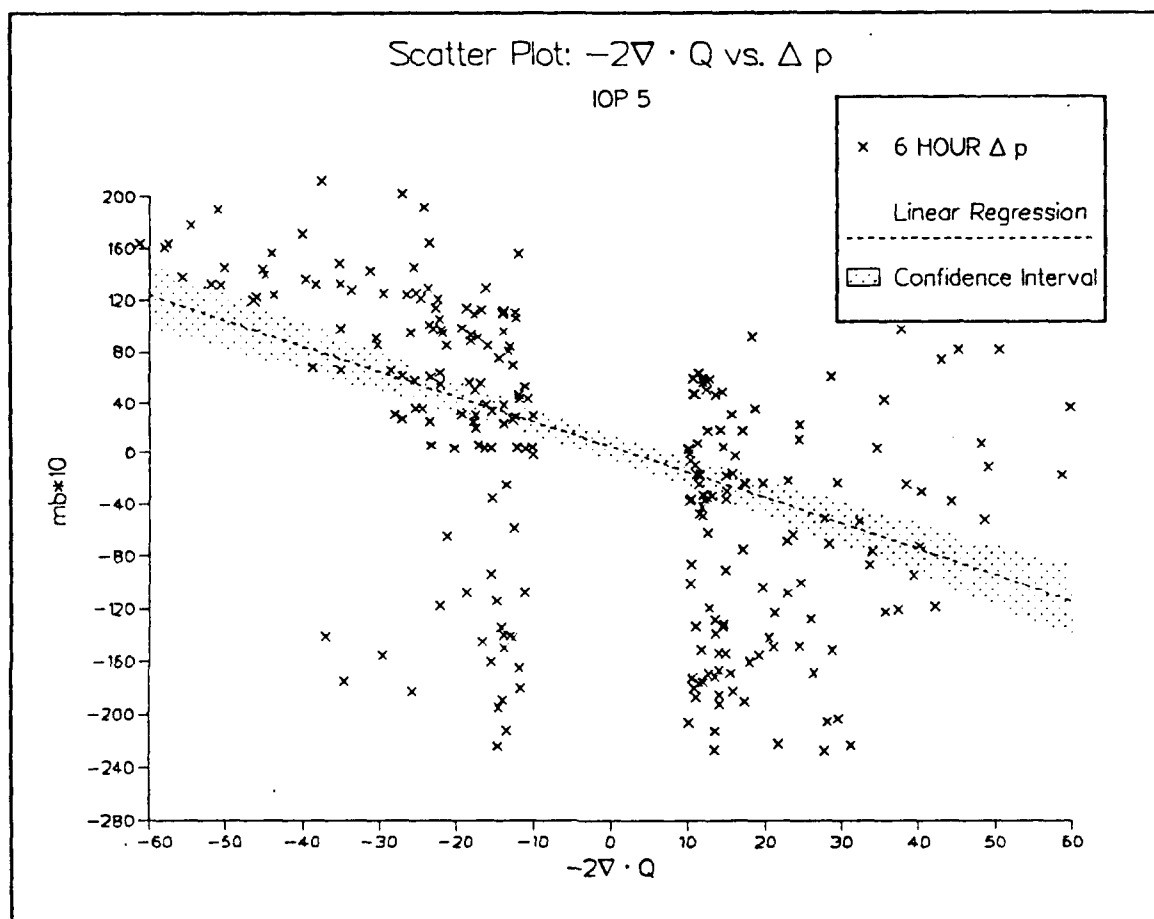


Fig. 62. Scatter plot of $-2\nabla \cdot Q$ ($\times 10^{-16} \text{ m kg}^{-1} \text{ s}^{-1}$) vs. the future 6 h pressure tendency ($\text{mb} \times 10$), with linear regression line (dashed) and 95% confidence interval (dotted) for IOP 5.

Table 10. CORRELATION COEFFICIENTS AND LINEAR REGRESSION EQUATIONS FOR THE IOP 5 CYCLONE.

Δt (h in the future)	Number of Data Points	Standard Deviation of the Regression Line	Regression Equation	Correlation between the Pressure Change and $-2\nabla \cdot Q$
Regression Equation is in the form $y = a + bx$, where y = Pressure change (mb*10) Δt hours in the future $x = -2\nabla \cdot Q \times 10^{-16} \text{ m kg}^{-1} \text{ s}^{-1}$				
3	407	57.6	$y = -13.3 - 1.6x$	-0.60
6	407	113.6	$y = 5.0 - 2.0x$	-0.44

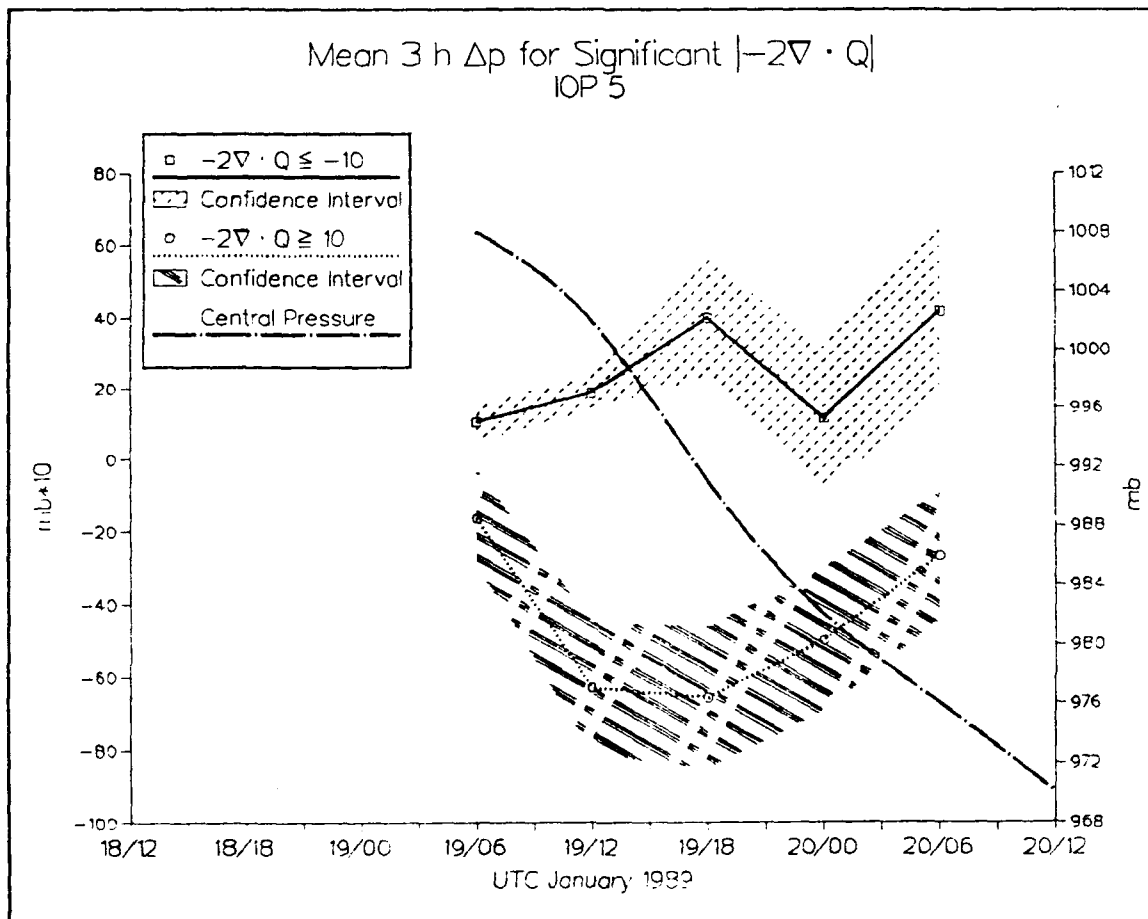


Fig. 63. Mean 3 h pressure tendency for significant (see text) $|-2\nabla \cdot Q|$ (solid and dotted lines), 95% confidence intervals (hatched) and analyzed central pressure of the IOP 5 storm (dash-dot).

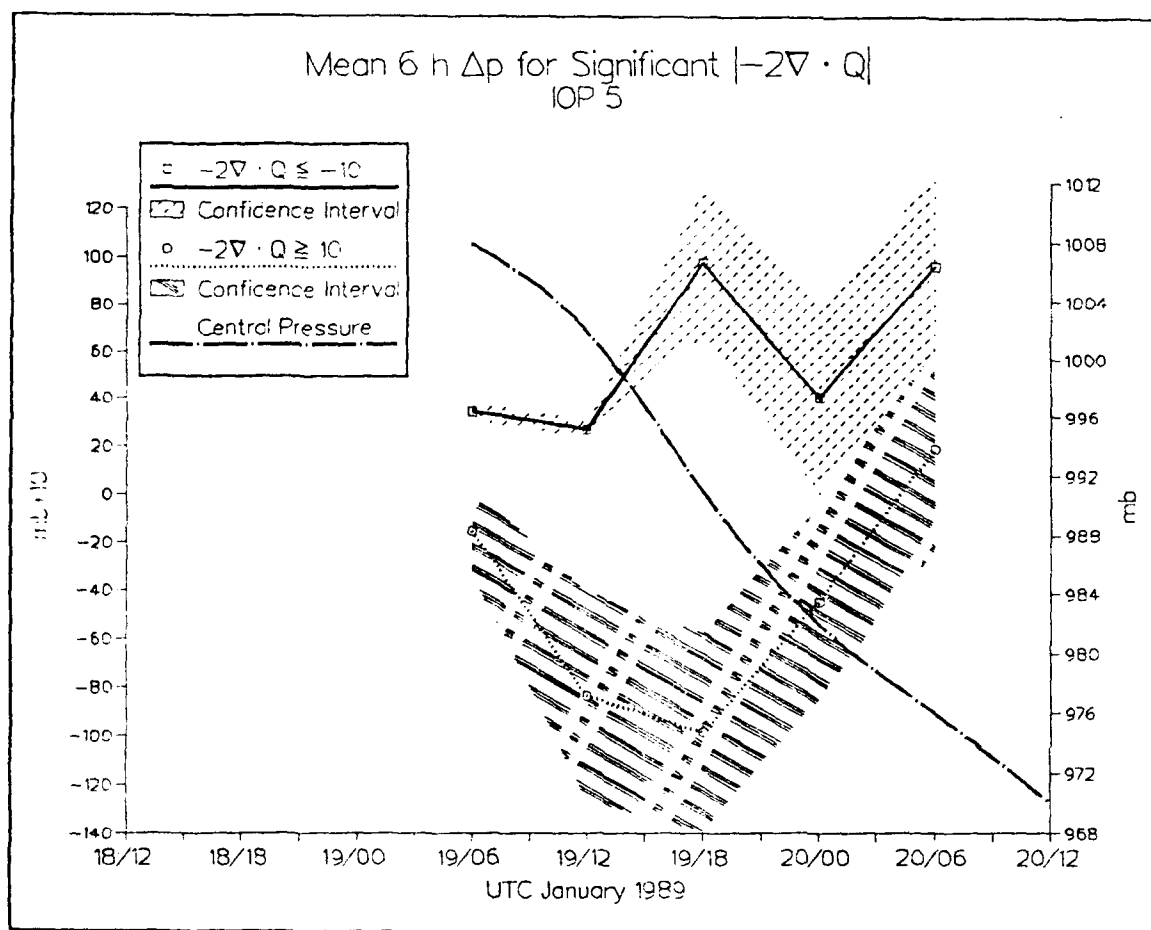


Fig. 64. As in Fig. 63, except for 6 h pressure tendency.

Table 11. $-2\nabla \cdot \mathbf{Q}$ VS. 3 H FUTURE PRESSURE TENDENCY FOR THE IOP 5 CYCLONE.

Time (DDHH UTC January 1989)	Threshold value for $-2\nabla \cdot \mathbf{Q}$ ($\times 10^{-16} \text{ m kg}^{-1} \text{ s}^{-1}$)	Number of grid points	Mean pressure change (mb) in 3 h	Standard Deviation
1906	-10	7	1.0	0.6
	+10	6	-1.6	1.3
1912	-10	8	1.9	0.5
	+10	8	-6.3	2.1
1918	-10	18	4.0	2.8
	+10	23	-6.6	3.8
2000	-10	44	1.2	6.8
	+10	37	-5.0	6.1
2006	-10	41	4.2	7.9
	+10	33	-2.7	5.1

Table 12. $-2\nabla \cdot \mathbf{Q}$ VS. 6 H FUTURE PRESSURE TENDENCY FOR THE IOP 5 CYCLONE.

Time (DDHH UTC January 1989)	Threshold value for $-2\nabla \cdot \mathbf{Q}$ ($\times 10^{-16} \text{ m kg}^{-1} \text{ s}^{-1}$)	Number of grid points	Mean pressure change (mb) in 6 h	Standard Deviation
1906	-10	7	3.4	0.4
	+10	6	-1.5	1.9
1912	-10	8	2.7	0.5
	+10	8	-8.4	4.9
1918	-10	18	9.7	5.3
	+10	23	-9.9	8.0
2000	-10	44	4.0	13.5
	+10	37	-4.5	12.4
2006	-10	41	9.6	11.8
	+10	33	1.9	12.4

C. DISCUSSION

Comparisons between $-2\nabla\cdot\mathbf{Q}$, satellite imagery and the future 3-h and 6-h pressure changes were encouraging for both IOPs 3 and 5. Satellite pictures showed cold-topped stratiform clouds or organized convection directly over or very close to the region of maximum \mathbf{Q} vector convergence during the storms' rapid deepening phase. During IOP 5, an area of sustained convection that was a precursor to the surface low formation was well depicted by the \mathbf{Q} vector convergence. Apparent areas of upward motion as implied by satellite imagery correlated best with the surface \mathbf{Q} vectors when the upper-level forcing (as inferred from the NMC final analyses) and near-surface dynamics were in phase. Correlation with the satellite imagery was smallest when the storms had matured, and the upper-level supporting dynamics had moved ahead of the surface low during IOP 3.

Satisfactory results were also obtained when the \mathbf{Q} vector convergence values were objectively compared to the future 3 and 6 h pressure tendencies. Quasi-geostrophic dynamics, as applied through the use of surface \mathbf{Q} vector convergence fields, successfully indicated areas of positive and negative pressure tendencies 3 h and 6 h in the future. In conjunction with satellite imagery, this tool could be used as a short-term qualitative predictive field for the future direction of the storm.

The \mathbf{Q} vector convergence fields agree closely with the conceptual model of an extratropical cyclone (i.e., rising air to the north and east of the storm, and sinking air to the south and west of the storm), but the \mathbf{Q} vectors do not distinguish between the two

processes that change the surface pressure: intensification and translation of the storm. One reason for the modest correlation coefficients obtained may be the neglect of pressure advection terms. Using (2),

$$-2\nabla \cdot \mathbf{Q} = \left(\sigma \nabla^2 + f_o^2 \frac{\partial^2}{\partial p^2} \right) \omega \sim -\omega \equiv -\frac{dp}{dt} \quad (4)$$

and

$$\frac{dp}{dt} = \frac{\partial p}{\partial t} + \bar{v} \cdot \nabla p + w \frac{\partial p}{\partial z} . \quad (5)$$

Correlations between $-2\nabla \cdot \mathbf{Q}$ and future pressure tendencies only account for the first term on the right side of (5). Scale analysis for a developing extratropical cyclone shows that the horizontal and vertical advective terms are the same order of magnitude as the local time rate of change of surface pressure.

Determining the magnitude of future deepening using the surface \mathbf{Q} vectors may not be appropriate. The mean \mathbf{Q} vector divergence around the storm was calculated for each analysis time for both the IOP 3 and IOP 5 cyclones. For every (a total of 15) analysis time, the mean \mathbf{Q} vector divergence was not statistically significantly different from zero. This includes periods in which the low was deepening at a rate in excess of 1 mb h⁻¹. This result may be attributed to a characteristic of the quasi-geostrophic equations. Pauley and Nieman (1991) found that a significant deviation between quasi-geostrophic vertical motion and the vertical motion from a hydrostatic, generalized omega equation was the tendency for the quasi-geostrophic equations to over-estimate the sinking motion

to the rear of the storm. Ageostrophic advection terms are significant in this region of the storm, where these terms act in a direction opposite to the quasi-geostrophic vertical motion.

The amount of "warning" that Q vectors may provide about an imminently deepening storm appears to depend upon the present strength of the low-level disturbance. In the IOP 3 cyclone, a well-defined surface low pressure system was also in existence. As this disturbance began to intensify, the magnitude of the Q vector convergence significantly increased 6 h prior to the commencement of the rapid development. By contrast, the IOP 5 cyclone had a much weaker surface low system at the start of the rapid development stage. The lack of a well-defined surface low at the start resulted in only a 3 h warning between the onset of substantially stronger Q vector convergence values and the commencement of the rapid deepening of the IOP 5 cyclone.

Q vector divergence fields derived from surface data consistently produced a distinct "couplet" pattern of divergence behind the storm and convergence ahead of the storm, which implies rising vertical motion north and east of the cyclone center and sinking vertical motion south and west of the center of the storm. This pattern of vertical motion is expected in the vicinity of a cyclone, as has been well-known for many years (e.g., Petterssen 1956). In both the IOP 3 and 5 cyclones, the magnitude of this couplet increased by a factor of three as the storms intensified. The couplet pattern is strikingly similar to the full physics quasi-geostrophic ω field (Fig. 65) from Kuo *et al.* (1991) and the location of the rising air relative to the storm agrees with the Pauley and Nieman (1991) generalized omega equation. Both the shape of the couplet pattern and the

locations of rising and sinking motion with respect to the surface storm agree very well with the patterns of Q vector convergence in this study. Adiabatic quasi-geostrophic ω fields are typically much broader, and have less magnitude and structure in the vertical velocity (Fig. 66), as

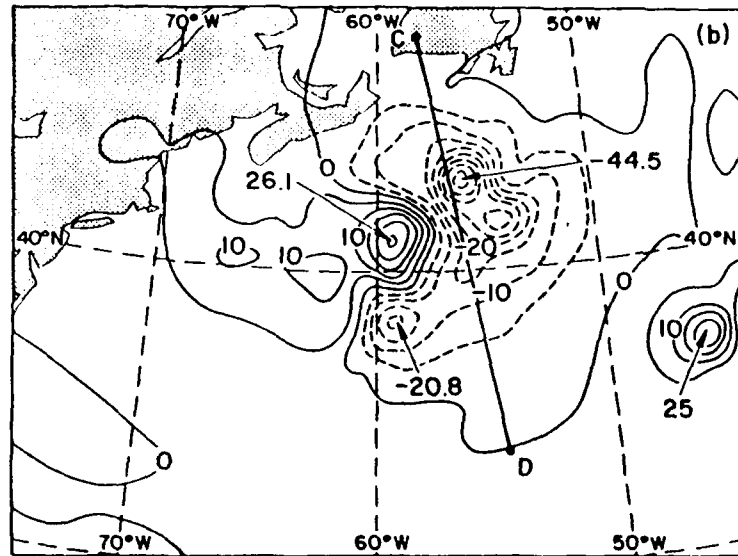


Fig. 65 Quasi-geostrophic vertical motion (ω , mb s^{-1}) at 700 mb, based upon a full-physics model run of Kuo *et al.* (1991, Fig. 15 b).

shown by Kuo *et al.* (1991). This may occur since Q vectors are an alternate way to represent the forcing terms for the Sawyer-Eliassen equations (if friction and diabatic terms are neglected). Therefore, the structure noted in the Q vector divergence field is representing strong surface frontogenetical terms. Another explanation may be that as the atmosphere increasingly departs from

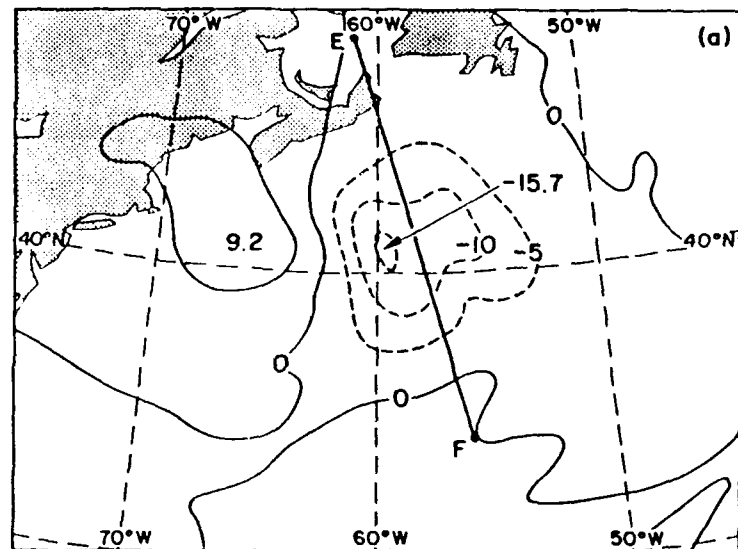


Fig. 66. Quasi-geostrophic vertical motion (ω , mb s^{-1}) at 700 mb calculated for an adiabatic experiment (Kuo *et al.* 1991, Fig. 15 a).

geostrophic and thermal wind balance, Q vectors will depict the intensified ageostrophic circulation that is necessary to restore the atmospheric balances. Thus, as Hoskins and Pedder (1980) noted, Q vectors would implicitly account for diabatic effects and the Q vector divergence field would produce a vertical velocity profile more similar to that of a full physics simulation. Further studies are required to quantify the amount of diabatic forcing accounted for by Q vectors.

Although the Q vectors were successful in diagnosing vertical motions in these case studies, these results probably do not apply to all oceanic storms. Surface-based Q vectors may not represent mid-tropospheric vertical motion in regions of high static stability that inhibit effective coupling between the lower- and mid-troposphere. Similarly, surface-based Q vectors may not be an appropriate diagnostic tool in areas where the surface temperature gradient does not represent the deeper troposphere gradient. An example of such a region is near the west coast of a continent, over regions of oceanic upwelling.

Q vectors--at any level--have limitations when applied to forecasting situations. The 0600 UTC 19 January 1989 satellite IR picture (Fig. 54) illustrates the strengths and limitations of surface-based Q vectors particularly well. As discussed above, Q vectors accurately indicate the location of the extensive stratiform clouds in the comma head and imply upward vertical motion where the convection was breaking out along the newly-formed cold front. However, Q vectors give no indication of the gale force winds that developed east of the North Carolina and Virginia coast (Fig. 67). Satellite imagery and ship observations indicate that these gale-force winds are occurring under clear skies, and

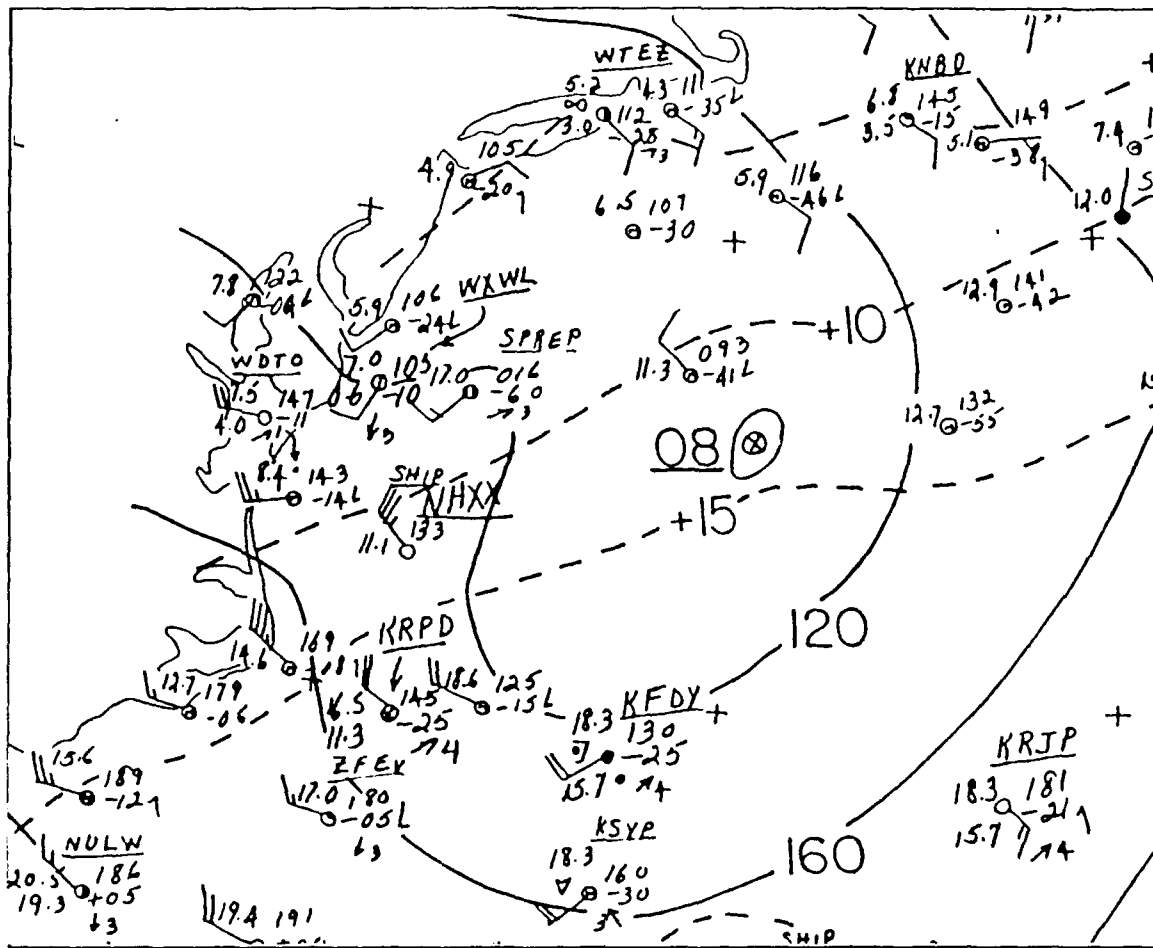


Fig. 67. 0600 UTC 19 January 1989 surface analysis by Sanders (1989) of temperature ($^{\circ}\text{C}$, dashed) and pressure (mb, solid). Observations plotted using conventional notation.

the Q vectors do not indicate any organized lifting immediately east of the coast. These gale-force winds appear to be mesoscale in nature, and are most likely caused by a downward transfer of momentum as cool air flows from the continent and is destabilized from below by large surface heat fluxes over the ocean. Surface-based Q vectors are not likely to indicate these areas of supergeostrophic winds.

Surface-based Q vectors may be also be less successful in diagnosing vertical motion for storms near the coast. Surface Q vectors calculated over hilly or mountainous

terrain, snow-covered regions, or other areas with temperature gradients that are not representative of the deeper atmosphere will probably have less correlation with either current areas of precipitation-producing clouds or with future pressure tendencies.

Even if favorable conditions exist, such as low static stability and surface temperatures that are representative of the mean tropospheric temperature field, surface Q vector calculations can be no better than the analyses of surface pressure and temperature upon which the Q vectors are based. As mentioned previously, accurate analysis of pressure and temperature over the ocean based on limited ship observations is a challenging task. Another important consideration is the process to convert the analysis to a regular grid for calculations. As Dunn (1991) notes, an incorrect method of interpolating an analysis onto a grid, or a poor choice in finite difference methods, can create sufficient noise in a field to mask the signal. This issue cannot be neglected if Q vectors are to be calculated in an operational setting.

Once the temperature and pressure analysis has been gridded, the Q vectors are simple to calculate. For an 80 km grid that covers one half of the North Atlantic Ocean, the time to calculate Q vectors and $\nabla \cdot Q$ is no longer than a few seconds on a current generation personal computer.

V. CONCLUSIONS AND RECOMMENDATIONS

A. CONCLUSIONS

Surface Q vector analysis based upon temperature and pressure data were useful in diagnosing low-level, synoptic-scale vertical motions in the two storms studied. Despite the numerous approximations required to apply quasi-geostrophic theory to surface data, sufficient signal was found in the rapidly developing cyclones studied to produce meaningful Q vector divergence fields. Although these Q vectors were calculated using the enhanced ERICA dataset, the additional observations for a synoptic time may not be crucial. Although drifting buoys accounted for only 13% of the observations for the IOP 5 cyclone, Q vectors calculated at synoptic times had similar values with respect to the cyclone as did the Q vectors evaluated for the IOP 3 storm.

Q vectors and $-2\nabla \cdot Q$ provide qualitative guidance for the near-term (0-6 h) track of the storm, but do not demonstrate skill at forecasting the future intensity of the cyclone. This inability to provide a forecast of storm intensity may be due to the limitations of the quasi-geostrophic theory upon which the Q vectors are based. The Q vectors and their associated divergence fields correlate qualitatively to significant cloud fields as depicted by satellite imagery, and quantitatively to future 3 h and 6 h pressure tendencies. An analysis of surface-based Q vectors is not designed to replace upper-air analyses. Given favorable synoptic conditions, such a method may provide a proxy to the mean tropospheric vertical velocity when no upper-air data are available.

Surface pressures fell an average of 3-4 mb and 4-5 mb in the next 3 h and 6 h, respectively, in areas where there was significant ($\geq 10 \times 10^{-16} \text{ m kg}^{-1} \text{ s}^{-1}$) Q vector convergence. Surface pressure rises averaged 1-3 mb and 3-5 mb for 3 h and 6 h respectively, in areas of significant Q vector divergence. The correlation between the future pressure tendency and $-2\nabla \cdot Q$ was highest for areas where $-2\nabla \cdot Q \leq -20 \times 10^{-16} \text{ m kg}^{-1} \text{ s}^{-1}$. While these values were calculated based on only two cases, they provide some practical guidance to apply Q vector divergence to future pressure tendencies.

B. RECOMMENDATIONS

Of course, two case studies are not sufficient to conclusively prove or disprove any method. Additional case studies should be done, and should include storms that did not deepen as rapidly as IOPs 3 and 5. ERICA storms that would be appropriate to investigate further include IOP 6 and IOP 7. Oceanic cyclogenesis during the summer could be studied to see how stable the atmosphere can become before surface-based Q vectors lose their diagnostic and predictive value.

An appropriate sensitivity study would be to calculate the Q vectors for one storm based upon independent surface analyses. These analyses would be based upon varying amounts of surface and satellite data, with data gaps imposed in some analyses near frontal boundaries. These tests would determine how sensitive the Q vectors are to changes in the surface analysis. Results of this study could help determine if surface Q vectors are practical and appropriate in an operational environment.

This method could also be applied to "model" storms, where the forcing can be compared to known vertical velocities. Calculating Q vectors for the *Queen Elizabeth 2* storm that Kuo *et al.* (1991) and Pauley and Nieman (1991) have analyzed may show how close the $-2\nabla\cdot Q$ values are to either the total ω or the full physics, quasi-geostrophic ω values. The contribution to $-2\nabla\cdot Q$ (if any) of the implicit diabatic forcing should be calculated. A related study could derive and apply Q vectors to semi-geostrophic theory. The resulting fields ("S" vectors?) should account for ageostrophic advections and provide more realistic vertical motions, especially in the subsiding air to the rear of the storm.

Assuming that the above studies will confirm the use of surface-based Q vectors in an operational setting, a cost-benefit analysis should be done to determine the feasibility of seeding the winter-time oceans with relatively low cost ERICA-type drifting buoys, and placing this data in the Global Telecommunications System (GTS). If this were done, oceanic surface analyses of temperature and pressure could be derived at least every 3 h. This increase in temporal resolution of data over the oceans may help to improve short-term forecasts that are vital to civilian and military maritime interests.

Further research is also required to quickly and accurately convert an operational surface (or upper-air) analysis with sparse data onto a regular grid. Gridding an analysis through multiple trial-and-error bogussing iterations is not acceptable in an operational environment. Operational meteorologists require the ability to interactively modify an objective analysis with a pointing device such as a light pen or a mouse. When the meteorologist is satisfied with the analysis, the computer would grid the revised analysis and then perform the Q vector calculations.

LIST OF REFERENCES

- Barnes, S. L., 1964: A technique for maximizing details in numerical weather map analysis. *J. Appl. Meteor.*, **3**, 396-409.
- _____, 1973: Mesoscale objective analysis using weighted time-series observations. NOAA Tech. Memo. ERL NSSL-62, National Severe Storms Laboratory, Norman, 60 pp. [NTIS COM-73-10781.]
- Bjerknes, J., and H. Solberg, 1922: Life cycle of cyclones and the polar front theory of atmospheric circulation. *Geofys Publ.*, **3**, No. 1, 30-45.
- Bluestein, H. B., and K. Thomas, 1984: Diagnosis of a jet streak in the vicinity of a severe weather outbreak in the Texas Panhandle. *Mon. Wea. Rev.*, **112**, 2499-2519.
- Bosart, L. F., 1981: The Presidents' Day snowstorm of 18-19 February 1979: A subsynoptic-scale event. *Mon. Wea. Rev.*, **109**, 1542-1566.
- Chang, C. B., D. J. Perkey and C. W. Kreitzberg, 1982: A numerical case study of the effects of latent heating on a developing wave cyclone. *J. Atmos. Sci.*, **39**, 1555-1570.
- Charney, J. G., 1947: The dynamics of long waves in a baroclinic westerly current. *J. Meteor.*, **4**, 135-162.
- Danard, M. B., and G. E. Ellenton, 1980: Physical influences on East Coast cyclogenesis. *Atmos.-Ocean*, **18**, 65-82.
- Doswell, C. A., III, 1986: Short-range forecasting. *Mesoscale Meteorology and Forecasting*. P. S. Ray, ed. Amer. Meteor. Soc., 689-719.
- Dunn, L. B., 1991: Evaluation of vertical motion: Past, present and future. *Wea. Forecasting*, **6**, 65-75.
- Durrán, D. R., and L. W. Snellman, 1987: The diagnosis of synoptic-scale vertical motion in an operational environment. *Wea. Forecasting*, **2**, 17-31.
- Eady, E. T., 1949: Long waves and cyclonic waves. *Tellus*, **1**, 33-52.

- Eliassen, A., 1962: On the vertical circulation in frontal zones. *Geophys. Publ.*, **24**, 147-160.
- Emanuel, K. A., 1983: On assessing local conditional symmetric instability from atmospheric soundings. *Mon. Wea. Rev.*, **111**, 2016-2033.
- _____, 1985: Frontal circulations in the presence of small moist symmetric instability. *J. Atmos. Sci.*, **42**, 1002-1071.
- Farrell, B., 1984: Modal and non-modal baroclinic waves. *J. Atmos. Sci.*, **41**, 668-673.
- Gall, R., 1976: The effects of released latent heat in growing baroclinic waves. *J. Atmos. Sci.*, **33**, 1686-1701.
- Gerald, C. F., and P. O. Wheatley, 1990: *Applied Numerical Analysis*. Fourth Edition. Addison-Wesley Publishing Company, 679 pp.
- Gyakum, J. R., 1983: On the evolution of the QE II storm. I: Synoptic Aspects. *Mon. Wea. Rev.*, **111**, 1137-1155.
- Hadlock, R., and C. W. Kreitzberg, 1988: The Experiment on Rapidly Intensifying Cyclones over the Atlantic (ERICA) field study: Objectives and plans. *Bull. Amer. Meteor. Soc.*, **69**, 1309-1320.
- _____, R., E. Hartnett and G. Forbes, 1989: Experiment on Rapidly Intensifying Cyclones over the Atlantic (ERICA) Field Phase Summary. [Available from ERICA Data Center, Department of Physics and Atmospheric Science, Drexel University, Philadelphia, Pennsylvania 19104.], 388 pp.
- Haltiner, G. J., and R. T. Williams, 1980: *Numerical Prediction and Dynamic Meteorology*, Second Edition. John Wiley and Sons, 477 pp.
- Holton, J. R., 1979: *An Introduction to Dynamic Meteorology*. Second Edition. Academic Press, 391 pp.
- Hoskins, B. J., and M. S. Pedder, 1980: The diagnosis of middle latitude synoptic development. *Quart. J. Roy. Meteor. Soc.*, **106**, 707-719.
- _____, I. Draghici and H. C. Davies, 1978: A new look at the ω equation. *Quart. J. Roy. Meteor. Soc.*, **106**, 707-719.

- Johnson, D. R., and W. K. Downey, 1976: The absolute angular momentum budget of an extratropical cyclone: Quasi-Lagrangian diagnostics 3. *Mon. Wea. Rev.*, **104**, 3-14.
- Keyser, D., and T. N. Carlson, 1984: Transverse ageostrophic circulations associated with elevated mixed layers. *Mon. Wea. Rev.*, **112**, 2465-2478.
- Kocin, P. J., and L. W. Uccellini, 1990: *Snowstorms Along the Northeastern Coast of the United States: 1955 to 1985*. Meteorological Monographs. American Meteorological Society, 280 pp.
- Kuo, Y.-H., and R. J. Reed, 1988: Numerical simulation of an explosively deepening cyclone in the Eastern Pacific. *Mon. Wea. Rev.*, **116**, 2081-2105.
- _____, and S. Low-Nam, 1990: Prediction of nine explosive cyclones over the Western Atlantic ocean with a regional model. *Mon. Wea. Rev.*, **118**, 3-25.
- _____, M. A. Shapiro and E. G. Donall, 1991: The interaction between baroclinic and diabatic processes in a numerical simulation of a rapidly intensifying extratropical marine cyclone. *Mon. Wea. Rev.*, **119**, 368-384.
- Mailhot, J., and C. Chouinard, 1989: Numerical forecasts of explosive winter storms: sensitivity experiments with a meso-a scale model. *Mon. Wea. Rev.*, **117**, 1311-1343.
- Mullen, S. L., and D. P. Baumhefner, 1988: Sensitivity of numerical simulations of explosive oceanic cyclogenesis to changes in physical parameterizations. *Mon. Wea. Rev.*, **116**, 2289-2329.
- NOAA, 1979: Smooth log, North Atlantic weather, September and October 1978. *Mar. Wea. Log*, **23**, p. 104.
- Nuss, W. A., and S. I. Kamikawa, 1990: Dynamics and boundary layer processes in two Asian cyclones. *Mon. Wea. Rev.*, **118**, 755-771.
- Ohring, G., 1990: Applications of satellite data in meteorology. *Weather Satellites: Systems, Data, and Environmental Applications*. P. K. Rao, S. H. Holmes, R. K. Anderson, J. S. Winston and P. E. Lehr, eds. Amer. Meteor. Soc., 251-259.
- Pauley, P. M., and S. J. Nieman, 1991: A comparison of quasi-geostrophic and non-quasi-geostrophic vertical motions for a model-simulated rapidly intensifying marine extratropical cyclone. *Mon. Wea. Rev.*, **119** (submitted)

- Petersen, R. A., and J. D. Stackpole, 1989: Overview of the NMC production suite. *Wea. Forecasting*, **4**, 313-322.
- Petterssen, S., 1956: *Weather Analysis and Forecasting*. Volume One. McGraw-Hill, 428 pp.
- _____, Bradbury, D. L. and K. Pedersen, 1962: The Norwegian cyclone models in relation to heat and cold sources. *Geophys. Publ.*, **24**, 243-280.
- Pyke, C. B., 1965: On the role of air-sea interaction in the development of cyclones. *Bull. Amer. Meteor. Soc.*, **46**, 4-15.
- Reed, R. J., and M. D. Albright, 1986: A case study of explosive cyclogenesis in the eastern Pacific. *Mon. Wea. Rev.*, **114**, 2297-2319.
- Roebber, P. J., 1984: Statistical analysis and updated climatology of explosive cyclones. *Mon. Wea. Rev.*, **111**, 723-744.
- Sanders, F., 1989: Surface temperature and pressure analyses for the Experiment on Rapidly Intensifying Cyclones over the Atlantic (ERICA) Intensive Observation Periods (IOPs). [Available from ERICA Data Center, Department of Physics and Atmospheric Science, Drexel University, Philadelphia, Pennsylvania 19104].
- _____, 1990: Surface analysis over the oceans--searching for sea truth. *Wea. Forecasting*, **5**, 596-612.
- _____, and J. R. Gyakum, 1980: Synoptic-Dynamic climatology of the "bomb." *Mon. Wea. Rev.*, **108**, 1589-1606.
- _____, and B. J. Hoskins, 1990: An easy method for estimation of Q-vectors from weather maps. *Wea. Forecasting*, **5**, 346-353.
- Sinclair, M. R., and R. L. Elsberry, 1986: A diagnostic study of baroclinic disturbances in polar air streams. *Mon. Wea. Rev.*, **114**, 1957-1983.
- Sutcliffe, R. C., 1947: A contribution to the problem of development. *Quart. J. Roy. Meteor. Soc.*, **65**, 370-383.
- Trenberth, K. E., 1978: On the interpretation of the diagnostic quasi-geostrophic omega equation. *Mon. Wea. Rev.*, **106**, 131-137.

- Uccellini, L. W., 1984: Comments on "Comparative Diagnostic Case Study of East Coast Secondary Cyclogenesis under Weak Versus Strong Synoptic-Scale Forcing." *Mon. Wea. Rev.*, **112**, 2540-2541.
- _____, 1990: Processes contributing to the rapid development of extratropical cyclones. *Extratropical Cyclones The Erik Palmén Memorial Volume*, C. Newton, and E. O. Holopainen, Eds., Amer. Meteor. Soc., 81-105.
- _____, P. J. Kocin, R. A. Petersen, C. H. Wash and K. F. Brill, 1984: The Presidents' Day cyclone of 18-19 February 1979: Synoptic overview and analysis of the subtropical jet streak influencing the pre-cyclogenetic period. *Mon. Wea. Rev.*, **112**, 31-55.
- _____, R. A. Petersen, K. F. Brill, P. J. Kocin and J. J. Tuccillo, 1987: Synergistic interactions between an upper-level jet streak and diabatic processes that influence the development of a low-level jet and a secondary coastal cyclone. *Mon. Wea. Rev.*, **115**, 2227-2261.
- Wash, C. H., J. E. Peak, W. F. Calland and W. A. Cook, 1988: Diagnostic study of explosive cyclogenesis during FGGE. *Mon. Wea. Rev.*, **116**, 2337-2365.
- Williams, R. T., 1972: Quasi-geostrophic versus non-geostrophic frontogenesis. *J. Atmos. Sci.*, **29**, 3-10.
- Winston, J. S., 1955: Physical aspects of rapid cyclogenesis in the Gulf of Alaska. *Tellus*, **7**, 481-500.
- Zwack, P., and M. Kabil, 1988: Estimating lower tropospheric vertical motion from surface pressure and pressure tendency alone. *Mon. Wea. Rev.*, **116**, 795-803.

INITIAL DISTRIBUTION LIST

		No. Copies
1.	Defense Technical Information Center Cameron Station Alexandria, VA 22314	2
2.	Library, Code 52 Naval Postgraduate School Monterey, CA 93943-5000	2
3.	Chairman (Code OC/Co) Department of Oceanography Naval Postgraduate School Monterey, CA 93943-5000	1
4.	Chairman (Code MR/Hy) Department of Meteorology Naval Postgraduate School Monterey, CA 93943-5000	1
5.	Professor Wendell A. Nuss (Code MR/Nu) Department of Meteorology Naval Postgraduate School Monterey, CA 93943-5000	3
6.	Professor Russell J. Elsberry (Code MR/Es) Department of Meteorology Naval Postgraduate School Monterey, CA 93943-5000	1
7.	Professor Carlyle H. Wash (Code MR/Wx) Department of Meteorology Naval Postgraduate School Monterey, CA 93943-5000	1
8.	LCDR David W. Titley (Code MR/TI) Department of Meteorology Naval Postgraduate School Monterey, CA 93943-5000	1

- | | | |
|-----|--|---|
| 9. | Director | 1 |
| | Naval Oceanographic and Atmospheric
Research Laboratory
Monterey, CA 93943-5006 | |
| 10. | Chief of Naval Research | 1 |
| | 800 N. Quincy Street
Arlington, VA 22217 | |
| 11. | Dr. Hugh E. Willoughby | 1 |
| | Hurricane Research Division
NOAA Atlantic Oceanographic and
Meteorological Laboratory
4301 Rickenbacker Causeway
Miami, FL 33149 | |